(1)

INVESTIGATION OF A MAGNETOSTRICTIVE FIBER OPTIC INTERFEROMETRIC SENSOR

THESIS

R. Dempsey Hackett, BSEE
Captain, USAF

AFIT/GEO/ENG/89D-4

DEPARTMENT OF THE AIR FORCE
AIR UNIVERSITY
AIR FORCE INSTITUTE OF TECHNOLOGY

Wright-Patterson Air Force Base, Ohio

(1)

AFIT/GEO/ENG/89D-4

INVESTIGATION OF A MAGNETOSTRICTIVE FIBER OPTIC INTERFEROMETRIC SENSOR

THESIS

R. Dempsey Hackett, BSEE
Captain, USAF

AFIT/GEO/ENG/89D-4

Approved for public release; distribution unlimited

AFIT/GEO/ENG/89D-4

INVESTIGATION OF A MAGNETOSTRICTIVE FIBER OPTIC INTERFEROMETRIC SENSOR

THESIS

Presented to the Faculty of the School of Engineering
of the Air Force Institute of Technology
Air University
In Partial Fulfillment of the
Requirements for the Degree of
Master of Science in Electrical Engineeering

R. Dempsey Hackett, BSEE
Captain, USAF

December 1989

Acknowledgements

I would like to thank the many individuals and organizations that made this research project possible. I cannot over state my appreciation for my faculty advisor, Major Ed Kolesar. I am very thankful that he decided to provide his excellent guidance and support for an additional student. I also appreciate the support I received from the other members of my thesis committee, Dr. Ted Luke and Major Harry Barksdale. I must acknowledge Dale Stevens of the Electronic Technology Laboratory who provided both equipment and useful discussions of fiber optic sensors. I wish to acknowledge the many others who provided support in the electrical engineering and physics departments including: Leroy Cannon, Bob Durham, Bob Lindsey, Charlie Powers, Don Smith, Greg Smith, and Bill Trop.

I am grateful of the support and funds that were provided by the Armstrong Aerospace Medical Research Laboratory.

Finally, I must express my appreciation of my wife, Lydia, who not only encouraged my research, but also helped in the laboratory.

Table of Contents

List of Figures

Figure Page

32

List of Tables

AFIT/GEO/ENG/89D-4

Abstract

This document reports the results associated with a magnetostrictive fiber optic interferometric sensor which was fabricated and evaluated. To evaluate the sensor's performance, a Helmholtz coil was designed and constructed to generate a uniform magnetic field. The sensor's response was determined by examining the amplitude of the interferometer's output light. No DC magnetic fields could be detected due to excessive noise contributed by the fused coupler component in the interferometer. AC measurements were successfully accomplished for a 25 Hz magnetic field by inspecting the modulation of the interferometer's output light at 25 Hz. Sensors composed of RF sputtered metal coated fibers did not detect the AC magnetic field because the thin metal films did not generate enough force to change the length of the optical fiber a detectable amount. The sensor did detect the AC magnetic field when the sensor arm was composed of a bulk nickel rod. Thermal annealing the nickel rod in the presence of an external magnetic field improved the sensor's response. Thinning the optical fiber in the sensor arm did not significantly affect the sensor's performance, but increasing the length of the optical fiber did enhance the sensor's response. The sensor's performance also improved when the AC magnetic field was superimposed on a DC bias magnetic field. In the sensor's optimum configuration, an AC magnetic field flux density of 10 mG was detected.

Investigation of a Magnetostrictive Fiber-Optic Interferometric Sensor

I. Introduction

Background

Magnetic fields generated by human mental activity can provide useful physiological information, such as an indication of pilot workload or loss of consciousness (1:1). However, the flux densities of these weak biomagnetic fields only span one decade (10^{-9} to 10^{-8} Gauss) (1:8). (Appendix A provides an explanation of magnetic flux density and magnetic field units). The intensity of these fields are extremely small compared to the ambient magnetic field which has a flux density of approximately 10^{-1} Gauss (2:360). The current state-of-the-art method of detecting small magnetic fields involves using a superconducting quantum interference device (SQUID) (1:8). This instrument, however, is expensive, bulky, and must be cryogenically-cooled. An overview of the other available magnetic field sensing approaches and their limitations is thoroughly discussed in Chapter II (Literature Review). An alternative technology, known as a magnetostrictive fiber optic interferometric sensor, has been proposed. Theoretically, this technology should be sufficiently sensitive to detect the weak biomagnetic fields without the disadvantages associated with the competing existing technologies (3:87).

The magnetostrictive fiber optic sensor concept is based upon the classic Mach-Zehnder interferometer (3:87). To implement this technology, one fiber is coated with a magnetostrictive material, and it serves as the sensor arm. A second fiber is uncoated, and it is used as the reference arm. In practice, a magnetic field will deform the magnetostrictive coating covering the fiber in the sensor arm, and this induced deformation will cause perturbations in the light propagating in that arm. These perturbations can subsequently be detected via the constructive/destructive interference pattern that is generated when the sensor arm's light is recombined with the light propagating in the reference arm. The use of the interference property is responsible for the high sensitivity of the sensor since changes in the length of the sensor arm (on the order of the wavelength of the propagating light) can be detected. The basic arrangement is illustrated in Figure I.1. More detailed illustrations of the exact interferometers built are included in Chapter IV (Experimental Procedure).

The initial theoretical study postulated that the sensor would be sufficiently sensitive to detect a magnetic flux density as small as 10^{-12} Gauss, which would certainly enable the detection of biomagnetic fields (3:87). However, the prototype sensors fabricated thus far have not achieved the theoretically predicted minimum nor the level associated with human biomagnetic activity (4:47). A minimum detectable magnetic flux density of 1.4×10^{-4} G at 25 Hz has been achieved by the American Research

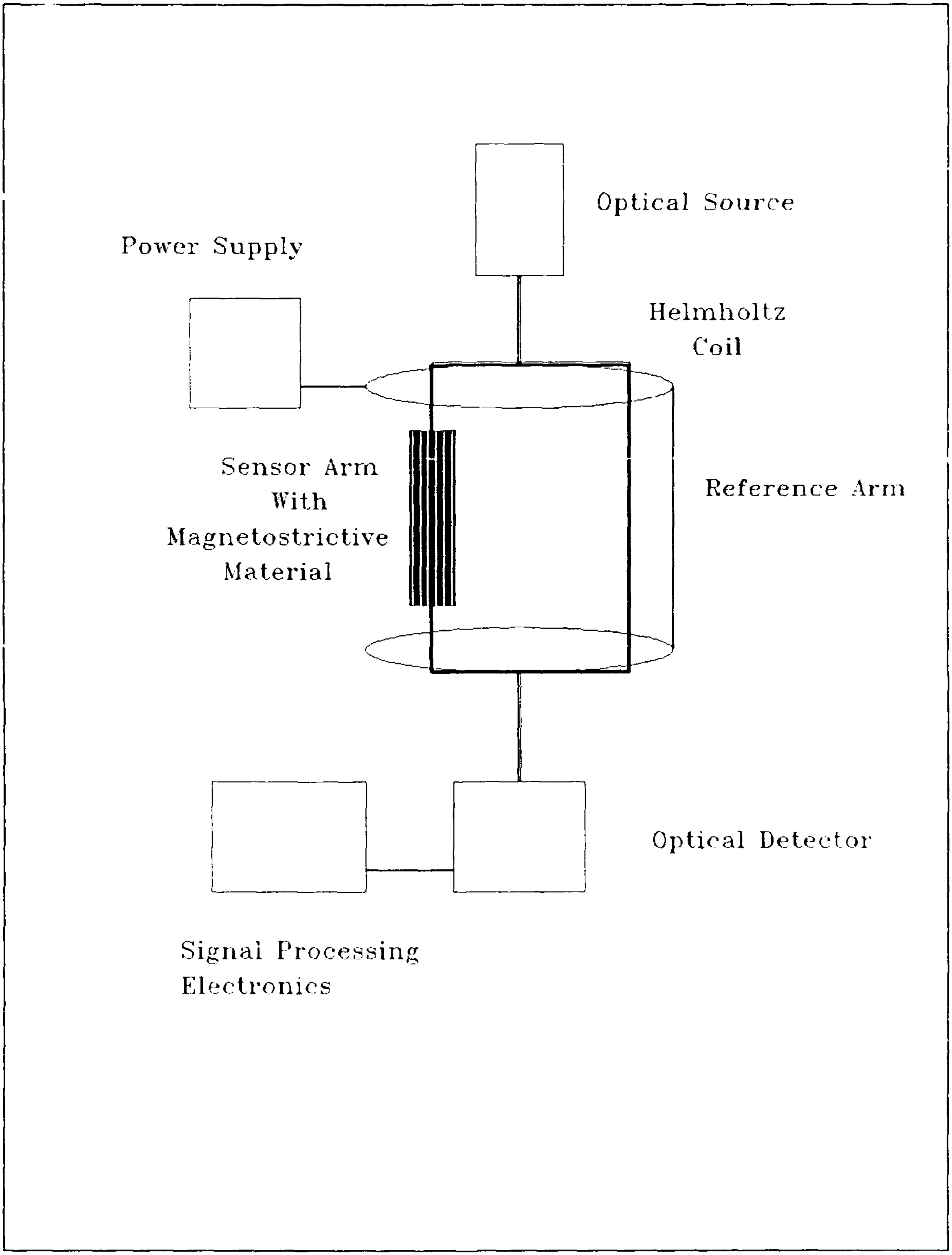

Figure I.1. Interferometer Arrangement

Corporation of Virginia, and this value represents the progress made thus far (5:36). Chapter II (Literature Review) provides a more comprehensive discussion concerning the previous developments of the magnetostrictive fiber optic sensor.

Problem Statement

This thesis project attempted to realize the desired minimum detectable biomagnetic field flux density of 10^{-9} Gauss by designing and fabricating an interferometer with optimized sensor arms. The frequency range of interest spans DC to 30 Hz.

The sensor arm in most of the previously fabricated interferometers were of two types (4:48). The first class of sensor arms used a standard fiber optic cable epoxied to a slab of bulk magnetostrictive material. This type of sensor arm is difficult to accurately characterize and reproduce due to the epoxy that serves as an interface between the magnetostrictive material and optical fiber. The second type of sensor arms were conventional fiber optic cables that were coated with a magnetostrictive material. Many methods have been used to coat the fiber, including electron beam evaporation (6:408), electroplating (7:86), and RF sputtering (8:32). However, no one has thoroughly characterized the sensor's performance with respect to utilizing RF sputtered materials and specific coating geometries. It was the goal of this research project to characterize RF sputtered sensor arms. For completeness, several magnetostrictive coating materials and bulk magnetostrictive materials were investigated along with the influence of thermally annealing the thin films while they are exposed to an externally applied magnetic field.

Scope

The method of depositing the magnetostrictive materials was limited to the highly-reliable, monolithic silicon integrated circuit thin film RF sputtering technology. The magnetostrictive materials used included: cobalt, iron, and nickel. These materials all exhibit magnetostrictive properties, and they have been utilized in similar applications (1:14). The wavelength of light used to excite the sensor was restricted to 633 nm to reduce the number of parameters investigated. The influence of wavelength on the sensor's performance is thoroughly addressed in the theoretical analysis section.

Assumptions

The ultimate goal of this project was to design, fabricate and evaluate the performance of a magnetostrictive fiber optic sensor possessing sufficient sensitivity to detect biomagnetic fields. However, to test the sensor, the biomagnetic fields were simulated. A Helmholtz coil was designed, fabricated, and calibrated for this purpose. During calibration, the Helmholtz coil's dynamic magnetic field intensity and uniformity were determined. The magnetic field intensity measured was limited by the fabrication tolerances associated with the Helmholtz coil, the regulation of the applied current, and the ambient magnetic flux density, and not by the sensitivity of the Hall effect magnetometer which was used for calibration (9:5).

Approach

This project encompassed three critical tasks: sensor arm design and fabrication, interferometer instrumentation design and configuration, and the sensor's performance evaluation. This section only outlines the approach. The details associated with accomplishing the various tasks are discussed in Chapter IV (Experimental Procedure).

Sensor Arm Design and Fabrication

The first step in designing and fabricating the sensor arm was to prepare and examine the ends of the fiber optic cable. The length of the sensor arm was limited to 10 cm, which was the extent of the uniform magnetic field generated. Once the ends of the fiber optic cable were adequate to make optical connections, the fiber's outer glass cladding was cleaned and thinned using chemical etchants. The magnetostrictive materials were then RF sputtered. Coating variables included: thickness, geometry, and thermal annealing conditions, which included annealing in the presence of an external magnetic field. Additional sensor arms were fabricated by bonding a fiber to a bulk magnetostrictive material sample.

Interferometer Configuration

This task required connecting the fibers (coated and uncoated) and components to from an interferometer. All of the fiber ends were carefully prepared to make high-quality optical connections. Once the fiber ends were prepared, the fiber-to-fiber connections were made using glass ferrule tubes. All of the fibers, couplers, and connections were evaluated for optical power loss before the interferometer was assembled, as well as during the sensor's fabrication sequence.

Sensor Performance Evaluation

Prior to evaluating the sensor, the Helmholtz coil was designed, fabricated, and calibrated. The sensor, with each of the various sensor arm configurations, was evaluated for its response to DC and AC magnetic fields. These performance measurements were accomplished by varying the applied magnetic field's magnitude and examining the interferometer's output light amplitude and frequency information.

Plan of Development

Following this Chapter, which serves as an overview of the thesis research, a literature review is presented. Chapter II identifies the competing magnetic field sensing technologies and highlights the evolution and the current status of research concerning magnetostrictive fiber optic sensor technology. The applicable theory is presented in Chapter III, which includes a discussion of Helmholtz coil design, Mach-Zehnder interferometer operation, fiber optic cables, electromagnetic propagation in cylindrical waveguides, magnetostrictive materials, and the sensor arm designs. Chapter IV describes the experimental procedures used to fabricate and evaluate the interferometric sensor and the Helmholtz coil. The results of the experiments are reported in Chapter V. The last Chapter concludes with a summary and recommendations for subsequent research.

II. Literature Review

Introduction

Since the initial concept for detecting magnetic fields with a fiber optic interferometer was reported in 1980, dozens of papers concerning this sensor technology have been published. Research regarding this sensor concept is being conducted in government, industry, and university laboratories in Denmark, Great Britain, Japan, and the United States (10:57). After identifying the other available methods of detecting magnetic fields and their limitations, this section highlights the important advances in the development of the magnetostrictive fiber optic sensor and reports on the sensor's current performance status.

Competing Technologies

Many methods are currently available to detect magnetic fields. However, as this section will illustrate, none of the technologies competing with the magnetostrictive fiber optic sensor have the same potential for high sensitivity, compactness, and low cost. The other technologies addressed include: induction coils, Hall effect magnetometers, magneto-optic devices, superconductor quantum interference devices (SQUIDs), and magnetoresistive devices.

A fluxmeter is an example of an induction coil that has a typical sensitivity of 10^{-5} G. A fluxmeter detects magnetic fields through the movement of a coil placed in a magnetic field

(1:10). The coil rotates as it is moved through an area of changing magnetic flux density (1:10).

A Hall effect magnetometer detects magnetic fields through the voltage that appears when a semiconductor with a current passing through it is placed in a magnetic field. The Hall effect is often used in laboratory settings to detect magnetic fields as small as 10^{-5} G (9:3).

While less sensitive than Hall effect magnetometers, magneto-optic devices are used to measure power line current (10:60). Magneto-optic devices operate using the Faraday effect, which states that linearly polarized light is rotated when the light propagates in special media that are exposed to magnetic fields. Quartz, special glass, ferrite and some semiconductors have been used as the Faraday element. The magnetic field sensitivity of the magneto-optic device depends on the Verdet constant and propagation length of the Faraday element. A sensitivity of 10^{-2} G is representative of magneto-optic devices (1:11).

SQUID magnetometers currently are the most sensitive magnetic field detectors available, and they possess a minimum detectable magnetic flux density of 10^{-9} $Gm^{-1}Hz^{-1/2}$. There are two types of SQUID magnetometers: DC-SQUIDs and RF-SQUIDs. DC-SQUIDs consist of a DC bias current flowing through a loop composed of two Josephson junctions. A change in the applied magnetic flux density can be detected from the change in current flowing through the loop. RF-SQUIDs contain only one Josephson junction in a loop that is excited with an RF bias current. While SQUIDs are sufficiently sensitive to detect biomagnetic fields, they require cooling to 4.2° K, which makes the device bulky and expensive to operate because of the liquid helium dewar requirement. Since SQUIDs cost hundreds of thousands of dollars, they are too expensive for many research applications (1:12). In October 1989, IBM and the Helsinki University reported that they had fabricated a sensor capable of detecting magnetic fields generated by the brain that was composed of four SQUIDs on a silicon chip (11:5).

The final technology competitive with the magnetostrictive fiber optic sensor is the magnetoresistive sensor, which detects magnetic fields using the magnetoresistive effect. The change in resistance of a current carrying magnetic material induced by an externally applied magnetic field is referred to as the magnetoresistive effect (12:2). Philips produces a magnetoresistive sensor that uses a Wheatstone bridge arrangement composed of magnetic materials. Philips claims their detector is one and one half times more sensitive than Hall effect magnetometers (12:6).

Initial Proposal

Yariv and Winsor first proposed the magnetostrictive fiber optic sensor concept in March 1980 (3:87-89). In their paper, they described the sensor's configuration, the principle of magnetostriction, and calculated the minimum magnetic field flux density that could be detected using their theoretically modeled sensor. Their sensor was proposed using nickel as the magnetostrictive material. By assuming that the magnetic field to be detected was a small AC field superimposed upon a larger DC field, they stated that the change in the phase of light propagating in the sensor arm would be directly proportional to the length of the sensor arm and the magnitude of the AC field. To determine the minimum detectable magnetic field, they assumed that the dominant noise source would be shot-noise in the light detector. Shot-noise is the result of random electron emissions in the electrical components (13:104). Using an excitation laser source with an output power level of 1 mW, an emission wavelength of 1 micron, a detector possessing a quantum efficiency of 0.5, and a detection bandwidth of 1 Hz, they calculated a minimum detectable magnetic field flux density of 1.6×10^{-9} Gauss for each 1 meter length of the coated sensor arm.

Experimental Verification

One month after Yariv and Winsor published their proposal for the sensor concept, Dandridge and others at the Naval Research Laboratory published the first experimental evidence that such a sensor would work (6:408-409). They examined the response of two classes of sensor arms: fiber optic cables epoxied around a nickel tube, and 1.5 micron thick electron beam evaporated films of nickel that were deposited directly on the surface of the fiber and then annealed at 900°C in hydrogen. Their measurements indicated that the sensor's sensitivity increased with the frequency of the AC magnetic field. They attributed this increase in sensitivity to the interferometric detection system and not to the magnetostrictive material. Fiber optic interferometric systems are less sensitive at lower frequencies due to the 1/f noise in the light detector (14:141). They also found that the sensors using bulk magnetostrictive material were three orders of magnitude more sensitive than sensors using thin film magnetostrictive material. Their bulk magnetostrictive material sensors exhibited a linear response with magnetic field variations, and peak sensitivities of 8×10^{-8} G for each one meter length of the coated fiber at 10 kHz, and 10^{-5} G at 100 Hz.

Elimination of Interferometer Drift

The first improvement to the magnetostrictive fiber optic interferometric sensor was adopted from a technique employed for an optical fiber hydrophone. In September of 1980, Jackson and others at the Naval Research Laboratory, published a report concerning the utilization of a piezoelectric cylinder to maintain the operation of a fiber optic interferometer at the quadrature point (15:2926-2929). An interferometer is most sensitive to changes in the relative phase of the propagating light intensity when operated at the quadrature point; this concept is illustrated in Figure II.1.

In their paper, they described attaching the reference fiber and the sensor fiber around piezoelectric cylinders whose diameter changes with an applied voltage. By changing the applied voltage to the piezoelectric cylinder, the relative phase

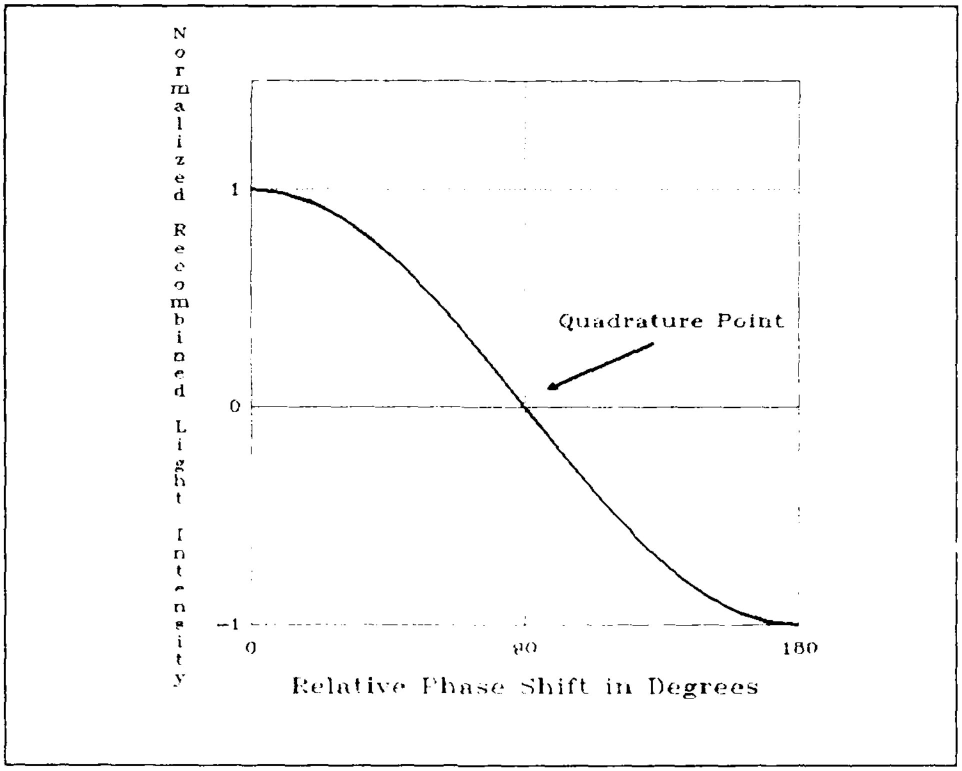

Figure II.1. Quadrature Operation

of the light in one arm could be changed until the quadrature point was obtained. For optimum operation of the sensor, the ability to change the relative phase of the output signal is necessary for two reasons. First, the lengths of the sensor and reference arms cannot be precisely cut to within one wavelength of the excitation source. Second, when the sensor arm is coated with a magnetostrictive material, the sensor arm will change dimensions, depending upon the thermal coefficient of expansion of the material and the ambient temperature conditions. In the interferometer they fabricated, the relative phase of the light propagating in the two arms could be varied from 10^{-5} to 1 radian. The phase change was linear at a rate of 2π per volt applied to the piezoelectric cylinder.

Materials Investigation

Once Dandridge and others had proven that the sensor idea would work in the laboratory, many scientists began investigating improvements to the sensor's performance. The use of metallic glasses as the magnetostrictive material in the sensor arm has been identified as one of the major achievements in the development of the sensor (10:57). Koo and Sigel of the Naval Research Laboratory first reported the use of metallic glasses as the magnetostrictive material in July 1982 (16:334-336). In their paper, they describe sensor arms fabricated by bonding fiber optic cables to strips of commercially available metallic glasses, such as 2605 SC produced by the Allied Chemical Company. They observed that annealing the metallic glass sensor arms affected the performance of the sensor. The reported minimum detectable magnetic flux density was 5×10^{-9} G for each one meter length of coated optical fiber (with an applied 1 kHz magnetic field).

Recent Patent

Although fiber optic magnetic field sensors are close to achieving the theoretical minimum detectable magnetic field, many laboratories are continuing to investigate methods to improve the sensor's performance. The SpecTran Corporation received a patent in 1987 for a unique method of bonding the magnetostrictive

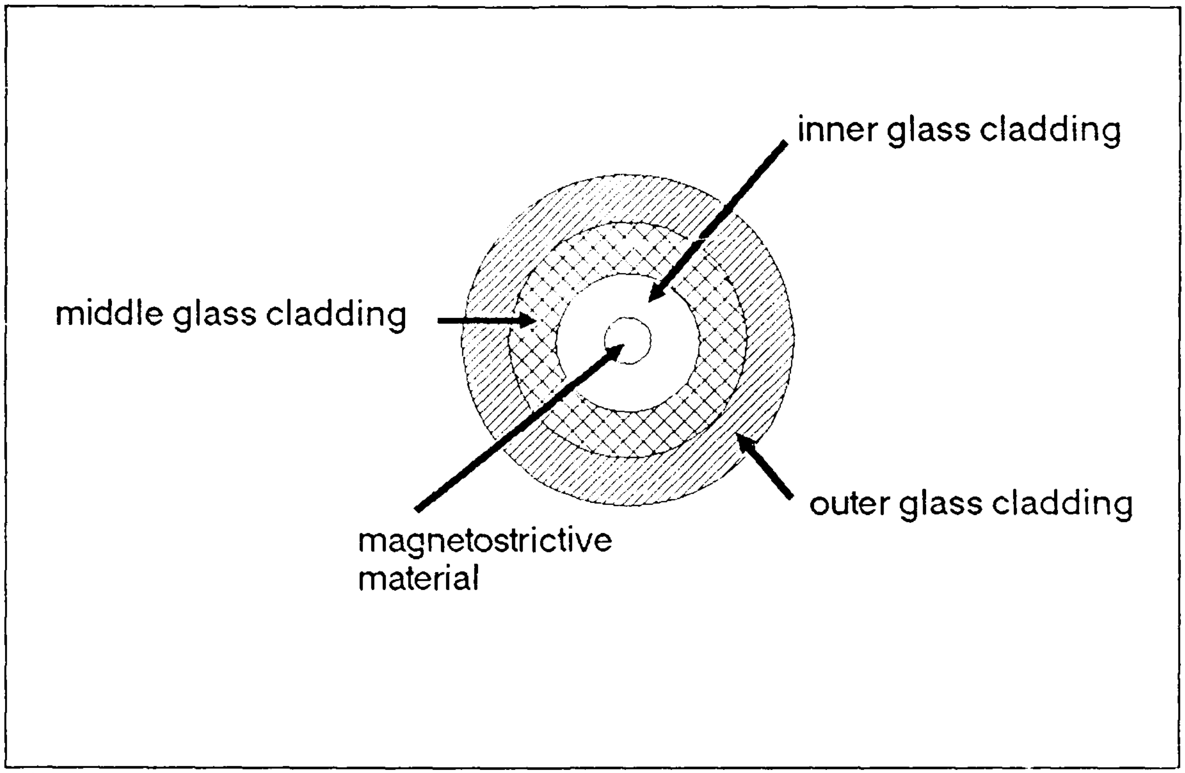

Figure II.2. SpecTran Corporation's Sensor Arm Design (17:97)

material to the fiber optic cable in the sensor arm (17:97). SpecTran's method of material-fiber bonding requires a new type of fiber optic cable that is illustrated in Figure II.2. The conventional fiber optic cable used in the sensor consists of a concentric arrangement of a light carrying glass core, glass outer cladding, and the magnetostrictive jacket. On the other hand, SpecTran's sensor arm fiber optic cable consists of a central core of magnetostrictive material, an inner glass cladding, a middle light carrying glass cladding, and finally, an outer glass cladding. By placing the magnetostrictive material inside the fiber optic cable instead of outside the cable, SpecTran predicts that the fiber optic cable will be more sensitive to length changes induced by an applied magnetic field. SpecTran has not published any performance results to date.

Current Work

In addition to new fiber-material bonding techniques, many laboratories are continuing to research new materials and new sensor configurations. An example of the current research directed at detecting biomagnetic fields is the work being conducted at the American Research Corporation of Virginia. Previously, they fabricated a sensor using fiber optic cables epoxied to bulk metallic glass and achieved a minimum detectable magnetic flux density of 1.4×10^{-4} G at 25 Hz for a sensor arm having a one meter coated length (5:36). Their current research involves the investigation of magnetostrictive materials and signal processing techniques (18:2). They are investigating vapor deposition and annealing of metallic glasses and fabricating new sensor arms using Terfenol, a rare earth magnetic alloy ($Tb_{0.3}Dy_{1.7}Fe_{2.9}$), as the magnetostrictive material. The use of lock-in amplifiers is being studied as one method to improve sensitivity. The lock-in amplifier is used to amplify only those signals from the light detector at the frequency of the applied magnetic field.

III. Theoretical Analysis

This chapter contains the theory that is pertinent to the sensor's performance and evaluation. The chapter begins with a discussion of the concepts used to design the Helmholtz coil. Once the method of generating the magnetic field is explained, the magnetostrictive materials, which sense the magnetic field, are described. The major component in the interferometer, the fiber optic cable, is then described as an introduction to a discussion of light propagation in a cylindrical waveguide. Next, the theory concerning an interferometer is presented. The results of the chapter are summarized in a section listing the critical performance parameters of the sensor, which is followed by the intended sensor arm designs for this research project.

Helmholtz Coil Design (19:152-158)

In order to evaluate the performance of the magnetostrictive fiber optic sensor, the biomagnetic flux density will be simulated using a Helmholtz coil, which consists of two coils of equal size arranged perpendicular to a common axis as illustrated in Figure III.1. The Helmholtz coil is often used in scientific research to produce a relatively uniform magnetic field whose magnitude is controlled by the amount of current flowing through the two coils, the number of turns in each coil, the radius of each coil, and the distance separating them.

The magnetic field generated by a Helmholtz coil can be explained using Figure III.2 and the Biot-Savart law which

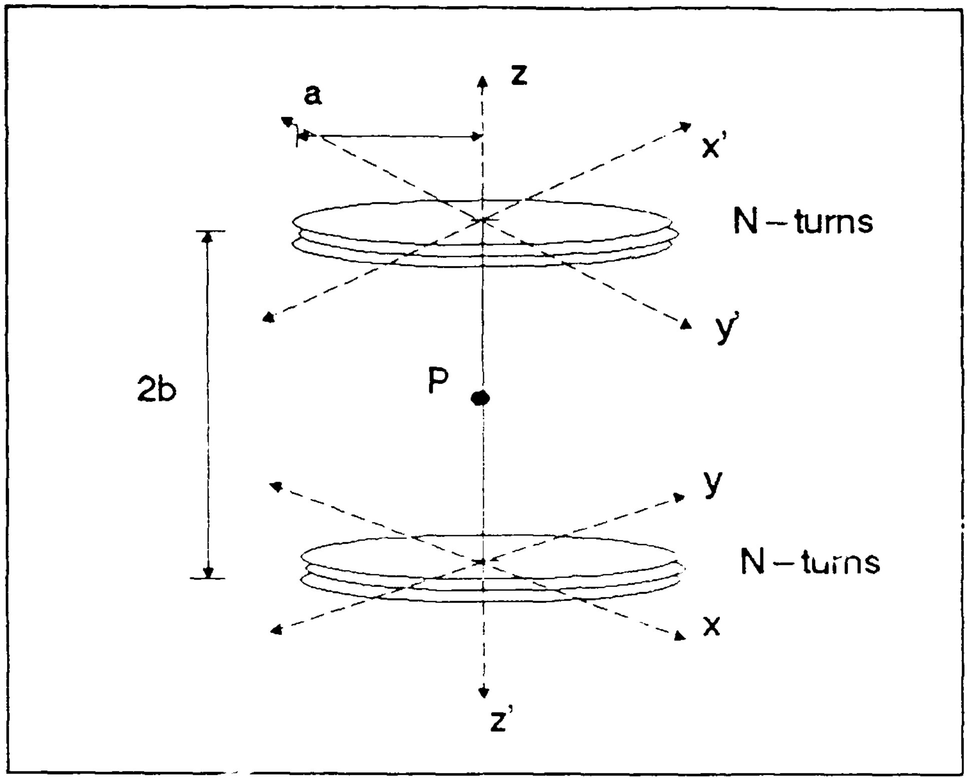

Figure III.1. Helmholtz Coil (19:156)

states (bold indicates vector quantity):

$$\mathbf{B}(\mathbf{r}_2) = \frac{\mu_0 I_1}{4\pi} \oint_1 \frac{\mathbf{dl}_1 \times (\mathbf{r}_2 - \mathbf{r}_1)}{|\mathbf{r}_2 - \mathbf{r}_1|^3} \qquad (1)$$

where,

$\mathbf{B}(\mathbf{r}_2)$ = magnetic flux density vector at a point of interest on coil 2

μ_0 = permeability of free space

I_1 = magnitude of the current in coil 1

$\mathbf{r}_1$ = vector measured from an arbitrary reference point to a point on coil 1

$\mathbf{r}_2$ = vector measured from an arbitrary reference point to a point of interest on coil 2

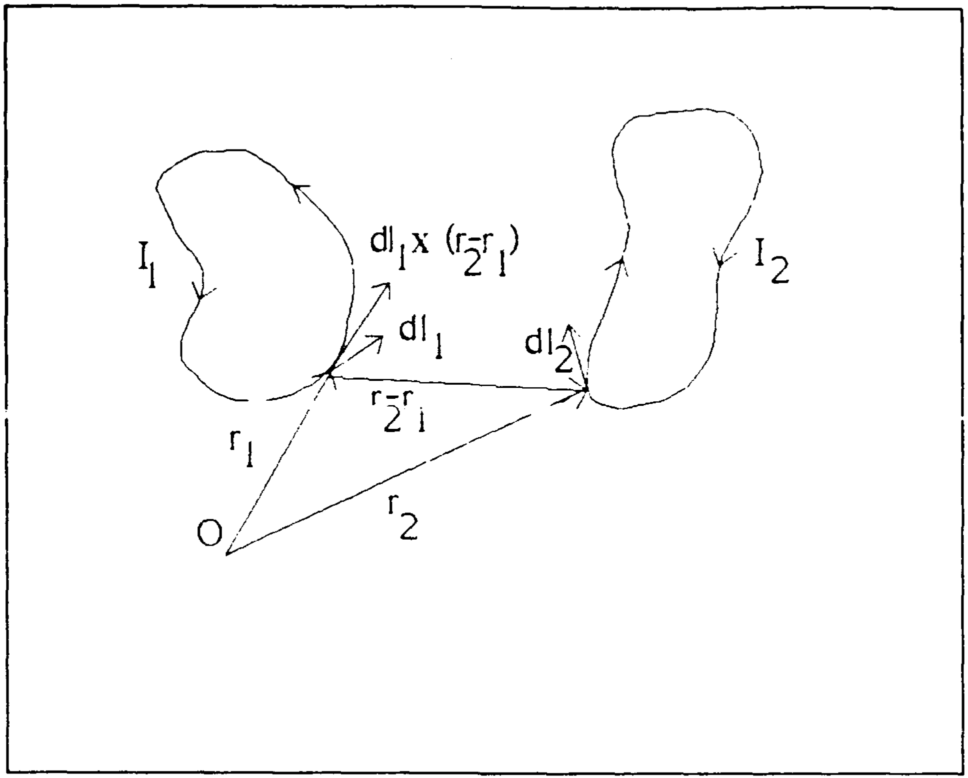

Figure III.2. Biot-Savart Law Geometry (19:153)

$\mathbf{dl}_1$ = vector line integral increment.

In order to describe the magnetic flux density that can be generated in a multiple-turn Helmholtz coil, the Biot-Savart law is first applied to determine the on-axis magnetic flux density of a single-turn of wire with the geometry shown in Figure III.3. Since the magnetic flux density for off-axis points cannot be calculated in closed form, numerical techniques are used, and they will be explained following the on-axis calculation. Based on the geometry of the problem (Figure III.3), the following substitutions into equation 1 can be made:

$\mathbf{dl}_1 = a d\theta(-\mathbf{i}\sin\theta + \mathbf{j}\cos\theta)$

$\mathbf{r}_2 - \mathbf{r}_1 = -\mathbf{i}a\cos\theta - \mathbf{j}a\sin\theta + \mathbf{k}z$

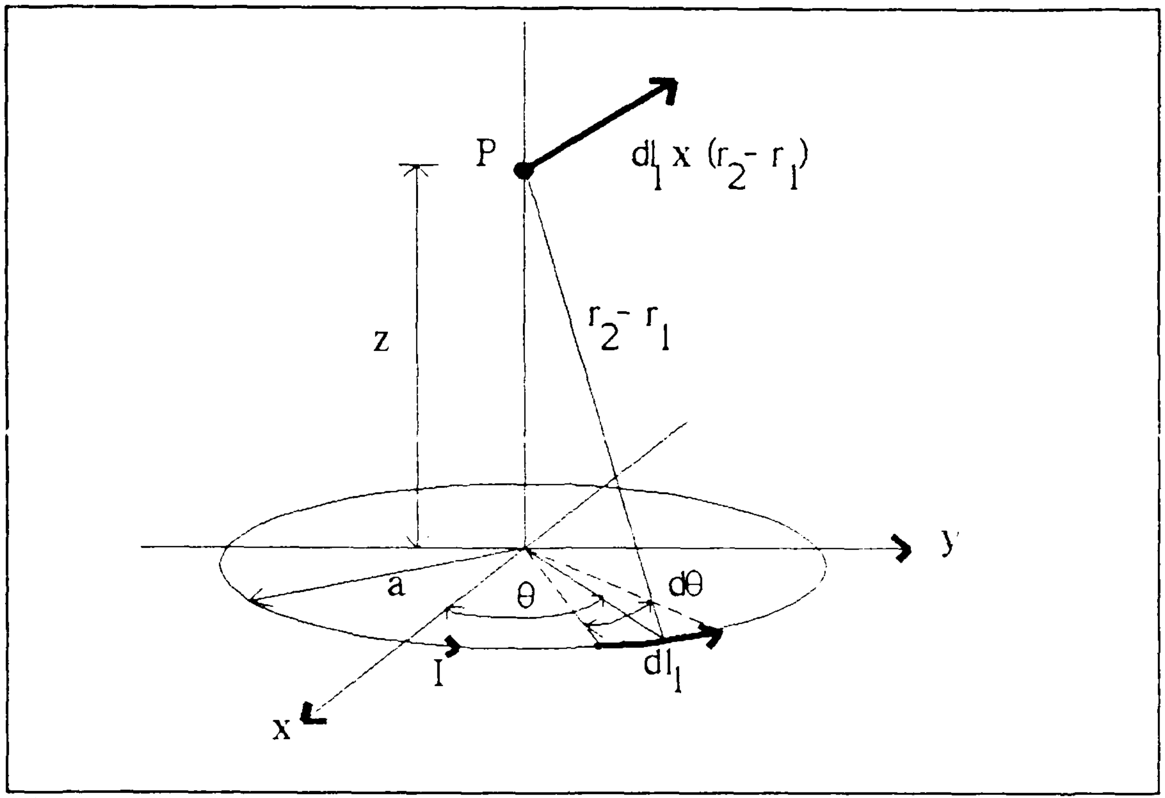

Figure III.3. Axial Magnetic Flux Density for a Single-Turn of Wire (19:155)

$$|\mathbf{r}_2 - \mathbf{r}_1| = (a^2 + z^2)^{1/2}.$$

Thus, with the substitutions, the Biot-Savart law for the single-turn of wire becomes:

$$\mathbf{B}(z) = \frac{\mu_0 I}{4\pi} \int_0^{2\pi} \frac{(\mathbf{i}za\cos\theta + \mathbf{j}za\sin\theta + \mathbf{k}a^2)}{(z^2 + a^2)^{3/2}}\, d\theta \qquad (2).$$

Using the fact that:

$$\int_0^{2\pi} \sin\theta d\theta = \int_0^{2\pi} \cos\theta d\theta = 0,$$

equation 2 simplifies to:

$$\mathbf{B}(z) = \frac{\mu_0 I a^2}{2(z^2 + a^2)^{3/2}}\, \mathbf{k} \qquad (3).$$

Consequently, this equation can be used to predict the magnetic field produced by two circular on-axis coils with the same radius. Using the geometry shown in Figure III.1, the magnetic flux density at a point on-axis between the two N-turn coils contributed from the N-turn lower coil is given by:

$$\mathbf{B}(z) = \frac{N\mu_o I a^2}{2(z^2 + a^2)^{3/2}} \mathbf{k} \qquad (4).$$

To determine the magnetic flux density contribution from the upper N-turn coil, an alternate reference system is used. The new z-coordinate origin, z', is located 2b above z as shown in Figure III.1. The magnetic flux density at a point on-axis between the two N-turn coils that is contributed from the upper N-turn coil is given by:

$$\mathbf{B}(z) = \frac{N\mu_o I a^2}{2(z'^2 + a^2)^{3/2}} \mathbf{k} \qquad (5).$$

Since z' = 2b-z, equation (5) can be rewritten as:

$$\mathbf{B}(z) = \frac{N\mu_o I a^2}{2((2b-z)^2 + a^2)^{3/2}} \mathbf{k} \qquad (6).$$

Combining the two expressions for the magnetic flux density contributions from the upper and lower N-turn coils (equations 4 and 6) yields the magnitude of the total magnetic flux density at a point on-axis which is given by:

$$B(z) = \frac{N\mu_o I a^2}{2} \left\{ \frac{1}{(z^2 + a^2)^{3/2}} + \frac{1}{[(2b-z)^2 + a^2]^{3/2}} \right\} \qquad (7).$$

The purpose of the Helmholtz coil is to produce a uniform magnetic field. By determining the necessary conditions for the first and second derivatives (with respect to z) of equation (7) to vanish, the values of coil separation (2b) and coil radius (a) can be optimized for the most uniform region of the magnetic field. The first derivative of the above expression with respect to z is given by:

$$\frac{dB}{dz} = \frac{N\mu_o Ia^2}{2}\left\{-\frac{3z}{(z^2 + a^2)^{5/2}} - \frac{3(z-2b)}{[(2b-z)^2 + a^2]^{5/2}}\right\} \qquad (8).$$

This expression is zero when z = b. Differentiating equation 8 with respect to z yields:

$$\frac{d^2B}{dz^2} = -\frac{3N\mu_o Ia^2}{2}\left\{\frac{1}{(z^2 + a^2)^{5/2}} - \frac{5z^2}{(z^2+a^2)^{7/2}}\right.$$

$$\left. + \frac{1}{[(2b-z)^2 + a^2)]^{5/2}} - \frac{5(z-2b)^2}{[(2b-z)^2 + a^2]^{7/2}}\right\} \qquad (9).$$

When z=b, equation 9 simplifies to:

$$\left.\frac{d^2B}{dz^2}\right|_{z=b} = -\frac{3N\mu_o Ia^2}{2}\left\{\frac{2a^2 - 8b^2}{(b^2 + a^2)^{7/2}}\right\} \qquad (10).$$

It is noted that the second derivative evaluated with z=b vanishes when a=2b. These results indicate that the coil radius should be equal to the coil separation. Under these conditions, the magnetic flux density at the midpoint between the coils is given by:

$$\mathbf{B}(z=\tfrac{1}{2}a) = \frac{8\mu_o NI}{a5^{3/2}}\mathbf{k} \qquad (11).$$

A Taylor series approximation for the magnetic flux density indicates how slowly it changes near the midpoint. The Taylor series approximation using the first five terms is given by:

$$\mathbf{B}(z) = \mathbf{B}(z=\tfrac{1}{2}a)\left\{1 - \frac{144}{125}\left(\frac{z - \frac{1}{2}a}{a}\right)^4\right\} \qquad (12),$$

where it is noted that the middle three terms of the expansion vanish. The above expression shows that for a position equal to a distance (a/10) measured relative to the midpoint along the center-line, the magnetic flux density is 0.99988 of its midpoint value.

To illustrate how slowly the magnetic flux density changes in the axial direction, the magnetic flux density was calculated for the specific Helmholtz coil fabricated for this experiment (an average coil radius of 10.5 cm with 250 turns of wire). For a current flow of 200 mA, Figure III.4 shows the axial variation of the magnetic flux density between the two coils. The axial magnetic flux density at the midpoint between the coils was calculated to be 4.28 Gauss (G).

To examine the change in the magnetic flux density in the off-axis direction, numerical methods were used since a closed-form expression does not exist. The starting point for the calculation is the differential form of the Biot-Savart law; that is:

$$\mathbf{dB}(\mathbf{r}_2) = \frac{\mu_o I_1}{4\pi} \frac{\mathbf{dl}_1 \times (\mathbf{r}_2 - \mathbf{r}_1)}{|\mathbf{r}_2 - \mathbf{r}_1|^3} \quad (13),$$

which utilizes the geometry of Figure III.2. For the single-turn coil geometry of Figure III.3, the following substitutions can be made:

$$\mathbf{r}_1(\theta) = \mathbf{i}a\cos\theta + \mathbf{j}a\sin\theta$$

$$\mathbf{r}_2(\theta) = \mathbf{j}y + \mathbf{k}z$$

$$\mathbf{dl}(\theta) = -\mathbf{i}a\cos\theta + \mathbf{j}a\sin\theta$$

where θ, y, and z are specified for a single point on the coil.

As θ, y, and z are varied for points around the coil, the

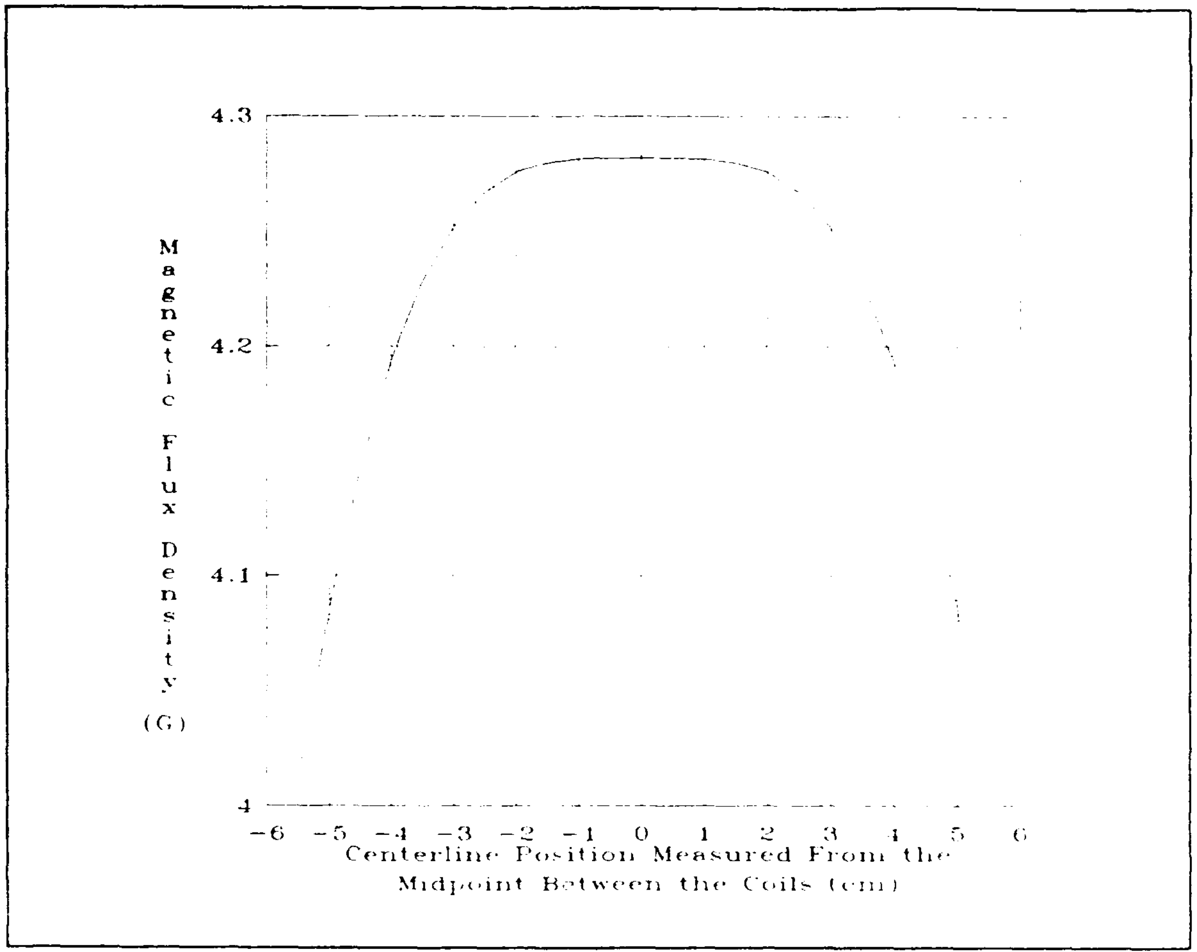

Figure III.4. Axial Magnetic Flux Density for a Helmholtz Coil

magnetic flux density at the observation point (P) is calculated by summing the contributions for all the points on the circle's circumference. This calculation was accomplished using the numerical values discussed above for the Helmholtz coil to be used in the sensor's experimental performance evaluation. The results, produced using MATHCAD software, are illustrated in Figure III.5. The computer program, attached as Appendix B, provides vector expressions for the magnetic flux density for the off-axis points, and it is noted that the vector quantities are no longer only in the z-direction.

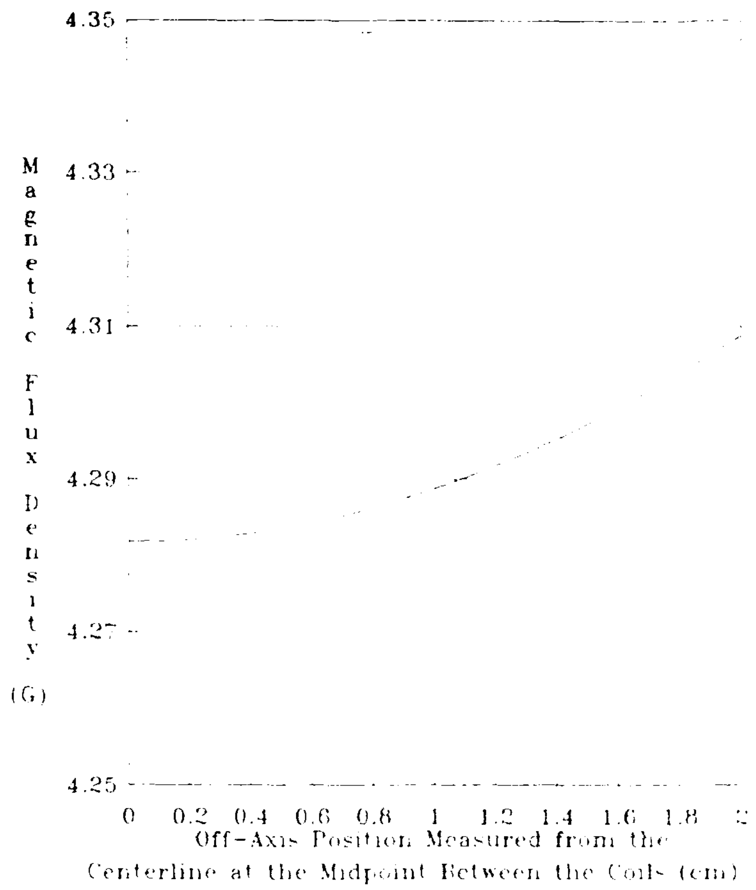

Figure III.5. Off-Axis Magnetic Flux Density from a Helmholtz Coil

Figure III.5 depicts a plot of the magnitude of the magnetic flux density vector for the off-axis points. The on-axis value of the magnetic flux density that was numerically calculated agrees with the value calculated in closed form to six decimal places. This calculation illustrates that any small off-axis errors that might be involved concerning the positioning of the fiber optic cable along the center-line of the Helmholtz coil will not drastically affect the magnetic flux density that the fiber optic cable will experience.

This research effort required a Helmholtz coil that could not only generate a small magnetic flux density to evaluate the performance of the sensor, but also a large flux density to permit its calibration using a state of the art laboratory magnetometer. The expression for the magnetic flux density at the center point between the coils (equation 11) illustrates the design trade-offs that exists between the following coil parameters:

i) number of turns (N),

ii) current (I), and

iii) coil radius (a).

Equation 11 is repeated here:

$$\mathbf{B}(z=\tfrac{1}{2}a) = \frac{8\mu_0 NI}{a5^{3/2}}\mathbf{k} \qquad (11).$$

Other constraints imposed on the design included limiting:

i) the current to 550 mA,

ii) power dissipation due to the wire's resistance to 2.5 W, and

iii) the maximum number of turns of wire to 250.

Based on these constraints and trade-offs, the final design consisted of a 10.5 cm radius, multiply-tapped coil that was wound with 18 gauge magnet wire. The taps at 250-, 100-, 10-, and 2-turns facilitated flexibility in generating the magnetic flux densities of interest. For calibration purposes, the Helmholtz coil was configured with 250-turns, and AC and DC currents ranging from 550 to 50 mA were applied to produce magnetic field densities spanning 11.78 to 1.07 G.

For a practical Helmholtz coil with many turns of wire, the coil separation and coil radius are not constant for all the turns of wire due to the finite size of the wire in each coil. Consequently, the values of coil separation and coil radius in the above calculations are average values. Figures III.6 and III.7 show the effects of the extreme values of coil separation (8 to 13 cm) and radius (10 to 11 cm) for the axial magnetic flux density relative to the center position between the coils. It was assumed that the average values contributed a negligible variation.

Magnetostrictive Materials

Now that the mechanism for generating the magnetic fields has been explained, the material that reacts to the magnetic field is described. Magnetostriction refers to the small change in the dimensions of ferromagnetic materials that are exposed to an external magnetic field (19:627). For this research project, the change in the length of the material applied to the outer surface of a fiber optic cable is the important parameter. This change in length is typically on the order of parts per million. This section begins by describing the magnetic nature of ferromagnetic materials. The origin of magnetostriction is then explained, which is followed by a discussion of enhancing the magnetostrictive property of materials.

Ferromagnetic Materials. To understand ferromagnetic materials, it is necessary to understand the source of magnetic

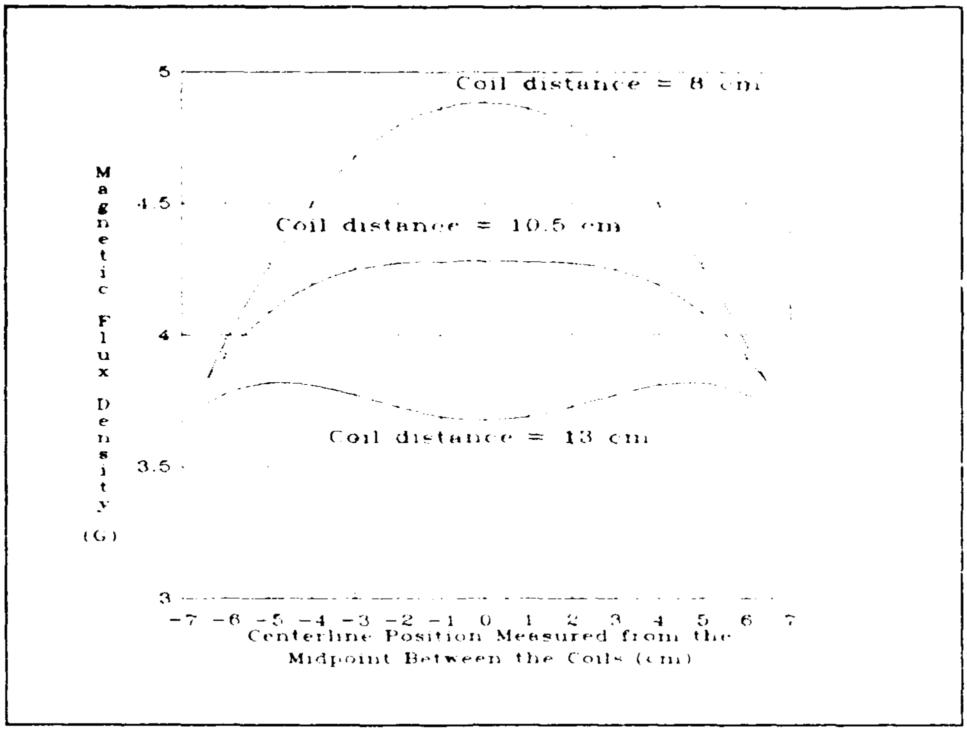

Figure III.6. Variations of Magnetic Flux Density with Coil Separation

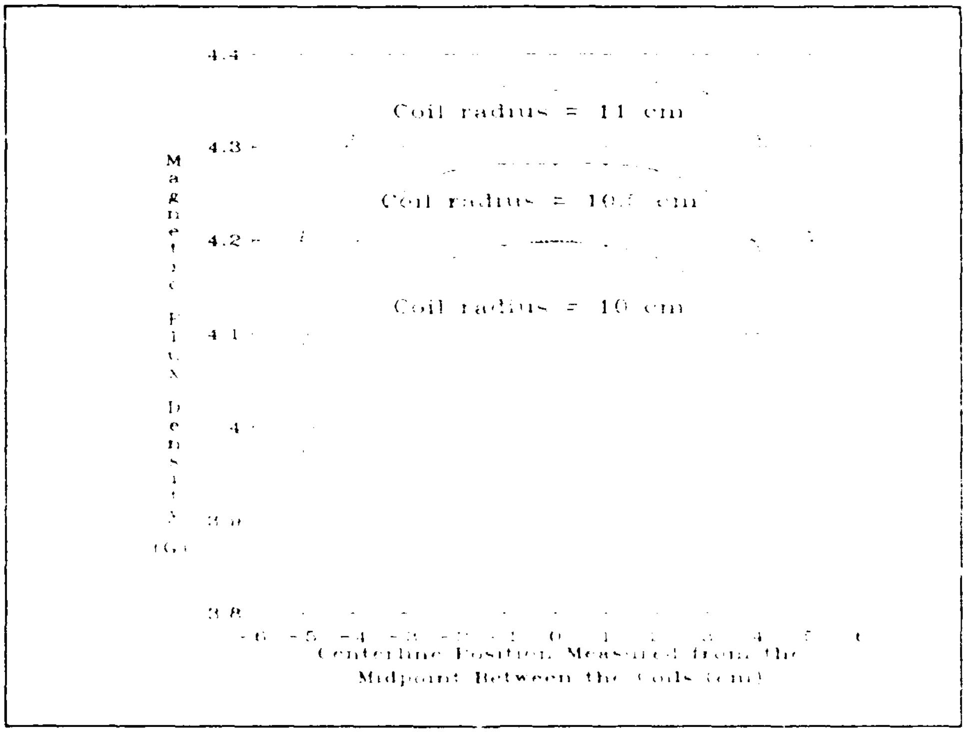

Figure III.7. Variations of Magnetic Flux Density with Coil Radius fields in materials. When an electron orbits the nucleus of an atom, it produces a magnetic field just as the current flowing through a conductor produces a magnetic field. The electron itself also produces a magnetic field from its inherent spin. In nonmagnetic materials, the magnetic field produced by the orbit and spin of one electron is cancelled by the magnetic field of an oppositely oriented electron to produce a net zero magnetic field in the bulk material. However, in certain materials like cobalt, nickel, and iron, the magnetic field contributions from each atom contribute to a net average external magnetic field (2:210). A quantum effect referred to as the exchange coupling between atoms in a ferromagnetic material, locks their magnetic moments in a parallel configuration, and this regions is called a domain (2:214). The size of the domains vary, but average 0.1 to 0.01 cm across in iron. Domains are separated by boundaries called Block walls which are approximately fifty nm thick in iron (21:66). Block walls are composed of atoms whose magnetic moment orientation transitions between those of neighboring domains (20:815). Above a certain temperature, known as the Curie temperature, the domains in ferromagnetic materials become indistinct, and the material becomes paramagnetic. The Curie temperature and melting points for the materials of interest are listed in Table III.1. When exposed to an external magnetic field, the magnetic moments in both ferromagnetic and paramagnetic materials tend to align with the external field. When cooled below the Curie temperature, the domains reform to

Table III.1. Curie Temperatures and Melting Points (20:723 and 22:94)

Material	Curie Temperature (°C)	Melting Point (°C)
Co	1130	1492
Fe	770	1535
Ni	358	1453

the characteristic of ferromagnetic materials (2:214).

Magnetostriction. A change in length of ferromagnetic materials occurs when the domains rotate and move as they align with an external magnetic field (20:632). Figure III.8 illustrates a simplified model of magnetostriction. The rectangles represent the magnetic domains, and the arrows symbolize the net magnetic moment. As shown, magnetostriction refers to expansion and contraction. The amount of change in length in a material depends upon the magnetic field. Figure III.9 depicts the fractional change in length ($\lambda = \Delta l/l$) for the materials of interest relative to an externally applied magnetic field.

The direction of the external magnetic field relative to the magnetic moment of a single domain affects the fractional change in length and is given by (20:634):

$$\lambda_1 = 3/2\lambda_s(\cos^2\theta - 1/3) \qquad (14)$$

where λ_1 = observed fractional change in length

λ_s = saturated factional change in length value

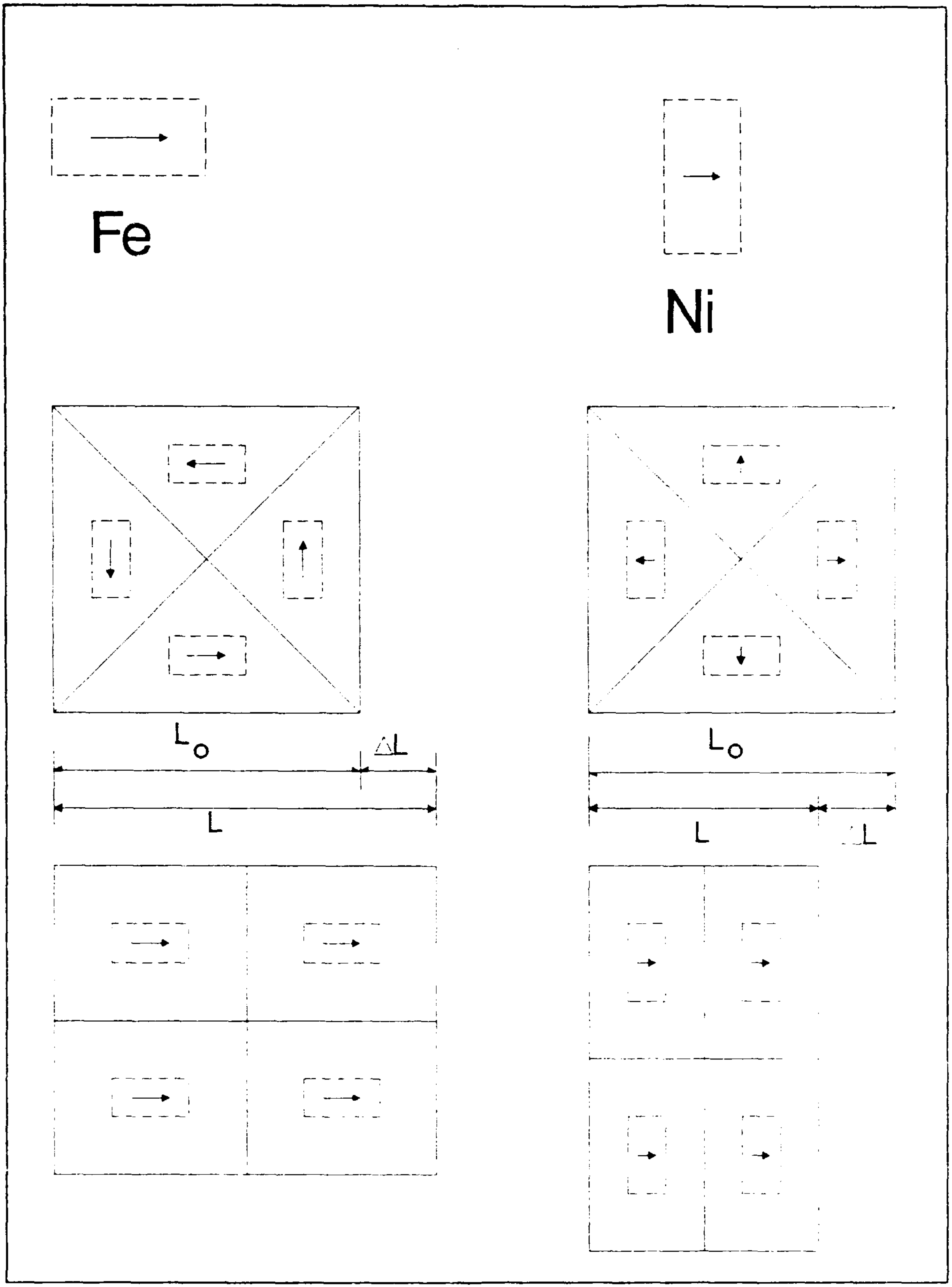

Figure III.8. Magnetostriction Model (23:36 and 20:635)

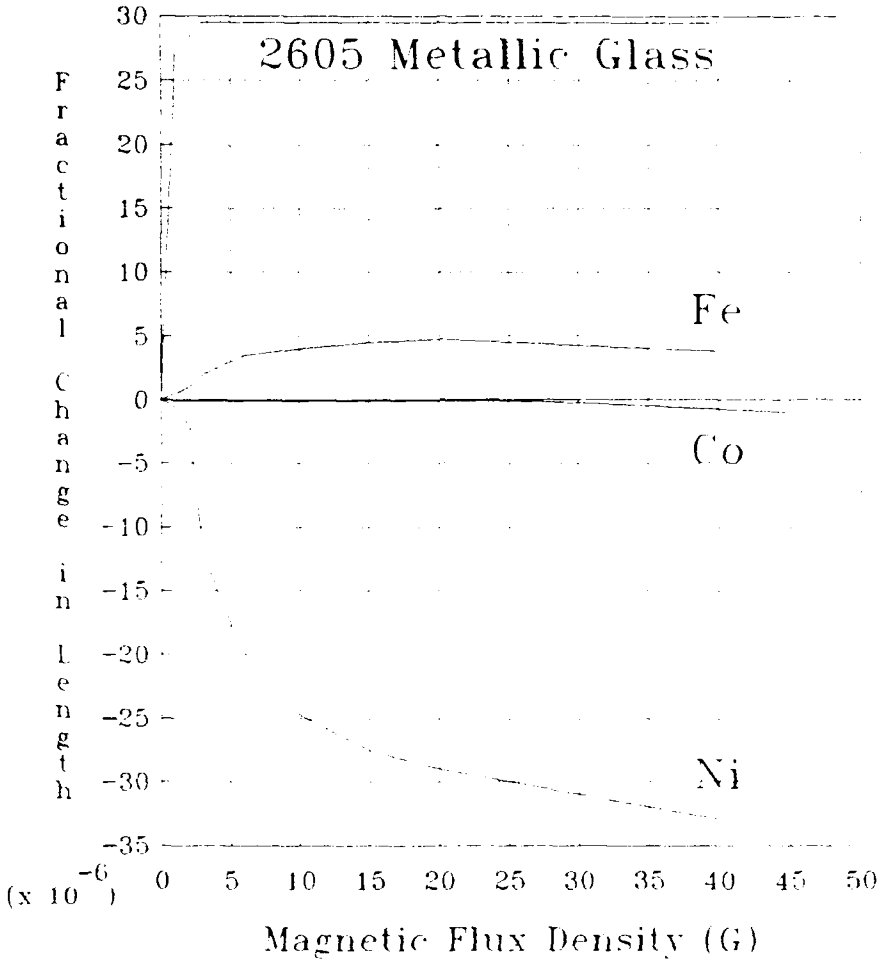

Figure III.9. Magnetostrictive Response (8:7)

θ = angle between the direction of measured change in length and the external magnetic field.

Equation 14 shows that the maximum or saturated value of magnetostriction occurs when the change in length is measured along the direction of the external magnetic field ($\theta = 0^\circ$). The above equation also shows that when the change in length is measured perpendicular to the magnetic field ($\theta = 90^\circ$), the transverse change in length is one half the negative of the longitudinal saturation value.

For an ensemble of domains whose initial magnetic moments are randomly arranged, the single cosine dependence is replaced by its average value. For an initial random distribution of domains and no external magnetic field, $<\cos^2\theta> = 1/3$, which yields no magnetostriction. When a strong external magnetic field is applied, $<\cos^2\theta> = 0$, producing the saturated value of magnetostriction.

If the domains are not initially randomly arranged, the following expression describes the fractional change in length (20:634):

$$\lambda_1 = 3/2\lambda_s(<\cos^2\theta>_{av} - <\cos^2\theta>_o) \tag{15}$$

where $<\cos^2\theta>_{av}$ refers to the final distribution of domains, and $<\cos^2\theta>_o$ refers to the initial distribution of domains. This expression reveals that the magnetostriction is three-halves that of the saturated value, and this result can be obtained if the domains are all originally oriented perpendicular to the external magnetic field.

Optimized Magnetostriction.

As implied in the previous discussion, there are methods that can be used to maximize the amount of magnetostriction. These techniques include material selection and initial orientation the of the domains by stressing the material or thermally annealing the material in the presence of external magnetic fields.

Much of the recent research associated with the fiber optic magnetic field sensor has been focused on developing new magnetostrictive materials. The Allied Chemical Company's 2605SC metallic glass is an example of these new materials. As shown in Figure III.9, the bulk material has a greater value of magnetostriction at low external magnetic fields compared to the elemental metals. This metallic glass is formed from a combination of boron, carbon, iron, and silicon which is quenched from a melt (8:6). This fabrication method limits the use of developing metallic glasses as a magnetostrictive material for the fiber optic magnetic field sensor. Metallic glasses cannot be RF sputtered in thin layers of various geometries and preserve their chemical composition. The magnetostrictive behavior of metallic glasses also changes with time (8:6). While the single elements have smaller magnetostriction values, they were investigated because they can be deposited in thin layers with various geometries. Once these high purity layers of single elements are deposited, they can processed to initially align their magnetic domains.

The first method which can be used to initially orient the magnetic domains of ferromagnetic materials is to apply a stress to the material (20:636). Figure III.10 shows the effect of compression and tension on the magnetostriction of a nickel sample. The data in Figure III.10 shows that the value of magnetostriction varies from zero to three-halves its saturation value without tension. Under tension, the nickel domains were

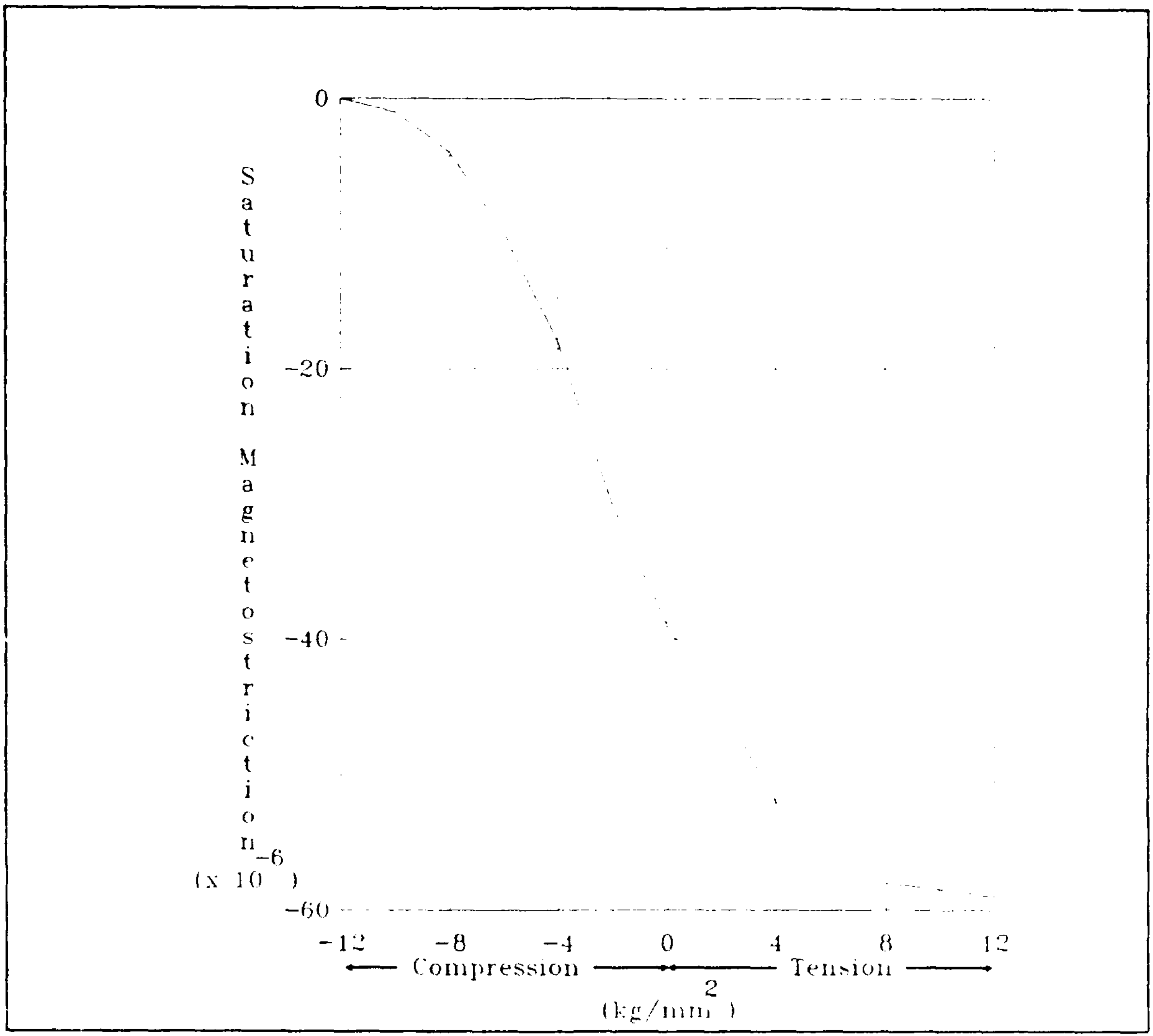

Figure III.10. Magnetostriction of Nickel Under Stress (20:636)

oriented perpendicular to the direction of the magnetic field and under compression, the magnetic field and the domains were aligned parallel. The stress required to align the domains is greater than the forces maintaining alignment of the domains in the unstressed material (20:634). These forces in the unstressed material are attributed to crystal anisotropy. Once an external stress greater than the crystal anisotropy force is applied, the domains align and the magnetostriction is given by:

$$\lambda = 3/2\lambda_s\cos^2\theta \qquad (16)$$

where θ = angle between the external magnetic field and stress. While tension has proven to be effective for domain control, it was not investigated in this research project since the following method of domain control appears more practical for a fiber optic magnetic field sensor.

The second method of domain control is to heat the ferromagnetic material and then allow it to cool in the presence of an external magnetic field (20:637). When the ferromagnetic material is heated past its Curie temperature, the domain boundaries disappear. If the material is then allowed to cool in the presence of an external magnetic field, the domains should reform and be aligned with the external field. Figure III.11 shows the change in magnetostriction for a sample of 68 Permalloy (68% Ni, 32% Fe). Figure III.11 illustrates how the magnetostriction of the material was increased in a direction perpendicular to the annealing field, and how it decreased in a direction aligned with the external field. The graph's abscissa (magnetization) refers to the magnetic dipole moment per volume of the sample (2:217) which is proportional to the magnetic field flux density and has the same units of gauss.

Although not addressed in the literature, it is postulated that the geometrical configuration of the magnetostrictive material may affect its bulk magnetostrictive property. That is, the magnetic domains may rotate more easily if they are not in contact with other domains that are also attempting to move under the influence of an external magnetic field. Therefore, by investigating the influence of the magnetostriction of domain-sized stripes of magnetostrictive material, the magnetostriction of the collection may be greater than that of a uniform coating.

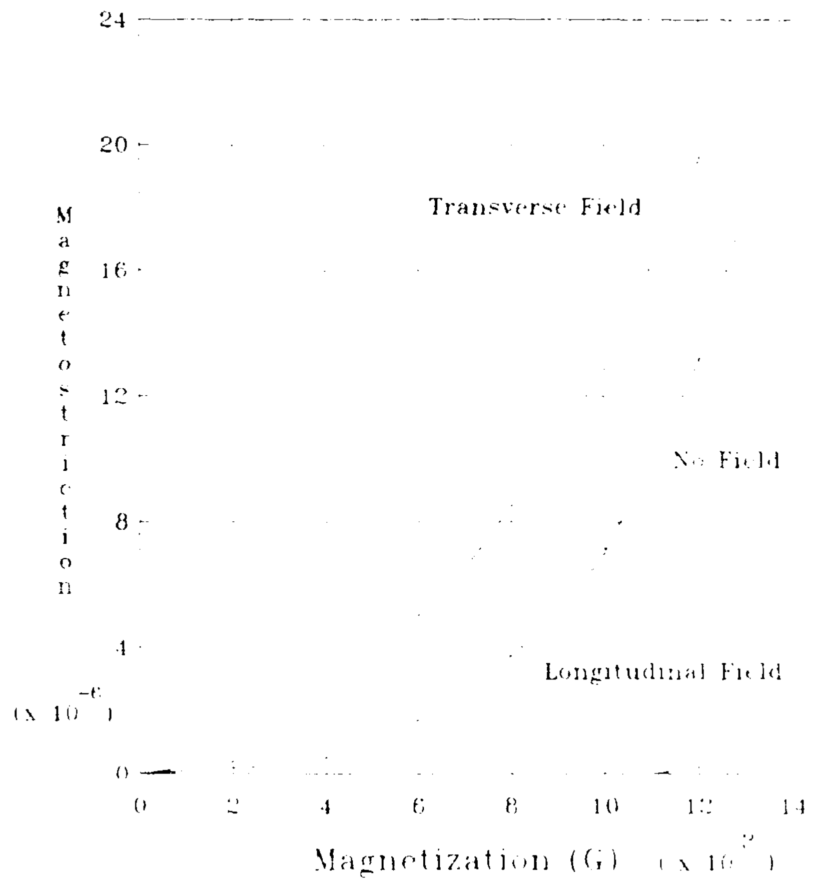

Figure III.11. Effect of Magnetic Annealing on the Magnetostriction Effect (20:638)

Fiber Optic Cables

A description of fiber optic cables, in addition to the discussion of magnetostrictive material, completes the analysis of the components of the sensor arm. The composition of the fiber optic cable directly affects the detection mechanism of the sensor by establishing how the light propagates in the interferometer.

The fiber optic cables used throughout the interferometer are York Technology, Model SM600, single-mode fibers. These fibers are composed of four concentric circular material layers as shown in Figure III.12. The inner core is composed of Ge-doped silicon dioxide (Ge:SiO_2) which has an index of refraction

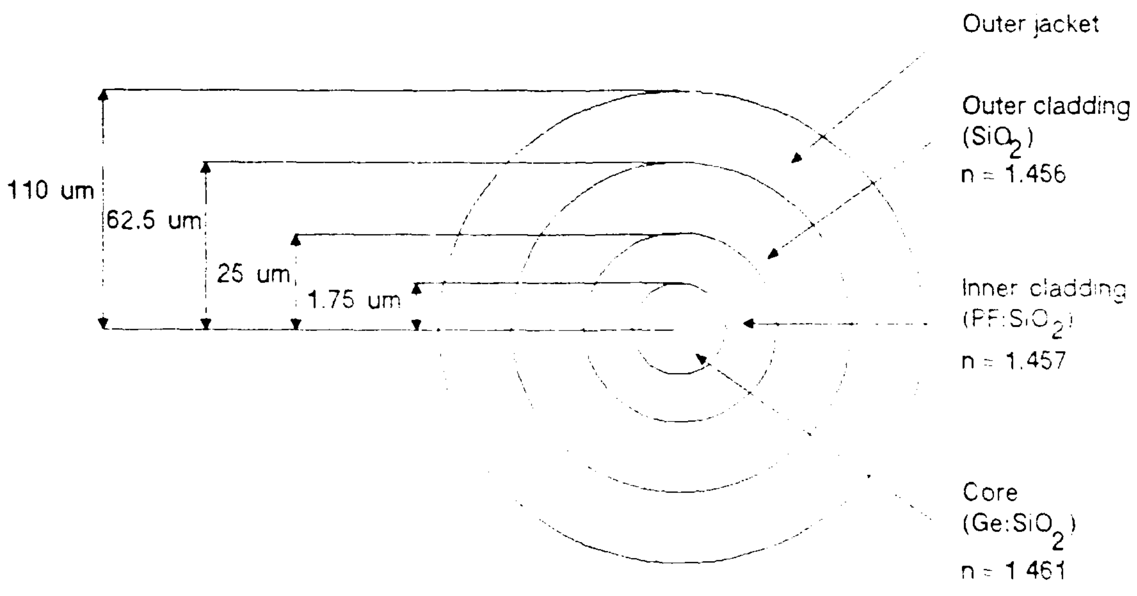

Figure III.12. York Technology, Model SM600, Single-mode Fiber Optic Cable Cross Section (24)

(n) of 1.461 and a radius of 1.75 microns. The outer glass cladding is composed of two parts: an inner cladding and an outer cladding. These two cladding layers are used to achieve a continuously-graded profile of the index of refraction. The inner cladding has a radius of 25 microns and is a phosphorous fluorine-doped silicon dioxide (PF:SiO_2) material, which has an index of refraction of 1.457. The outer cladding is undoped silicon dioxide (SiO_2), which has an index of refraction of 1.456 and a radius of 62.5 microns. The final layer is a jacket of mode absorbing ultraviolet cured acrylate which has a radius of 110 microns. The jacketing material provides mechanical strength and absorbs undesirable light which may propagate in the cladding layers (24).

Under the influence of an external magnetic field, the magnetostrictive material covering the sensor arm will apply a force on the fiber optic cable to change the cable's length. Regardless of the source of the force, the length change of the optical fiber has been shown to be given by (25:102):

$$\Delta L = \frac{FL_o}{EA} \qquad (17),$$

where ΔL = change in length

L_o = initial length

F = magnitude of the applied force

A = cross sectional area of the fiber

E = Young's modulus of the fiber.

This expression indicates that by reducing the cross-sectional area of the fiber, an increase in the change of length will result when the other variables remain constant. The cross-sectional area of the fiber can be reduced by thinning the cladding of the fiber optic cable.

Cylindrical Waveguide Propagation

The optical fiber previously described will serve as a waveguide for laser radiation in the sensor. The choice of an optical source and optical fiber relative to their influence on the sensor's performance will be determined by examining cylindrical waveguide propagation.

Method of Analysis. This section describes the electromagnetic wave propagation phenomena in an optical fiber. The analysis begins by assuming the general case of a time-varying (propagating) electromagnetic wave. These solutions are then substituted into the cylindrical coordinate system representation of Maxwell's equations. All components of the electric and magnetic fields are then found in terms of the electric and magnetic field's z-components. The wave equation is then derived and solved using the separation of variables technique to yield the z-components. Finally, the specific geometry and corresponding boundary conditions of an optical fiber are used to determine the constants generated in the solution of the differential equations. These solutions provide insight into the propagation of the allowed modes.

Maxwell's Equations. For nonmagnetic and nonconducting materials with no enclosed charge, the set of Maxwell's equations which relate the electric field (**E**), magnetic field (**H**), permittivity ($\epsilon=\epsilon_0\epsilon_r$), and permeability ($\mu=\mu_0$) may be represented as (bold characters indicate vector quantities) (2:374):

$$\nabla \times \mathbf{H} = \epsilon \frac{d\mathbf{E}}{dt} \quad (18)$$

$$\nabla \times \mathbf{E} = -\mu \frac{d\mathbf{H}}{dt} \quad (19)$$

$$\nabla \cdot \mathbf{E} = 0 \quad (20)$$

$$\nabla \cdot \mathbf{H} = 0 \quad (21).$$

(The italic d (d) denotes a partial derivative in this analysis). The electric and magnetic fields of the laser radiation are assumed to be propagating along the z-direction of the optical fiber and are of the form (26:55):

$$\mathbf{E} = \mathbf{E}_0(r,\theta)\exp[j(\omega t-\beta z)] \quad (22)$$

$$\mathbf{H} = \mathbf{H}_0(r,\theta)\exp[j(\omega t-\beta z)], \quad (23)$$

where ω = angular frequency

β = axial phase constant.

Substituting the assumed form of the electric and magnetic fields (equations 22 and 23) into the set of Maxwell's general equations (equations 18, 19, 20, and 21) yields (2:374):

$$\nabla \times \mathbf{H} = j\omega\epsilon\mathbf{E} \quad (24)$$

$$\nabla \times \mathbf{E} = -j\omega\mu\mathbf{H} \quad (25)$$

$$\nabla \cdot \mathbf{E} = 0 \quad (26)$$

$$\nabla \cdot \mathbf{H} = 0 \quad (27).$$

<u>**E** and **H** Field Components</u>. Using the expressions for the curl and divergence in cylindrical coordinates, equations 24 and 25 can be expanded as:

$$\mathbf{r}\left[\frac{dH_z}{rd\theta} - \frac{dH_\theta}{dz}\right] + \mathbf{\Theta}\left[\frac{dH_r}{dz} - \frac{dH_z}{dr}\right] + \mathbf{z}\frac{1}{r}\left[\frac{drH_\theta}{dr} - \frac{dH_r}{d\theta}\right] = j\omega\epsilon\mathbf{E} \qquad (28)$$

and

$$\mathbf{r}\left[\frac{dE_z}{rd\theta} - \frac{dE_\theta}{dz}\right] + \mathbf{\Theta}\left[\frac{dE_r}{dz} - \frac{dE_z}{dr}\right] + \mathbf{z}\frac{1}{r}\left[\frac{drE_\theta}{dr} - \frac{dE_r}{d\theta}\right] = -j\omega\mu\mathbf{H} \qquad (29).$$

Each component of equations 28 and 29 is a separate equation. Evaluating the partial derivatives where possible, the six equations become (27:49):

$$\frac{dH_z}{rd\theta} - \frac{dH_\theta}{dz} = \frac{dH_z}{rd\theta} + j\beta H_\theta = j\omega\epsilon E_r \qquad (30)$$

$$\frac{dH_r}{dz} - \frac{dH_z}{dr} = -j\beta H_r - \frac{dH_z}{dr} = j\omega\epsilon E_\theta \qquad (31)$$

$$\frac{drH_\theta}{rdr} - \frac{dH_r}{rd\theta} = j\omega\epsilon E_z \qquad (32)$$

$$\frac{dE_z}{rd\theta} - \frac{dE_\theta}{dz} = \frac{dE_z}{rd\theta} + j\beta E_\theta = -j\omega\mu H_r \qquad (33)$$

$$\frac{dE_r}{dz} - \frac{dE_z}{dr} = -j\beta E_r - \frac{dE_z}{dr} = -j\omega\mu H_\theta \qquad (34)$$

$$\frac{drE_\theta}{rdr} - \frac{dE_r}{rd\theta} = -j\omega\mu H_z \qquad (35).$$

The E_r, E_θ, H_r, H_θ components can be conveniently expressed in terms of the E_z and H_z components. That is, from equation 30, E_r can be expressed as:

$$E_r = -\frac{jdH_z}{\omega\epsilon rd\theta} + \frac{\beta H_\theta}{\omega\epsilon} \qquad (36).$$

Correspondingly, from equation 34, H_θ can be expressed as:

$$H_\theta = \frac{\beta E_r}{\omega\mu} - \frac{jdE_z}{\omega\mu dr} \qquad (37).$$

Substituting equation 37 into equation 36 yields:

$$E_r = -\frac{j dH_z}{\omega\epsilon r d\theta} + \frac{\beta}{\omega\epsilon}\left[\frac{\beta E_r}{\omega\mu} - \frac{j dE_z}{\omega\mu dr}\right]$$

$$E_r\left[1 - \frac{\beta^2}{\omega^2\epsilon\mu}\right] = -\frac{j dH_z}{\omega\epsilon r d\theta} - \frac{j\beta dE_z}{\omega^2\mu\epsilon dr}$$

$$E_r = -\frac{j}{\omega\epsilon r[1-\beta^2/(\omega^2\epsilon\mu)]}\frac{dH_z}{d\theta} - \frac{j\beta}{\omega^2\mu\epsilon[1-\beta^2/(\omega^2\epsilon\mu)]}\frac{dE_r}{dr} \qquad (38).$$

The following identities can then be used to simplify the above expression (27:50):

$k^2 = \omega^2\epsilon_0\mu_0$ (wave number squared)

$\beta' = k^2n^2 - \beta$ (transverse wave number) (39)

$n = (\mu_r\epsilon_r)^{1/2} = \epsilon_r^{1/2}$ (index of refraction).

Therefore, equation 38 now can be written as:

$$E_r = \frac{-j}{\beta'^2}\left[\frac{\omega\mu dH_z}{r d\theta} + \frac{\beta dE_z}{dr}\right] \qquad (40).$$

The other components can be derived in a similar manner, and they are given as (27:50):

$$E_\theta = \frac{-j}{\beta'^2}\left[\frac{\beta dE_z}{r d\theta} - \frac{\omega\mu dH_z}{dr}\right] \qquad (41)$$

$$H_r = \frac{-j}{\beta'^2}\left[\frac{\beta dH_z}{dr} - \frac{\omega\epsilon dE_z}{r d\theta}\right] \qquad (42)$$

$$H_\theta = \frac{-j}{\beta'^2}\left[\frac{\beta dH_z}{r d\theta} + \frac{\omega\epsilon dE_z}{dr}\right] \qquad (43).$$

Wave Equation. All the components of the electric and magnetic fields can be specified once E_z and H_z are known. The z-components can be determined using the wave equation. To derive the wave equation for the electric field, equations 42 and 43 are substituted into equation 32 which yields:

$$j\omega\epsilon E_z = \frac{dr}{r dr}\left[\frac{-j}{\beta'^2}\left(\frac{\beta dH_z}{r d\theta} + \frac{\omega\epsilon dE_z}{dr}\right)\right] - \frac{d}{r d\theta}\left[\frac{-j}{\beta'^2}\left(\frac{\beta dH_z}{dr} - \frac{\omega\epsilon dE_z}{r d\theta}\right)\right]$$

$$j\omega\epsilon E_z = -\frac{j\ \beta d^2H_z}{r\beta'^2 dr d\theta} - \frac{j\omega\epsilon d r dE_z}{\beta'^2 r dr^2} + \frac{j\beta d^2H_z}{r\beta'^2 d\theta dr} - \frac{j\omega\epsilon d^2E_z}{\beta'^2 r^2 d\theta^2}$$

$$j\omega\epsilon E_z = -\frac{j\omega\epsilon d}{\beta'^2 r dr}\left[\frac{r dE_z}{dr}\right] - \frac{j\omega\epsilon d^2E_z}{\beta'^2 r^2 d\theta^2}$$

$$j\omega\epsilon E_z = -\frac{j\omega\epsilon dE_z}{\beta'^2 r dr} - \frac{j\omega\epsilon r d^2E_z}{\beta'^2 r dr^2} - \frac{j\omega\epsilon d^2E_z}{\beta'^2 r^2 d\theta^2}$$

$$\frac{d^2E_z}{dr^2} + \frac{dE_z}{r dr} + \frac{d^2E_z}{r^2 d\theta^2} + \beta'^2 E_z = 0 \qquad (44).$$

Equation 44 is the wave equation for the electric field. The wave equation for the magnetic field is derived in the same manner, and it is given by (27:51):

$$\frac{d^2H_z}{dr^2} + \frac{dH_z}{r dr} + \frac{d^2H_z}{r^2 d\theta^2} + \beta'^2 H_z = 0 \qquad (45).$$

The wave equation in equations 44 and 45 can be solved using the method of separation of variables. That is, a solution for the electric field can be assumed to be of the form (27:51):

$$E_z = R_z(r)\Theta_z(\theta) = R\Theta \qquad (46).$$

To solve for each component, equation 46 is substituted into the wave equation (equation 44) which yields:

$$\frac{d^2(R\Theta)}{dr^2} + \frac{d(R\Theta)}{r dr} + \frac{d^2(R\Theta)}{r^2 d\theta^2} + \beta'^2 R\Theta = 0$$

$$\frac{\Theta d^2R}{dr^2} + \frac{\Theta dR}{r dr} + \frac{R d^2\Theta}{r^2 d\theta^2} + \beta'^2 = 0$$

$$\frac{d^2R}{R dr^2} + \frac{dR}{R r dr} + \frac{d^2\Theta}{\Theta d\theta^2} + \beta'^2 r^2 = 0 \qquad (47).$$

Equation 47 can be separated into two equations that are each a separate function of R and Θ. That is, the only way for the sum of the two functions to equal a constant, is for each individual function to be equal to a constant. Since equation 47 is equal to zero, the sum of these two constants must be zero. Therefore, the two constants are equal, but have different signs. By specifying these arbitrary constants as N^2 and $-N^2$, the two equations are given by:

$$\frac{r^2 d^2R}{R dr^2} + \frac{r dR}{R dr} + \beta'^2 r^2 = N^2 \qquad (48)$$

$$\frac{d^2\Theta}{\Theta d\theta^2} = -N^2 \qquad (49).$$

Equations 48 and 49 are rewritten as follows (27:51):

$$\frac{d^2R}{dr^2} + \frac{dR}{r dr} + R\left(\beta'^2 - \frac{N^2}{r^2}\right) = 0 \qquad (50)$$

$$\frac{d\Theta^2}{d\theta^2} + \Theta N^2 = 0 \qquad (51).$$

The closed form solution of equation 51 is given by (27:51):

$$\Theta_z(\theta) = \begin{cases} \cos(N\theta + \phi) \\ \sin(N\theta + \phi) \end{cases} \qquad (52)$$

where ϕ is an arbitrary phase constant (assumed to be zero for simplicity). Equation 50 is a specific form of Bessel's differential equation, and it has a solution given by (27:51):

$$R_z(r) = \begin{cases} AJ_N(\beta' r) + A'Y_N(\beta' r) \text{ when } \beta' \text{ is real} & (53) \\ CK_N(|\beta'|r) + C'I_N(|\beta'|r) \text{ when } \beta' \text{ is imaginary} & (54) \end{cases}$$

where:

N = the azimuthal mode number

A, A', C, C' = arbitrary constants

J_N, Y_N = Nth-order Bessel functions of the first and second kind, respectively

K_N, I_N = Nth-order modified Bessel functions of the first and second kind, respectively.

The Bessel functions are illustrated in Figures III.13 and III.14, and the modified Bessel function are shown in Figures III.15 and III.16.

Boundary Conditions. To determine the constants in the solution to the differential equations, the specific geometry of an optical fiber is now applied to the equations for R and Θ. As discussed earlier, an optical fiber is composed of two concentric circular layers of dielectric material. The inner core has a radius (a) and an index of refraction (n_1). The outer cladding has a radius (b) and an index of refraction (n_2). The corresponding boundary conditions for the electric and magnetic fields are (27:56):

$$E_z^{core} = E_z^{cladding} \tag{55}$$

$$E_\theta^{core} = E_\theta^{cladding} \tag{56}$$

$$\epsilon_1 E_r^{core} = \epsilon_2 E_r^{cladding} \tag{57}$$

$$H_z^{core} = H_z^{cladding} \tag{58}$$

$$H_\theta^{core} = H_\theta^{cladding} \tag{59}$$

$$H_r^{core} = H_r^{cladding} \tag{60}$$.

The boundary conditions also dictate that the azimuthal mode number, N, and the axial phase constant, β, must be consistent for the fields in both regions (27:53). Therefore, the solutions in the cladding and core regions will be examined separately, and then they will be reconciled at the core-cladding interface.

For the cladding region, the $R_z(r)$ solution must decay in an exponential fashion in order for light to propagate in the core. This requirement means that equation 53 cannot be a solution for

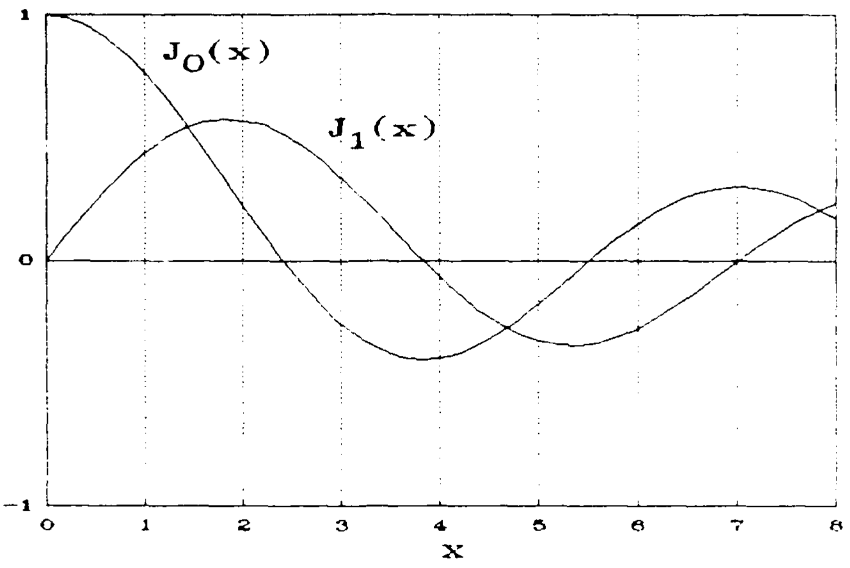

Figure III.13. Nth-Order Bessel Functions of the First Kind (28:390)

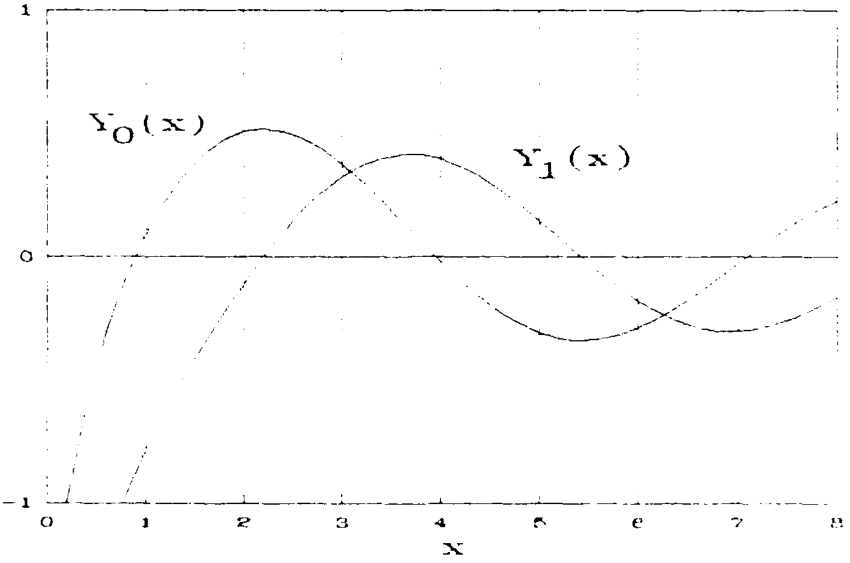

Figure III.14. Nth-Order Bessel Functions of the Second Kind (28:391)

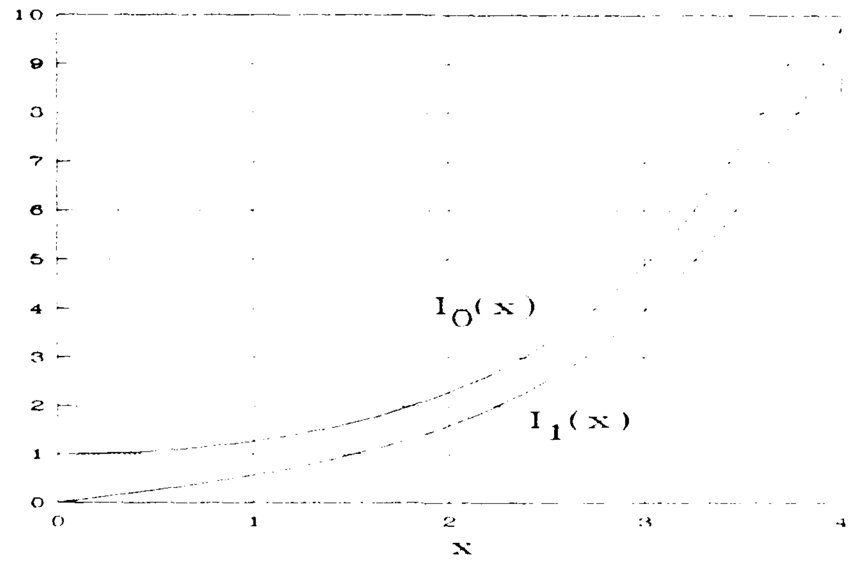

Figure III.15. Nth-Order Modified Bessel Functions of the First Kind (28:416)

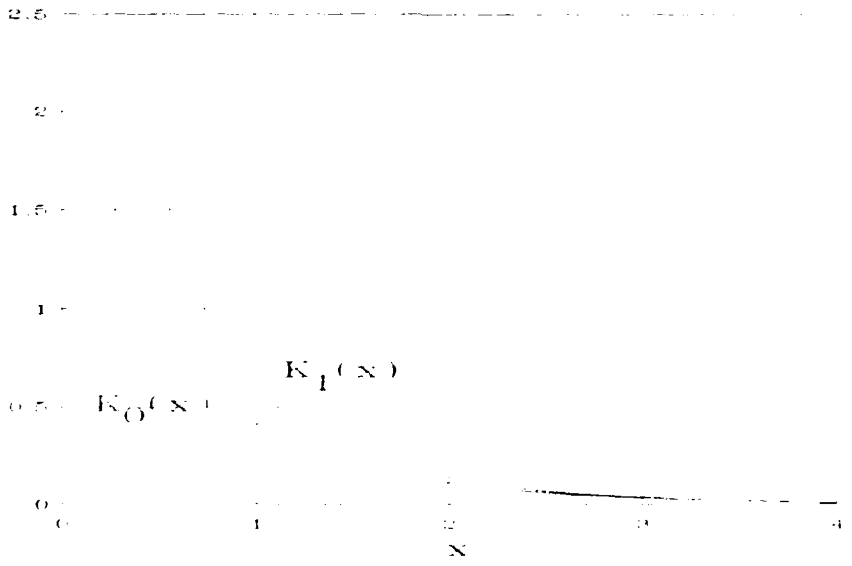

Figure III.16. Nth-Order Modified Bessel Functions of the Second Kind (28:417) the electric field in the cladding. Consequently, the constant C' in equation 54 must also be zero since I_n diverges for large values of r (27:53).

For the core region, the solution cannot contain Y_N or K_N, since these functions diverge on-axis when r equals zero. The requirement for the electric field to be smoothly connected at the interface prevents the solution from containing I_N. As shown in the graphical representations, I_N'/I_N (the ' refers to differentiation with respect to r) is always positive, and K_N'/K_N (the cladding solution function) is always negative (27:53).

Therefore, the solution in the core is proportional to J_N, and the solution in the cladding is proportional to K_N. The boundary conditions also indicate that β' must be real in the core and imaginary in the cladding. Therefore, based on the definition of β' (equation 39), β is bounded as follows (27:53):

$$kn_2 < \beta < kn_1.$$

The analysis for the magnetic field component follows the analysis outlined for the electric field. Based upon the previous arguments, the z-components of the electric and magnetic fields are expressed as (27:54):

$$E_z = AJ_N(ur/a)\sin(N\theta) \qquad (61)$$

$$H_z = BJ_N(ur/a)\cos(N\theta) \qquad (62)$$

in the core, and

$$E_z = CK_N(wr/a)\sin(N\theta) \qquad (63)$$

$$H_z = DK_N(wr/a)\cos(N\theta) \qquad (64)$$

in the cladding,

where

$$u = \beta'_1 a = (k^2 n_1^2 - \beta^2)^{1/2} a \qquad \text{(normalized transverse phase constant in the core)} \qquad (65)$$

$$w = |\beta'_2| a = (\beta^2 - k^2 n_2^2)^{1/2} a \qquad \text{(normalized transverse phase constant in the cladding)} \qquad (66).$$

The choice of the sine or cosine function in equations 61 through 64 was made to facilitate the hybrid mode solution. With E_z and H_z specified, the other components can be derived by substituting equations 61, 62, 63 and 64 into equations 40, 41, 42, and 43.

As an example, E_r in the core is derived as follows:

$$E_r = \frac{-j}{\beta'^2}\left[\frac{\omega\mu dH_z}{r d\theta} + \frac{\beta dE_z}{dr}\right] \qquad (40)$$

$$E_r = \frac{-j}{\beta'^2}\left[\frac{\omega\mu d}{r d\theta}\left(BJ_N(ur/a)\cos(N\theta)\right) + \frac{\beta d}{dr}\left(AJ_N(ur/a)\sin(N\theta)\right)\right]$$

$$E_r = \frac{-j}{\beta'^2}\left[\frac{\omega\mu BJ_N(ur/a)N\sin(N\theta)}{r} + \frac{\beta AuJ_N'(ur/a)\sin(N\theta)}{a}\right]$$

$$E_r = \left[\frac{-Aj\beta J_N'(ur/a)}{(u/a)} + \frac{Bj\omega\mu NJ_N(ur/a)}{(u/a)^2 r}\right]\cos(N\theta) \qquad (67).$$

The other components are given as (27:54-55):

$$E_\theta = \left[\frac{-Aj\beta NJ_N(ur/a)}{(u/a)^2 r} + \frac{Bj\omega\mu J_N'(ur/a)}{(u/a)}\right]\sin(N\theta) \qquad (68)$$

$$H_r = \left[\frac{Aj\omega\epsilon_1 NJ_N(ur/a)}{(u/a)^2 r} - \frac{Bj\beta J_N'(ur/a)}{(u/a)}\right]\cos(N\theta) \qquad (69)$$

$$H_\theta = \left[\frac{Aj\omega\epsilon_1 J_N'(ur/a)}{(u/a)} - \frac{Bj\beta NJ_N(ur/a)}{(u/a)^2 r}\right]\sin(N\theta) \qquad (70)$$

in the core, and

$$E_r = \left[\frac{Cj\beta K_N'(wr/a)}{(w/a)} - \frac{Dj\omega\mu NK_N(wr/a)}{(w/a)^2 r}\right]\sin(N\theta) \qquad (71)$$

$$E_\theta = \left[\frac{Cj\beta NK_N(wr/a)}{(w/a)^2 r} - \frac{Dj\omega\mu J_N'(wr/a)}{(w/a)}\right]\cos(N\theta) \qquad (72)$$

$$H_r = \left[\frac{-Cj\omega\epsilon_2 N K_N(wr/a)}{(w/a)^2 r} + \frac{Dj\beta K_N'(wr/a)}{(w/a)}\right]\cos(N\theta) \qquad (73)$$

$$H_\theta = \left[\frac{Cj\omega\epsilon_2 K_N'(wr/a)}{(w/a)} - \frac{Dj\beta N K_N'(wr/a)}{(w/a)^2 r}\right]\sin(N\theta) \qquad (74)$$

in the cladding.

A set of equations for the constants A, B, C, and D is obtained by setting r equal to "a" in the expressions for the electric and magnetic field components (equations 61 through 74), and substituting these equations into the boundary condition equations (equations 55 through 60).

As an example, starting with equation 55:

$$E_z^{core} = E_z^{cladding} \qquad (55).$$

Substituting equations 61 and 63 into equation 55 yields:

$$AJ_N(ur/a)\sin(N\theta) = CK_N(wr/a)\sin(N\theta).$$

Setting r=a in the above expression yields:

$$AJ_N(u) - CK_N(w) = 0 \qquad (75).$$

The same method produces the following equations (27:57):

$$BJ_N(u) - DK_N(w) = 0 \qquad (76)$$

$$\frac{Aj\beta NJ_N(u)}{(u/a)^2 a} - \frac{Bj\omega\mu J_N'(u)}{(u/a)} + \frac{Cj\beta NK_N(w)}{(w/a)^2 a} - \frac{Dj\omega\mu K_N'(w)}{(w/a)} = 0 \qquad (77)$$

$$\frac{Aj\omega\epsilon_1 J_N'(u)}{(u/a)} - \frac{Bj\beta NJ_N(u)}{(u/a)^2 a} + \frac{Cj\omega\epsilon_2 K_N'(w)}{(w/a)} - \frac{Dj\beta NK_N(w)}{(w/a)^2 a} = 0 \qquad (78).$$

A normalized set of values for the constants can be derived by setting A equal to one and using equations 75 through 78. From equation 75, C is found to be:

$$C = \frac{J_N(u)}{K_N(w)} \qquad (79).$$

From equation 76, D in terms of B is given by:

$$D = \frac{J_N(u)B}{K_N(w)} \qquad (80).$$

To solve for B, equations 79 and 80 are substituted into equation 77 to yield:

$$\frac{j\beta N J_N(u)}{(u/a)^2 a} - \frac{Bj\omega\mu J_N'(u)}{(u/a)} + \frac{J_N(u)Cj\beta N K_N(w)}{K_N(w)(w/a)^2 a} - \frac{BJ_N(u)j\omega\mu K_N'(w)}{K_N(w)(w/a)} = 0.$$

Solving for B gives:

$$B = \frac{\dfrac{\beta N}{\omega\mu}\left[\dfrac{1}{u^2} + \dfrac{1}{w^2}\right]}{\left[\dfrac{J_N'(u)}{uJ_N(u)} + \dfrac{K_N'(w)}{wK_N(w)}\right]} \qquad (81).$$

Correspondingly, substituting equation 81 into 80 yields D:

$$D = \frac{\dfrac{\beta N J_N(u)}{\omega\mu K_N(w)}\left[\dfrac{1}{u^2} + \dfrac{1}{w^2}\right]}{\left[\dfrac{J_N'(u)}{uJ_N(u)} + \dfrac{K_N'(w)}{K_N(w)w}\right]} \qquad (82).$$

Finally, all the components, including the normalized constants, are now specified for the electric and magnetic fields in the optical fiber.

Allowed Modes. The set of constant equations (equations 75 through 78) limit the modes that are will propagate in the fiber. Equations 75 through 78 can be written in a matrix form as (27:57):

$$[M] \times \begin{bmatrix} A \\ B \\ C \\ D \end{bmatrix} = 0,$$

where

$$M = \begin{bmatrix} J_N(u) & 0 & -K_N(w) & 0 \\ 0 & J_N(u) & 0 & -K_N(w) \\ \dfrac{j\beta N J_N(u)}{(u/a)^2 a} & \dfrac{-j\omega\mu J_N{}'(u)}{(u/a)} & \dfrac{j\beta N K_N(w)}{(w/a)^2 a} & \dfrac{-j\omega\mu K_N{}'(w)}{(w/a)} \\ \dfrac{j\omega\epsilon_1 J_N{}'(u)}{(u/a)} & \dfrac{-j\beta N J_N(u)}{(u/a)^2 a} & \dfrac{j\omega\epsilon_2 K_N{}'(w)}{(w/a)} & \dfrac{-j\beta N K_N(w)}{(w/a)^2 a} \end{bmatrix}.$$

For a solution to exist for the A, B, C, and D constants, the determinant of the matrix M must be zero. Evaluating the determinant produces the following equation (27:57):

$$\left[\frac{J_N{}'(u)}{uJ_N(u)} + \frac{K_N{}'(w)}{wK_N(w)}\right]\left[\frac{\epsilon_1 J_N{}'(u)}{\epsilon_2 u J_N(u)} + \frac{K_N{}'(w)}{wK_N(w)}\right] = N^2\left(\frac{1}{u^2} + \frac{1}{w^2}\right)\left(\frac{\epsilon_1}{\epsilon_2 u^2} + \frac{1}{w^2}\right) \qquad (83).$$

Equation 83 places restrictions on the allowed modes. These restrictions are examined by the various mode classifications. That is, the boundary conditions at the *core-cladding* interface dictate that TM (transverse magnetic) and TE (transverse electric) modes can only exist when N equals zero in the expressions for the electric and magnetic fields in the core and cladding (equations 61 through 74) (27:54). When N is not zero, the boundary conditions can be satisfied by a linear combination of TM and TE modes which are labeled HE and EH modes (hybrid modes). TM modes occur when H_z and N are zero, which from equations 62 and 64, requires that the constants B and D are zero.

For TM modes, equation 83 is simplified to:

$$\frac{\epsilon_1 J_0{}'(u)}{\epsilon_2 u J_0(u)} + \frac{K_0{}'(w)}{wK_0(w)} = 0 \qquad (84).$$

For TE modes, E_z and N are zero which requires that the constants A and C in equations 61 and 63 are zero. Consequently, equation 83 for TE modes can be simplified to:

$$\frac{J_0'(u)}{uJ_0(u)} + \frac{K_0'(w)}{wK_0(w)} = 0 \qquad (85).$$

To simplify equation 83 for the hybrid modes, it is necessary to invoke the weakly-guided approximation, which assumes that ϵ_1 is approximately equal to ϵ_2. With this approximation, equation 64 for the hybrid modes can be simplified to:

$$\frac{J_N'(u)}{uJ_N(u)} + \frac{K_N'(w)}{wK_N(w)} = \pm N^2\left(\frac{1}{u^2} + \frac{1}{w^2}\right) \qquad (86).$$

Using the weakly-guided approximation for the TM modes simplifies equation 84 into equation 85. Equation 85 can be simplified further using the following identities (27:59):

$$J_0'(u) = -J_1(u)$$

$$K_0'(w) = -K_1(w)$$

$$v^2 = u^2 + w^2 = k^2 n_1^2 a^2 2\Delta \text{ (normalized frequency squared)} \qquad (87)$$

$$\Delta = \frac{n_1^2 - n_2^2}{2n_1^2} \qquad (88).$$

Equation 85 is now of the form:

$$-\frac{J_1(u)}{uJ_0(u)} = \frac{K_1((v^2-u^2)^{1/2})}{(v^2-u^2)^{1/2} K_0((v^2-u^2)^{1/2})} \qquad (89).$$

Equation 89 can be solved graphically to illustrate the allowed TM or TE modes. The v-parameter is a number which can be calculated for a particular fiber optic cable and excitation source wavelength. For example, if v is set equal to seven, Figure III.17 yields a graphical solution when N equals zero. In

Figure III.17, the right-hand side of equation 89 (Γ_1) is an exponentially growing function, and the tangent-like function is the left-hand side of equation 89 (X_1). The intersections of the two functions satisfy equation 87 for the corresponding value of u. For a particular solution set of u and v, a propagation constant β for the allowed mode can be calculated. To generate similar graphical solutions for the hybrid modes, equation 88 is simplified using the following identities (27:267):

$$\frac{J_N'(u)}{uJ_N(u)} = \frac{J_{N-1}}{uJ_N} - \frac{N}{u^2} = -\frac{J_{N+1}}{uJ_N} + \frac{N}{u^2} \qquad (90)$$

$$\frac{K_N'(w)}{wK_N(w)} = -\frac{K_{N-1}}{wK_N} - \frac{K}{w^2} = -\frac{K_{N+1}}{wK_N} + \frac{N}{w^2} \qquad (91).$$

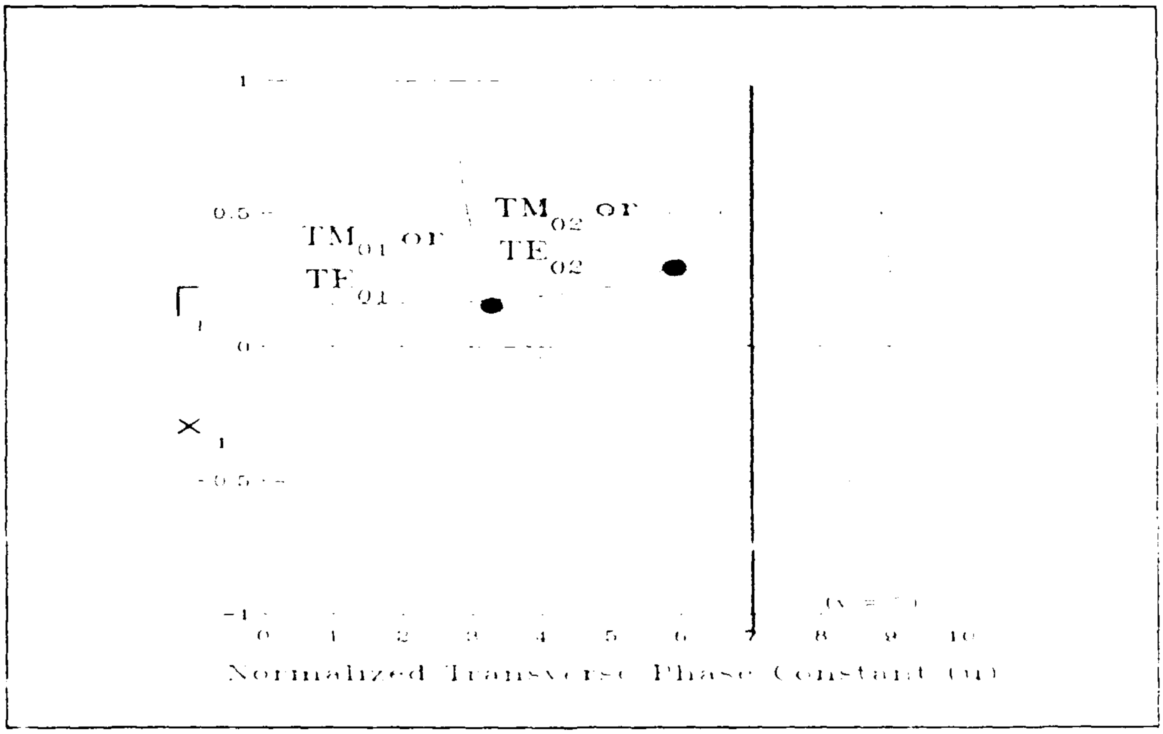

Figure III.17. Allowed TM or TE Modes

Equation 90 and 91 are substituted into equation 86 to yield two equations due to the positive and negative signs in equation 86; that is:

$$-\frac{J_{N+1}(u)}{uJ_N(u)} = \frac{K_{N+1}((v^2-u^2)^{1/2})}{(v^2-u^2)^{1/2}K_N((v^2-u^2)^{1/2})} \qquad (92)$$

and

$$\frac{J_{N-1}(u)}{uJ_N(u)} = \frac{K_{N-1}((v^2-u^2)^{1/2})}{(v^2-u^2)^{1/2}K_N((v^2-u^2)^{1/2}} \qquad (93).$$

Equation 92 describes the allowed EH modes, and equation 93 describes the allowed HE modes. Graphical solutions to equations 92 and 93 for N equal to one are shown in Figures III.18 and III.19. The axis labels for Figures III.18 and III.19 are as follows: Γ_2 refers to the left-hand side of equation 92, X_2 refers to the right-hand side of equation 92, Γ_3 refers to the left-hand side of equation 93, and X_3 refers to the right-hand side of equation 93.

Observations. As seen in Figures III.17 and III.18, there are values of the normalized frequency for which there are no allowed TE, TM, or EH modes. However, as shown in Figure III.19, there is always an allowed HE mode. Only the HE_{11} mode will propagate as long as the normalized frequency is sufficiently small to prevent any allowed TM_{00} or TE_{00} modes from propagating. From equation 89, this critical value of the normalized frequency occurs at the first zero of J_0, which occurs at a value of 2.405. Correspondingly, this value of the normalized frequency

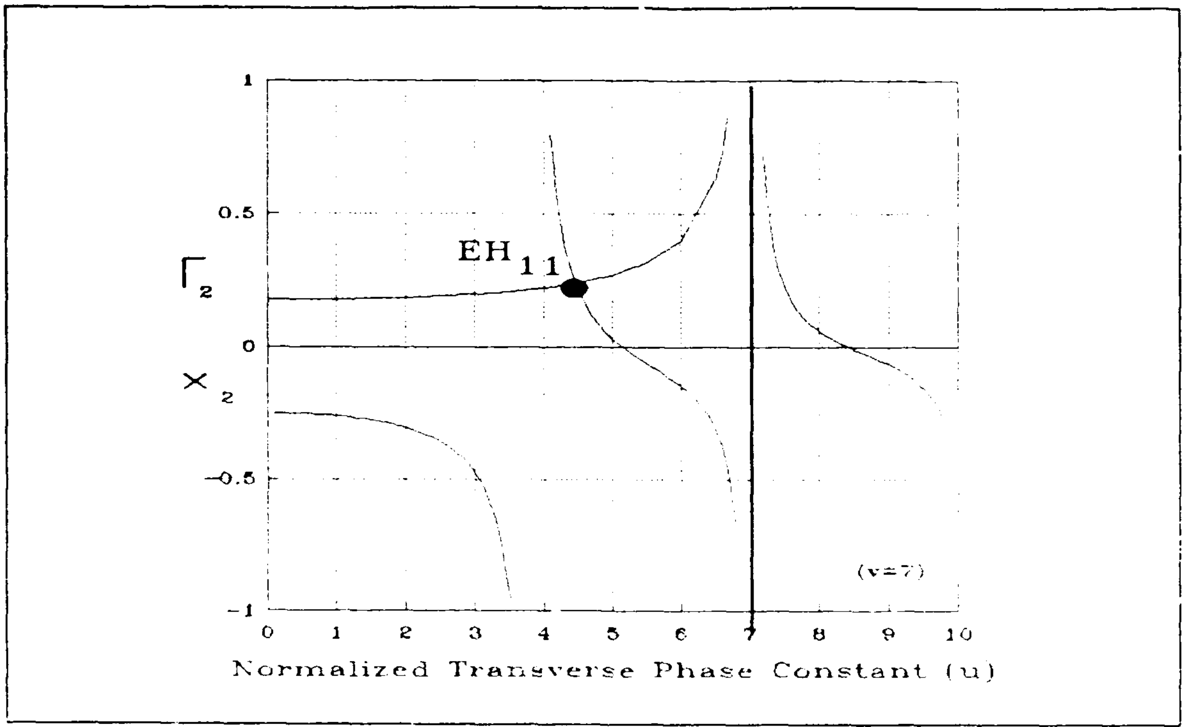

Figure III.18. Allowed EH Modes

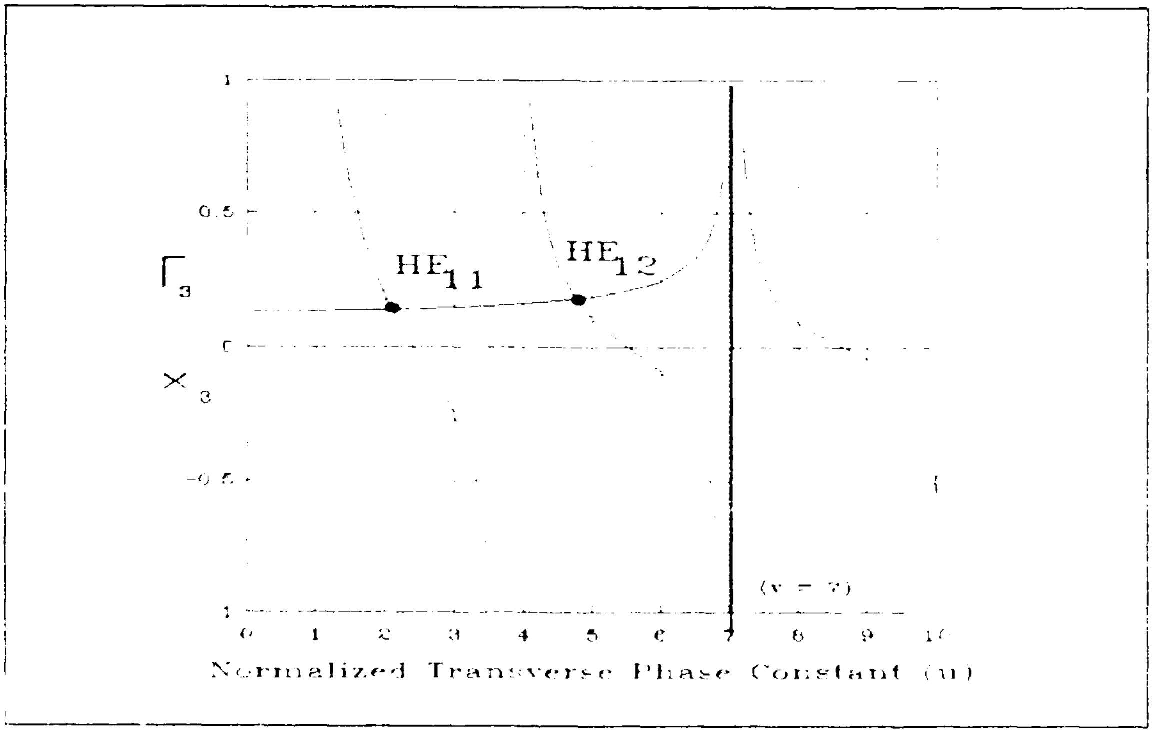

Figure III.19. Allowed HE Modes

constrains the values of the fiber's core radius (a), core index of refraction (n_1), cladding index of refraction (n_2), and excitation wavelength (λ). More explicitly, equation 89 is expanded to show the relationships between these parameters. That is:

$$v = kn_1 a 2^{1/2} \Delta^{1/2} = \frac{2^{3/2} \pi n_1 a \Delta^{1/2}}{\lambda} < 2.405 \qquad (94)$$

Assuming that the index of refraction difference between the core and inner cladding and the value of the fiber core's index of refraction are limited by manufacturing considerations, the two parameters of interest are the core size and excitation wavelength. The core size should be maximized to facilitate the source-to-fiber coupling. Therefore, the excitation wavelength should also be maximized. However, there is an upper limit on the excitation wavelength in the near infrared spectrum due to absorption in the fiber itself (26:87). In addition, there are further considerations concerning the choice of the optical source's wavelength that are discussed in the next section.

Specific Calculation. The electric and magnetic fields propagating in an optical fiber are now calculated for the particular optical source and fiber that was used in this research effort. After the phase constants are calculated, the A, B, C, and D constants are determined. The final step is to calculate and plot the electric and magnetic fields.

The normalized frequency (v) is calculated to be 1.87 (unitless) using equation 87 and the fiber optic cable dimensions for the York Technology, Model SM600, fiber that was described in the previous section. To determine the normalized transverse phase constant in the core (u), a BASIC computer program was written (included in Appendix C) to solve equation 89. Equation 89 was also solved graphically as shown in Figure III.20. As a result, u was found to be 1.48 (unit-less). The axial phase constant (β) was next evaluated to be 1.448 x 10^7 m^{-1} from equation 65.

Additionally, the u, v, and β constants were evaluated in another BASIC computer program (included in Appendix C) which also solved for the A, B, C, and D constants. This computer program used numerical series approximations for the Bessel functions and modified Bessel functions. The constants A, B, C,

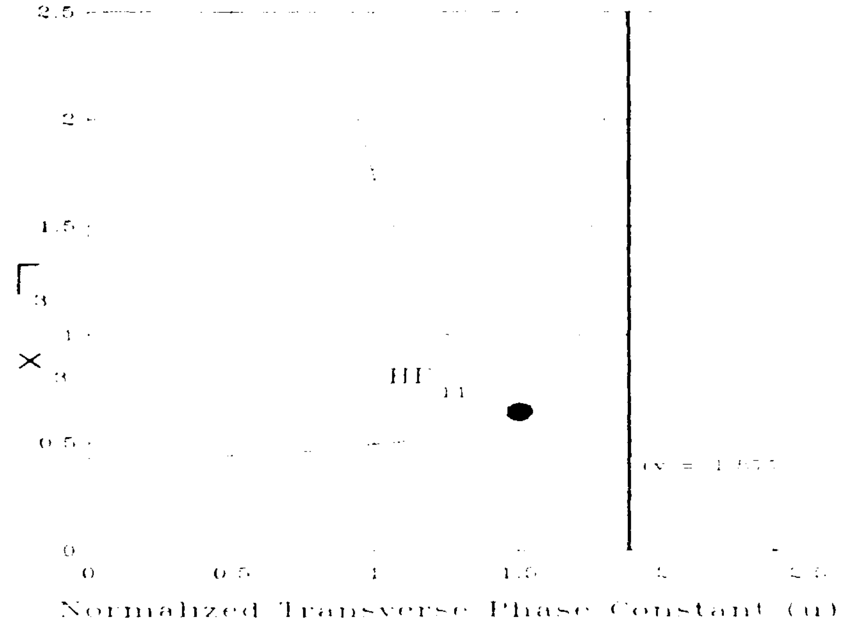

Figure III.20. Single-mode Operation of York Technology, Model SM600, Optical Fiber With a 0.633 um Laser Source and D were found to be 1, -3.832×10^{-3}, 1.178, and -4.509×10^{-3} (unit-less), respectively. The same computer program then solved for the electric and magnetic fields in the fiber. The electric field was found to be linearly polarized in the negative y-direction, and the magnetic field was linearly polarized in the positive x-direction. The components of electric and magnetic fields in the z-direction were found to be negligible in magnitude compared to the components in the x-y plane. Figures III.21 and III.22 illustrate the electric and magnetic fields propagating in the fiber optic cable. The electric and magnetic fields have decayed significantly after only a short distance into the cladding, which extends to over 35 times the radius of the core.

To summarize, solving for the electric and magnetic fields that propagated in the particular fiber optic cable used in this research project contributed information concerning the sensor's design. That is, there is a trade-off concerning fiber core radius and optical source wavelength, with maximum wavelength and minimum core radius desireable for single-mode operation, with a maximum core radius preferred for source-to-fiber coupling. The analysis also showed that thinning the cladding would not significantly affect the propagation of the electromagnetic wave since the wave has decayed after a short distance into the cladding.

Interferometer Operation

Additional information concerning the sensor's design can be

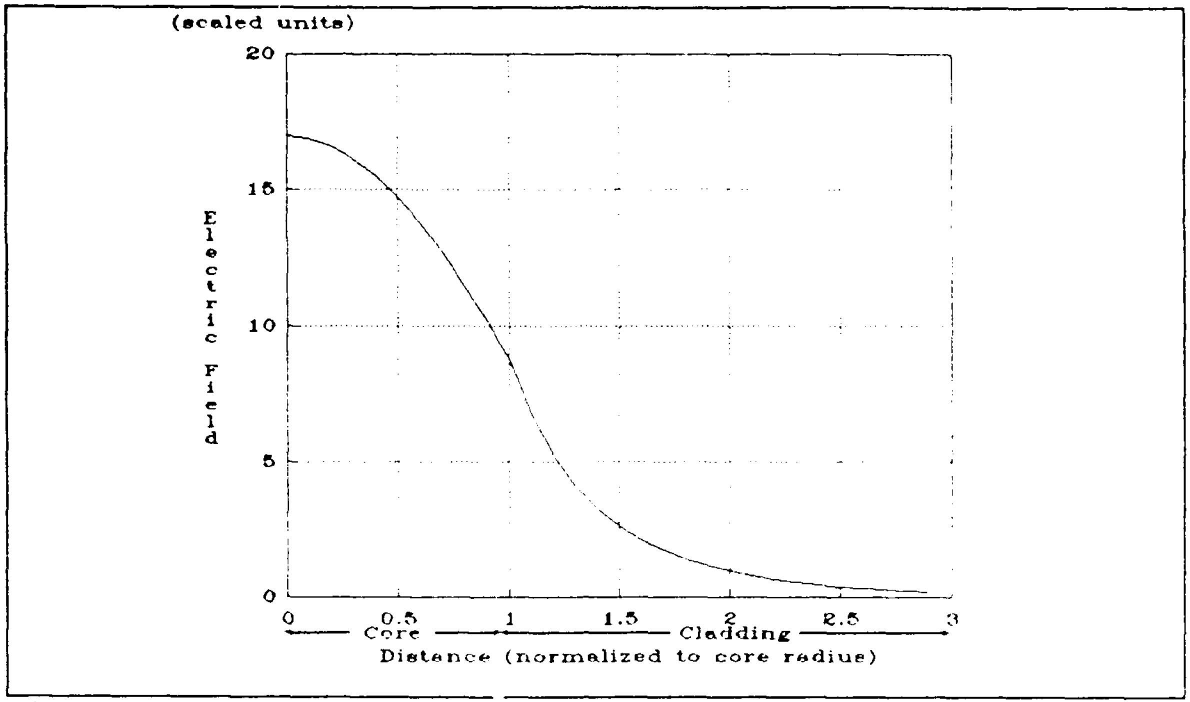

Figure III.21. Electric Field Propagating in York Technology, Model SM600, Optical Fiber with a 0.633 um Laser Source

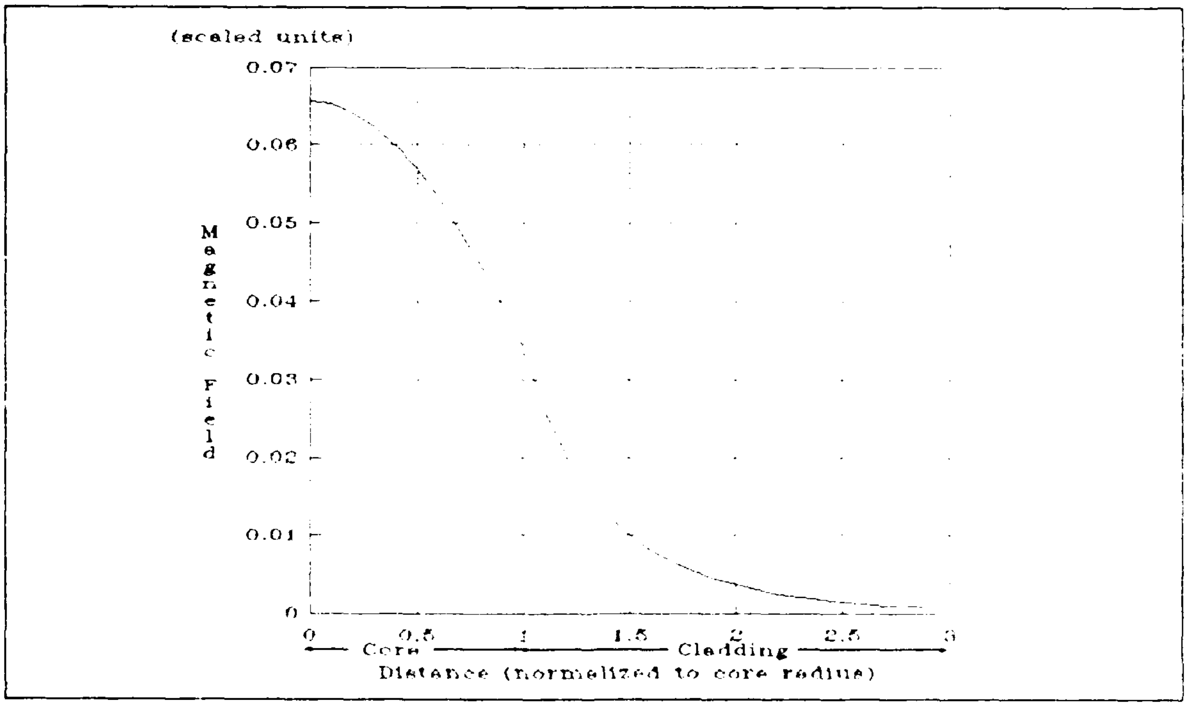

Figure III.22. Magnetic Field Propagating in York Technology, Model SM600, Optical Fiber with a 0.633 um Laser Source gained by examining the behavior of interferometers. A fiber optic implementation of the Mach-Zehnder (MZ) interferometer can be used to measure small changes in a fiber's length, such as those induced by a magnetostrictive material coating. This section explains how the small change in length in one arm of a MZ interferometer can be measured as a corresponding change in the phase of light propagating in that arm. This phase change is then converted into a detectable amplitude change. The components of a MZ interferometer are illustrated in Figure I.1. The section concludes with a discussion of the significant factors affecting magnetostrictive interferometer performance.

As shown in the previous analysis, the only mode propagating in single-mode fiber optic cables is the HE_{11} mode, which is linearly polarized. Using an equivalent form of equation 27, the electric field in the reference and sensor arms can be modeled as (29:277):

$$\mathbf{E}_r(z,t) = \mathbf{E}_{ro}\cos(\beta_r z - \omega t + \xi_r) \qquad (95)$$

$$\mathbf{E}_s(z,t) = \mathbf{E}_{so}\cos(\beta_s z - \omega t + \xi_s), \qquad (96)$$

where $\mathbf{E}_r(z,t$ = electric field in the reference arm

$\mathbf{E}_s(z,t)$ = electric field in the sensor arm

$\mathbf{E}_{ro}$ = reference arm electric field vector at time t, and position z

$\mathbf{E}_{so}$ = sensor arm electric field vector at time t, and position z

β = axial phase constant

ξ_r = initial phase constant in the reference arm

ξ_s = initial phase constant in the sensor arm.

For simplicity, the electric field is assumed to be equal in magnitude and parallel in each arm, with equal initial phase constants. While the initial phase constants may not be equal due to the fact that the sensor arm and reference arm are not exactly the same length, this assumption merely adds a constant in the final expression. The assumption that the electric fields are equal in magnitude is valid since the optical power in each arm of the sensor can be adjusted until they are equal. If the electric fields in each arm were not parallel, but constantly at an angle with respect to each other, this assumption would again only add another constant to the final result. However, if the orientation of the two electric fields varied with time, then the final result would be modulated by a time-varying factor. Since the behavior of the electric fields in a fused coupler has not been modeled, it will be assumed that the fields are constant with respect to each other. The mathematical representation of these assumptions is stated as:

$$\mathbf{E}_{ro} = \mathbf{E}_{so} = \mathbf{E}_c \qquad (97)$$

$$\xi_r = \xi_s = \xi \qquad (98).$$

Due to the high frequencies of optical signals ($\sim 10^{14}$ Hz), light detectors do not detect electric fields (29:45). Instead, optical detectors sense irradiance which is given by (29:277):

$$I = \epsilon v \langle E^2 \rangle \qquad (99)$$

where I = irradiance (W/cm^2)

ϵ = permittivity of the propagation media

v = speed of the propagating optical energy

$\mathbf{E}^2 = \langle|\mathbf{E}^2|\rangle = \langle|\mathbf{E}\cdot\mathbf{E}|\rangle$ = time-average value of the magnitude of the square of the electric field.

The time average of a function f(t) is given by (29:58):

$$\langle f(t)\rangle = \frac{1}{T}\int_{t}^{t+T} f(t')dt'$$

where T = time interval

t' = dummy integration variable.

The high frequency of the electromagnetic wave compared to the frequency response of light detectors indicates that the time interval (T) is much greater than the period of the electromagnetic wave. The square of the electric field for this application is given by:

$$E^2 = (\mathbf{E}_r + \mathbf{E}_s) \cdot (\mathbf{E}_r + \mathbf{E}_s) \qquad (100)$$

$$E^2 = |\mathbf{E}_r|^2 + |\mathbf{E}_s|^2 + 2|\mathbf{E}_r\cdot\mathbf{E}_s| \qquad (101).$$

Multiplying by the appropriate constants and taking the time-averaged value of the above expression yields:

$$I = I_r + I_s + I_{rs} \qquad (102).$$

The last term, I_{rs}, is the interference term which is evaluated by substituting equations 95 and 96 into equation 99 as follows:

$$I_{rs} = 2\epsilon v\langle|\mathbf{E}_r\cdot\mathbf{E}_s|\rangle$$

$$I_{rs} = 2\epsilon v\langle|\mathbf{E}_o\cdot\mathbf{E}_o \cos(\beta_r z-\omega t+\xi)\cos(\beta_s z-\omega t+\xi|\rangle$$

$$I_{rs} = 2\epsilon v\langle|\mathbf{E}_o\cdot\mathbf{E}_o [\cos(\beta_r z+\xi)\cos\omega t + \sin(\beta_r z+\xi)\sin\omega t] \times$$

$$[\cos(\beta_s z+\xi)\cos\omega t + \sin(\beta_s z+\xi)\sin\omega t]|\rangle$$

$$\begin{aligned} I_{rs} = 2\epsilon v\langle|\mathbf{E}_o\cdot\mathbf{E}_o\ \{&\cos^2\omega t\cos(\beta_r z+\xi)\cos(\beta_s z+\xi)\ + \\ &\sin^2\omega t\sin(\beta_r z+\xi)\sin(\beta_s z+\xi)\ + \\ &\cos\omega t\sin\omega t\ \mathrm{x}\ [\cos(\beta_r z+\xi)\sin(\beta_s z+\xi)\ + \\ &\sin(\beta_r z+\xi)\cos(\beta_s z+\xi)]\}|\rangle \end{aligned} \qquad (102).$$

Using the fact that (29:278):

$$\langle\sin^2\omega t\rangle = \langle\cos^2\omega t\rangle = \tfrac{1}{2}$$

and $\langle\cos\omega t\sin\omega t\rangle = 0$,

the interference term (equation 102) can be rewritten as:

$$\begin{aligned} I_{rs} = 2\epsilon v\langle|\mathbf{E}_o\cdot\mathbf{E}_o\ [&\tfrac{1}{2}\cos(\beta_r z+\xi)\cos(\beta_s z+\xi)\ + \\ &\tfrac{1}{2}\sin(\beta_r z+\xi)\sin(\beta_s z+\xi)]|\rangle \end{aligned} \qquad (103).$$

Equation 103 can be further simplified using the trigonometry identity:

$$\cos(a)\cos(b) + \sin(a)\sin(b) = \cos(a-b),$$

which, when used in equation 103 yields:

$$I_{rs} = \epsilon v\langle|\mathbf{E}_o\cdot\mathbf{E}_o\ \cos(\beta_r z-\beta_r z)|\rangle \qquad (104).$$

Equation 104 is no longer a function of time, and the time-averaged value is simply:

$$I_{rs} = \epsilon v[E_o^2\ \cos(\beta_r z-\beta_r z)]$$

$$I_{rs} = 2I_o\ \cos\delta \qquad (105)$$

where δ = phase difference or the difference in the optical path length.

The non-interference terms in the irradiance expression are correspondingly evaluated as (29:278):

$$I_r = I_s = I_o = \tfrac{1}{2}E_o^2.$$

Finally, the total irradiance can now be expressed as:

$$I = I_r + I_s + I_{rs}$$

$$I = I_o + I_o + 2I_o\cos\delta$$

$$I = 2I_o(1 + \cos\delta)$$

$$I = 4I_o\cos^2(\tfrac{1}{2}\delta) \qquad (106).$$

The total irradiance function is plotted with respect to the phase difference (δ) in Figure III.23. This Figure shows how phase changes are converted into detectable amplitude variations.

Now that the effect of changing the phase difference has been illustrated, the exact effect of strain on the optical

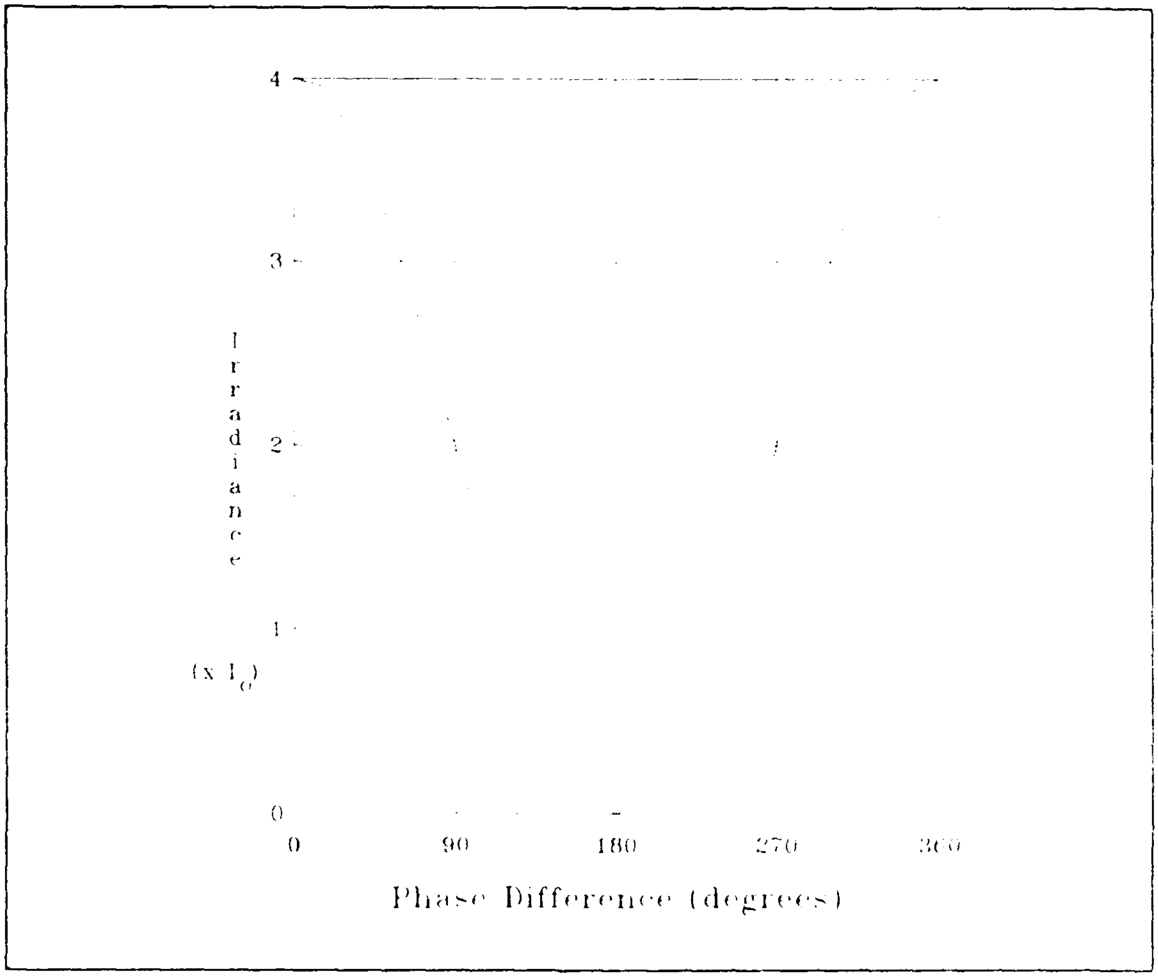

Figure III.23. Total Irradiance Function Plotted with Respect to the Phase Difference fiber is examined. In the section on optical fibers, equation 17 described optical fibers as a bulk piece of material which undergoes a longitudinal change in length in response to a specifically applied force. To examine this characterization more closely, the actual phase difference in an optical fiber exposed to an external force is explored.

The difference in path lengths in the sensor and reference arms is the phase difference (δ), which is given by:

$$\delta = \beta_r z - \beta_s z = \beta l \qquad (107).$$

A phase shift occurs when the phase difference changes; that is:

$$\Delta\delta = \Delta(\beta l) \qquad (108).$$

When the fiber length changes, the change in the phase difference is due to both the length change and an induced change in the index of refraction of the glass fiber. This phase difference change is given by (3:88):

$$\Delta\delta = \frac{2\pi L}{\lambda}\left(\frac{\Delta L}{L} + \frac{\Delta n}{n}\right) \qquad (109)$$

$$\Delta\delta = \frac{2\pi n L}{\lambda}\{\gamma_3 - \tfrac{1}{2}n^2[(p_{11} + p_{12})\gamma_1 + p_{12}\gamma_3]\}, \qquad (110)$$

where n = index of refraction of the core = 1.461

L = initial length of the sensor arm

λ = wavelength of the excitation source

γ_1 = change in length in the radial direction = $-\nu\gamma_3$

γ_3 = change in length along the optical axis

p_{11} = photoelastic tensor element

p_{12} = photoelastic tensor element.

The constants p_{11} and p_{12} are 0.12 and 0.27, respectively, for optical fibers in general. Substituting the numerical values into the above expression yields:

$$\Delta\delta = \frac{2\pi nL}{\lambda}(\gamma_3 - 0.08\gamma_3), \tag{111}$$

which shows that the major contribution to phase difference arises from a change in the fiber's length. Therefore, it is a valid approximation to only attribute phase change difference to a change in length along the optical axis of the fiber.

Other factors may also affect a change in the phase difference for a magnetostrictive fiber optic interferometer. Temperature variations can affect the fiber optic sensor in two ways: (i) linear expansion of the magnetostrictive material and, (ii) index of refraction changes (30:1478). Figure III.24 depicts how calculated thermal variations may cancel the effects of magnetostriction in nickel. In this research project, thermal variations were minimized by thermally insulating the optical fibers with cloth, and placing the sensor and reference arms in close proximity so that any thermal effects would occur in both arms to produce a minimal effect on the sensor's response.

The thickness of the ferromagnetic material also affects the phase difference change. Figure III.25 shows experimental data relating phase difference change for different thicknesses of a nickel jacket. In this research project, the magnetostrictive coatings were designed to be at least fifteen microns thick to avoid compromising the phase change difference.

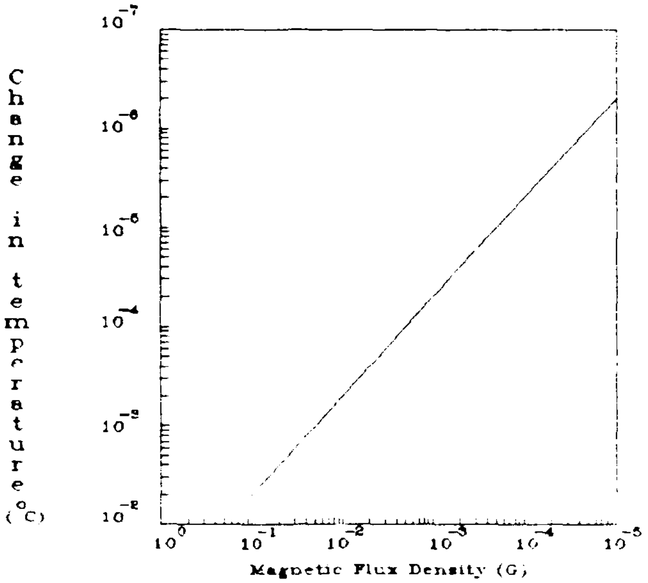

Figure III.24. Thermal Fluctuations Producing a Phase Change Identical to a Magnetostriction Phase Change (31:3719)

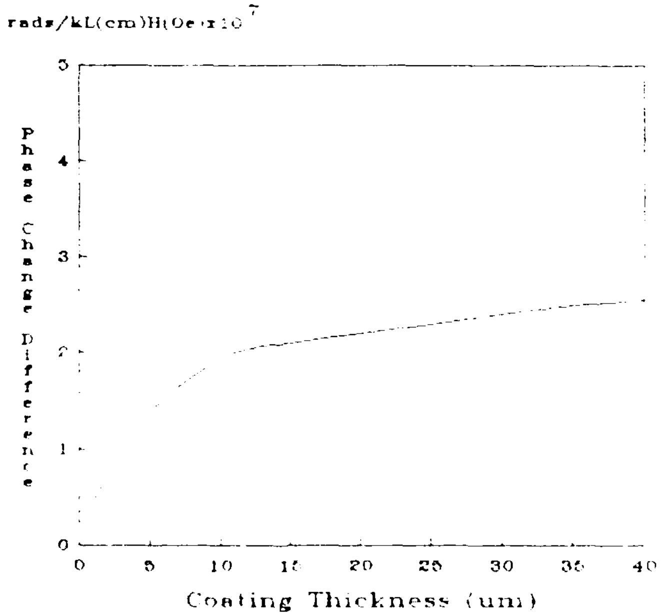

Figure III.25. Effect of Magnetostrictive Coating Thickness on the Phase Change Difference (32:3747)

Critical Performance Parameters

In summary, the results of this Chapter's analysis revealed the critical parameters affecting the sensitivity of a MZ fiber optic magnetic field sensor. These parameters are shown in Table III.2.

The magnetostrictive material used in the sensor design incorporates the most significant influence on the sensor's performance. The material's magnetostriction properties directly affect the magnitude of the change in the length of the sensor arm. The amount of magnetostriction depends on the initial orientation of the magnetic domains. Maximum magnetostriction occurs when the magnetic domains are initially aligned perpendicular to the direction of the magnetic field to be

Table III.2. Critical Parameters Affecting Sensor Performance

- Magnetostrictive Material
- Initial Orientation of the Magnetic Domains
- Magnetostrictive Material Thickness
- Magnetostrictive Material Length
- Shape of the Magnetostrictive Material Coating
- Fiber Optic Cable's Cladding Thickness
- Wavelength of the Optical Excitation Source
- Sensor Temperature Stability

measured.

In addition to processing the material, the geometry of the magnetostrictive coating affects the sensor's response. There is experimental evidence in the literature that the thickness of the magnetostrictive material affects the amount of magnetostriction. The amount of induced phase change increases with increasing coating thickness until saturating at a coating thickness associated with bulk material. The static physical length of the magnetostrictive material is directly proportional to the phase change difference as shown in equation 111. In a packaged sensor, the length of the coating could be maximized by winding the sensor arm in a coil. For this research project, the length is limited to 10 cm. While not addressed in the literature, it is postulated that the shape of the magnetostrictive material may affect its magnetostriction.

The geometry of the fiber optic cable directly affects the amount that the cable will stretch under the force applied by the magnetostrictive material. To maximize the change in length, the cross-sectional area of the fiber optic cable should be minimized. The cross-sectional area can be minimized by reducing the fiber optic cable's cladding thickness.

The wavelength of the optical excitation source also affects the sensor's performance. The phase change difference is inversely proportional to the wavelength. Therefore, a short wavelength excitation source is desired. However, the shorter the wavelength, the smaller the fiber optic core must be for single-mode operation. The smaller core leads to fiber optic cable fabrication problems and difficulties in coupling light into the fiber.

Finally, the ambient temperature environment surrounding the sensor will also affect its performance. Thermal fluctuations cause thermal expansion and changes in the index of refraction of the optical fiber. These thermally induced changes in the sensor arm may be sufficiently large so as to mask any magnetostrictive induced changes. For this project, thermal fluctuations were minimized by covering the fibers with cloth and placing the sensor and reference arms in close proximity.

Sensor Arm Designs

Based on the preceding theory, specific sensor arms were designed to test specific aspects of the fiber optic magnetic field sensor. These sensor arms were intended to evaluate the following sensor parameters:

1) magnetostrictive material
2) bulk material vs. thin films
3) initial orientation of magnetic domains
4) magnetostrictive material coating geometry
5) fiber optic cable cladding thickness

A series of experiments were carefully planned to evaluate each of these sensor parameters.

Experiment 1. The first experiment was designed to evaluate the most promising magnetostrictive material. To accomplish this objective, three sensor arms were designed to be 10 cm in length with a 15 um thick uniform coating of a particular magnetostrictive material (cobalt, iron, and nickel).

Experiment 2. The second experiment was designed to compare the sensor's performance relative to thin film coated fibers and fibers bonded to bulk material. To accomplish this objective, the sensor arms were designed to be three identical 10 cm long bulk rods of the magnetostrictive materials bonded to optical fibers.

Experiment 3. The third experiment was designed to evaluate the effect of initially orienting the magnetic domains. To accomplish this objective, the sensor arms from the first experiment were planned to be heated above their Curie temperature, and then allowed to cool in the presence of an externally applied static magnetic field flux density of 1000 G.

Experiment 4. The fourth experiment investigated the effect of coating geometry on the sensor's performance. Using the most promising material from the first experiment, an ensemble of sensor arms were designed. The length of the magnetostrictive material was limited to 10 cm, and its thickness was controlled to 15 um. The sensor's response with the uniformally coated sensor arm of the first experiment was planned to be compared to the sensor's performance with fibers coated with the following geometries: (i) semi-cylindrical coating, and (ii) spiral coatings with void spacings of 1 mm, 5 mm, and 10 mm.

Experiment 5. This experiment was designed to determine the effects of fiber optic cable cladding thickness on sensor performance. The magnetostrictive coating on each fiber in this experiment was designed to be carefully controlled (10 cm length and 15 um thickness). Prior to RF sputtering the magnetostrictive material on the fiber, the cladding on four fiber were designed to be thinned to diameters of 125, 100, 75, and 50 um. These diameters correspond to normalized areas of 100%, 64%, 36%, and 16% with respect to the 125 um diameter fiber.

IV. Experimental Procedure

This Chapter describes the equipment configuration and experimental procedures that were used to evaluate the sensor. This Chapter describes the Helmholtz coil calibration procedure, sensor arm fabrication, interferometer arrangement, sensor sensitivity measurements, and sensor optimization. The results of these procedures are reported in the following chapter.

Helmholtz Coil Calibration

In order to verify that the Helmholtz coil generated the magnetic field flux density which was predicted by its theoretical analysis, the Helmholtz coil was calibrated using a commercial Hall effect magnetometer. The magnetometer available at AFIT (Walker Scientific, Model MG-7D, Worcester, MA) was not sufficiently sensitive, so a more responsive magnetometer (F. W. Bell Inc., model 620, Columbus, OH) was borrowed from Tim Peterson of the Materials Laboratory to perform the calibration. After the ambient magnetic field noise was measured, the magnetic field flux density produced by the Helmholtz coil was characterized.

Since the sensor's sensitivity goal was to detect magnetic flux densities below the earth's ambient magnetic field of approximately 0.1 G (2:360), a magnetically shielded test chamber was constructed. A set of hollow spheres fabricated from a material with high permeability would represent an ideal magnetically shielded chamber (17:9). However, due to practical considerations, a first level magnetically shielded chamber was constructed. The AFIT model shop built a plexiglass rectangular chamber which measured 31 cm x 51 cm x 31 cm. This size permitted the Helmholtz coils to be placed inside the chamber. The enclosure had two 2.5 cm diameter holes as ports for the optical fibers and a 25 pin connector for electrical connections to the Helmholtz coil. The surfaces of the plexiglass were sprayed with a nickel-impregnated polymer coating (Miller-Stephenson Chemical Co., model MS-485N, Danbury, CT). However, the conducting paint supply was exhausted before an even coat could be applied to the chamber. As a result, the conductivity of the surfaces varied; for example, the resistance across the chamber's lid was measured to be seven ohms. To further lower the chamber surfaces' resistance, aluminum foil was placed on both sides of each surface. This foil was electrically connected to the ground terminal on the Helmholtz coil. The resistance between any surface on the enclosure and the Helmholtz ground connection was measured to be one ohm or less on the average.

Before attempting to make any measurements, the magnetometer was calibrated for DC magnetic fields. AC calibration was not attempted since reference AC magnetic field sources were not available. The magnetometer readings were taken when the probe was placed inside a zero gauss chamber and two reference magnets of 95 and 978 G, respectively. Reference magnets with smaller magnetic flux densities would have been more appropriate, but were not available.

To determine the ambient magnetic field flux density, the magnetometer probe was placed in various positions and orientations, both inside the chamber and around the laboratory. The magnetometer's readings were then recorded with no current flowing in the Helmholtz coil.

After the ambient magnetic field flux density was determined, power was applied to the Helmholtz coil. For the DC measurements, the current was supplied with a power supply (Hewlett-Packard, model HP 6236B, Palo Alto, CA) and for the AC measurements, the current was provided with a function generator (Wavetek, model 23, San Diego, CA) and a power amplifier (Hewlett-Packard, model HP 467A, Palo Alto, CA). The power amplifier was used when currents between 120 and 500 mA were required. (Larry Reitz of the Electronic Technology Laboratory provided the power amplifier). The frequency of the AC signal was chosen to be 25 Hz since this frequency is in the 0 to 30 Hz range of interest, and was not an AC power harmonic. During measurements, the current was monitored with a multimeter (Fluke, model 8010A, Everett, WA).

Once power was applied to the Helmholtz coil, DC and AC measurements were made. The first measurement was accomplished to determine the magnetic field flux density at the center point between the two coils for different amounts of applied current. For the second set of measurements, a constant current of 250 mA was applied to the Helmholtz coil. The magnetic field flux density at the center point between the two coils was then determined for different numbers of turns in the coils. The final measurement was implemented to evaluate the magnetic field flux density at various spatial locations between the two coils for a constant applied current and fixed number of turns. The spatial variations of the magnetic field flux density was determined by placing the 2 mm x 5 mm x 0.5 mm probe tip in various positions on and off the axis between the coils.

Sensor Arm Fabrication

After the model biomagnetic field source was generated and characterized, the sensor arms were fabricated. The two classes of sensor arms used in this research project included: (i) fibers that were coated with thin films of magnetostrictive material, and (ii) fibers that were attached to bulk magnetostrictive material. The preparation of the fibers, application of the magnetostrictive material to the fiber, and sensor arm characterization are described in this section. The sensor arms fabricated were based on the designs presented in the previous chapter. However, there are some differences between the sensor arms designed and those fabricated. The differences resulted from fabrication difficulties and actual sensor performance results. A table summarizing the characteristics of the fabricated sensor arms is included in the next chapter.

Preparation. Both classes of sensor arms required that the optical fiber be prepared. One meter was chosen as the length of the sensor arm since this distance was adequate to make connections in the interferometer without having excess fiber length. The one meter length was also sufficient for the mode-stripping, jacketing material to absorb extraneous modes propagating in the cladding. The extraneous modes are introduced into the fiber by non-ideal coupling of light into the fiber. Surplus fiber length in addition to the one meter standard would just add environmental noise to the sensor.

In order for the magnetostrictive material to have a maximum effect on the fiber, the magnetostrictive material must be as close to the fiber's core as possible. The first step in achieving this proximity was to remove the jacketing material around a 10 cm interior segment of the fiber. This length was chosen to match the extent of the Helmholtz coil's uniform magnetic field. The entire length of fiber was not stripped since the jacketing material provides mechanical strength and absorbs extraneous modes. Without the jacket, the fiber is extremely fragile. Since an interior section of fiber was to be stripped, a microstripper was not appropriate. Instead, the section of fiber to be stripped was placed in a chemical solvent (Star Bronze, Model Zipstrip, Alliance, OH) for a few minutes. The chemical solvent softened the jacketing material enough such that this layer peeled away after being gently rubbed. Although this method of stripping an interior length produced the best results, the method was not ideal since approximately one quarter of all the fibers broke while being stripped.

Once the fiber was stripped of its jacketing material, the bare silica was cleaned. The cleaning process involved a multistep procedure consisting of sequentially dipping the fiber in acetone, methanol, buffered hydrofluoric acid, and deionized water. The fiber was allowed to remain in each solution for two minutes. The acetone and methanol served to remove the chemical solvent and any remnants of the jacketing material. The 4:1 NH_4F:HF buffered hydrofluoric acid solution slightly etched the bare silica, which was done to enhance adhesion of the magnetostrictive material to the fiber. Following cleaning, the fiber was placed in an oven at 70°C for twenty minutes to remove absorbed moisture. The caustic nature of the cleaning process required gloves to be worn while cleaning the fibers. The handling required to implement the cleaning resulted in approximately one third of the fibers breaking.

Thin film sensor arms. In the first class of sensor arms, the thin film of magnetostrictive material was applied using a RF sputtering system (Denton Vacuum, Inc., Model DV 602, Cherry Hill, NJ). This following discussion describes the procedures used to sputter the metal, thermally anneal the fibers, and characterize them.

To fit the fiber in the sputtering chamber, the jacketed end lengths of the fiber were coiled into approximately four centimeter circles, which were loosely held together with masking tape. The coiled ends of the fiber were then placed on two stacks of four microscope slides such that the bare section of fiber was suspended approximately 0.5 cm above the deposition system's vacuum chamber floor. The coiled ends were then masked from the deposited metal by placing microscope slides over them.

Masking was also used on the bare interior section of one fiber to produce a geometrical design with the deposited metal. In order to produce a spiral coating configuration, a 0.05 mm nickel wire was wrapped around the fiber with a pitch of 2 mm. After the metal was deposited, the nickel wire was carefully removed. In order to produce an approximate semi-cylindrical pattern, the fiber was positioned on a piece of masking tape.

Once the fibers were placed in the chamber directly beneath the sputtering target, the enclosure was evacuated, and the RF power was applied. The three metal sputtering targets (cobalt, iron, and nickel) and fresh fiber samples were interchanged between sputtering runs. After the chamber was pumped down to 2 x 10^{-5} Torr, increasing amounts of argon gas were introduced into the chamber. With the RF forward power set at 500 W, the argon pressure was allowed to increase until the plasma formed. Plasma formation was marked by a blue glow in the chamber and a drastic reduction in the RF reflected power. The argon pressure required ranged from 7 to 15 Torr. Once the plasma was formed, the argon pressure was decreased to just sustain the plasma. For nickel, this pressure was 0.5 Torr, but for cobalt and iron, this pressure was 6 to 7 Torr. The argon pressure was decreased to prevent the cryo pump from becoming saturated before the sputtering run was finished. After the sputtering process had continued for the time required for the desired film thickness, the RF power was shut-off, and the fibers were allowed to cool for one hour. Once the fibers cooled, they were removed and immediately attached to plexiglass strips for mechanical support.

In order to test the effects of thermal annealing on the sensor's performance, three of the sputtered fibers were later placed in an oven (Sheldon Manufacturing, Model 1610D, Cornelius, OR). The fibers were arranged on a glass plate and heated to the maximum oven temperature of 350° C for two hours. Although this temperature is below the Curie temperature of the magnetostrictive materials investigated, it was the maximum temperature available in an oven. In order to test the effects of thermal annealing in the presence of an external magnetic field, the fibers were again placed on the glass plate which was resting on a laboratory horseshoe magnet. The magnetic field flux density of the horseshoe magnet was measured to be 1000 G at the center line between its two poles. The fibers, glass plate, and magnet were all placed in the oven and heated to 350° C for two hours. After this thermal annealing cycle, the power to the oven was shut-off, and the oven was allowed to cool overnight before the fibers were removed.

The metalized fibers were characterized for film thickness and quality. The film thickness was determined using a glass slide that was in the sputtering chamber with the fibers. This glass slide was partially masked with a grating. A profilometer (Sloan Dektak, Model 900051, Santa Barbara, CA) was used to determine the metal step height between the masked and unmasked portions on the slide. To determine the film quality, an optical microscope (Heerbrugg, Model Wild, Switzerland) was used. The microscope was used to examine the surface of the fiber for film roughness. In order to determine if the metal was uniformly deposited on the top and bottom sides of the fiber, a metalized fiber was cleaved and then inspected with the optic axis of the fiber facing the microscope.

Bulk sensor arms. The second class of sensor arms was composed of fibers bonded to a bulk piece of magnetostrictive material. A 30 cm long, 2.5 cm diameter nickel rod was obtained from Art Beecraft of the Electronic Technology Laboratory. This rod was labeled as 99 1% nickel. Other samples of high purity magnetostrictive materials could not be obtained before the research project was completed. In order to perform an accurate comparison of the different magnetostrictive materials, it would be necessary to evaluate identically sized samples of the different materials.

Once the fiber was cleaned and prepared, it was bonded along the length of the nickel rod with cyanoacrylate adhesive (Loctite, Model MIL-A-46050C, Puerto Rico). The procedure used to adhere the fiber to the rod was accomplished by holding the fiber flat against the rod and gluing one end of the fiber to rod and allowing it to dry. The fiber was then stretched taut and the other end was bonded and allowed to dry. After both ends were secure, the entire length of the fiber was glued to the rod. Variables in this process include the amount of glue used and the degree of tension on the fiber as it was being attached to the rod. After the rod and fiber combination was evaluated, the fiber and glue was scrapped off, and the rod was rubbed with acetone.

With only one magnetostrictive bulk material sample, the various sensor arms were fabricated sequentially. The first three sensor arms were used to test the effect of thermal annealing on sensor performance. The first bulk sensor arm was simply a single length of fiber bonded to the nickel rod. For the second sensor arm, the nickel rod was placed in an oxidation/diffusion furnace (Thermco, Model 201, Orange, CA) at 758° C for three hours. This temperature was chosen because it was above the Curie temperature of nickel. After allowing the rod to cool overnight, a fiber was attached to the rod. The third bulk sensor arm was processed identically to the second except that the nickel rod cooled while resting on the glass plate and under the influence of the 1000 G magnet.

The final two bulk sensor arm configurations involved no further processing of the nickel rod, but did require modifications of the fiber attached to it. The fourth bulk sensor arm incorporated a thinned fiber. The thinned fiber was prepared by etching it in a 1:1 HF:NH_4F solution for forty minutes. The etched fiber was compared to a full-sized fiber with an optical microscope. The thinned fiber was then attached to the rod. Thinned fibers were not RF sputtered because they would not have survived the handling. The last bulk sensor arm was fabricated to test the effect of the active region of the fiber's length on the sensor's performance. To accomplish this objective, a single fiber with three 10 cm bare silica lengths was attached to the nickel rod.

Interferometer Arrangement

After the sensor arms were fabricated, the remainder of the sensor was assembled. This section, which describes the sensor's configuration, is subdivided into two parts. The first part, fiber optic cable fundamentals, describes the equipment and procedures used to work with the fiber optic cables. The second part details the remaining components and procedures used to fabricate three versions of a fiber optic Mach-Zehnder interferometer.

Fiber optic cable fundamentals. Working with fiber optic cables required developing techniques to cleave the ends of fibers, couple light into the end of the fiber, and make fiber splices.

In order to minimize loss at each fiber connection, the ends of the fiber must be smooth, flat, and perpendicular to the optical axis of the fiber. Properly prepared fiber ends were achieved by cleaving the fiber. The first step in cleaving a fiber was to use a microstripper (Utica, Model MS, Orangeburg, SC) to remove the fiber optic cable's jacket material along a length that is within 4 cm of the fiber's end. Microstrippers operate just like wire strippers. The fiber was then cleaved with a fiber cleaver (Fujikura, Model CT-02, New York, NY), which is a small device that scores the fiber with a carbide edge, and then bends it to cause a clean break.

The fiber end was then inspected using the fusion splicer (Orionics, Model FW-303, Bozeman, MT). The fusion splicer possesses the necessary optics, lamp, and viewer to accomplish this task. If the fiber's end surface was not as smooth when compared to the example pictures included in the fusion splicer manual, a small amount of heat was applied to the end of the fiber to flatten its surface. Both the duration and amount of heat applied are controllable variables associated with the fusion splicer. Another method for examining the quality of a cleaved fiber is to examine the quality of laser light exiting a fiber. A high quality cleave produces a uniform and sharply-defined circular spot, whereas a low quality cleave produces a distorted and irregularly-shaped region of light.

The last method of testing a fiber's cleave requires launching light into the fiber. Coupling laser light into the end of a fiber involves aligning a laser beam whose diameter is approximately 1 mm and focusing it down to the fiber's core diameter of 3.5 um. This task was achieved using a fiber light coupler (Newport, Model F-916, Fountain Valley, CA), which was borrowed from Dale Stevens of the Electronic Technology Laboratory. The fiber light coupler consists of a 20X microscope objective and a brass ferrule fiber holder. The fiber holder has micrometer adjustments in three perpendicular directions and tilt adjustments in two directions.

To couple light into the fiber, it was important that the beam be perpendicular to the plane of the microscope objective. A slight departure from the perpendicular condition prevents efficient coupling of the light into the fiber. Before the fiber holder was positioned in the light coupler, the beam was examined to ensure that it was passing through the center of the aperture where the fiber holder is secured. Since the light is rapidly diverging after being focused, a clean circular spot indicated proper alignment. One end of the fiber was then positioned in the fiber holder with approximately 2 mm of the fiber protruding from the holder, while the other end was attached to the optical power meter (described later). The 2 mm length of the extended fiber was essential for positioning the fiber's end the correct distance from the microscope objective.

The technique used to couple light into the fiber's core was similar to the method used to couple light through a spatial filter. That is, the fiber holder was initially positioned a great distance from the microscope objective such that the diverging beam's size was very large, which also ensures that some of the light enters the fiber core. The other two positioning micrometers were adjusted to maximize the light on the output power detector which served to center the core on the beam since the $TEM_{0,0}$ beam had more power towards the center of the beam. The two tilt micrometers were also adjusted to maximize the output power. After the two tilt micrometers were adjusted once, it was not necessary to change them. The fiber holder was then moved several full rotations, and the two positioning micrometers were used to maximize the output power. This procedure of rotating the fiber holder and adjusting for maximum output power was repeated approximately six times until the output power was maximized.

Most applications of fiber optic cables require that two fibers be joined together in a splice. Two pieces of equipment were investigated to make fiber splices: the fusion splicer and glass ferrule tubes (Norland, Model 20125, New Brunswick, NJ). The best method for forming a splice, regardless of which splicing equipment was used, was to begin with laser light being launched into the first of the two fibers that are being spliced. The light from the first fiber was measured with the optical power meter before being joined to the second fiber. The light from the second fiber was then monitored with the optical power meter as the two fibers were being adjusted and spliced.

The fusion splicer joins two fibers together by simply melting their ends together. The glass ferrule consists of a precision made tube whose internal diameter ports are only slightly greater than the diameter of the fiber. To form a splice with the glass ferrules, each fiber end was dipped in index matching gel and inserted into the glass ferrule until the two fibers met in the center. The glass ferrule was then mounted on a splice holder (Norland, Model Splicemate, New Brunswick, NJ) to prevent unwanted movement of the glass ferrule or fibers.

<u>Fiber optic Mach-Zehnder interferometers</u>. Once the techniques required to work with fibers were established, three

different fiber optic Mach-Zehnder interferometers were fabricated to investigate particular aspects of the sensor. The three interferometers are illustrated in Figures IV.1, IV.2 and IV.3. The GaAs fused coupler interferometer was only constructed to verify the performance of the fused couplers. This part describes the remaining unique equipment used, criteria for choosing the equipment, and the arrangement of the interferometers. Standard optical equipment such as lenses, mirrors, and beam splitters will not be described in detail.

The first requirement for assembling an interferometer was to have an optical bench that was isolated from floor vibrations. The 3.5 m x 1.2 m air-cushioned optical bench in Room 127, Building 640, provided adequate vibration isolation. When the air table was floating correctly, the interferometer produced useful results, such as a visible fringe pattern. When the air table rested on its support platform due to loss of the compressed air utility, no fringe pattern was visible. Even partial floating of the table caused problems. The fringe pattern was degraded significantly when one of the compressed air valves malfunctioned and caused one leg to loose its support capacity.

The optical components were arranged on five one meter long rectangular rails (Oriel, Stratford, CT) that were bolted onto the air table. Each component was mounted on the rail using translation stages (Oriel, Models 11621, 14781, and 16021, Stratford, CT). These stages provided translation in three

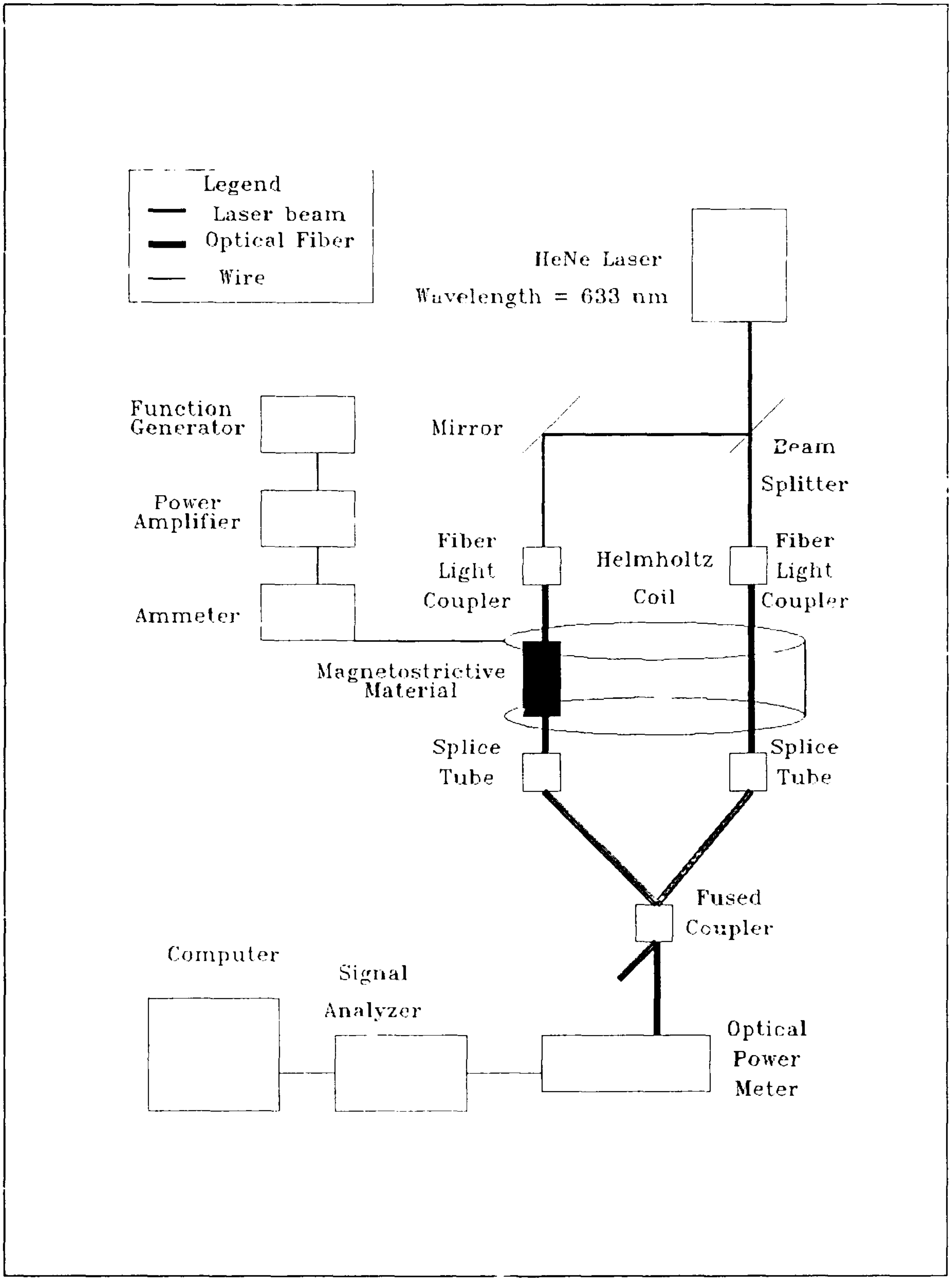

Figure IV.1. HeNe Fused Coupler Interferometer

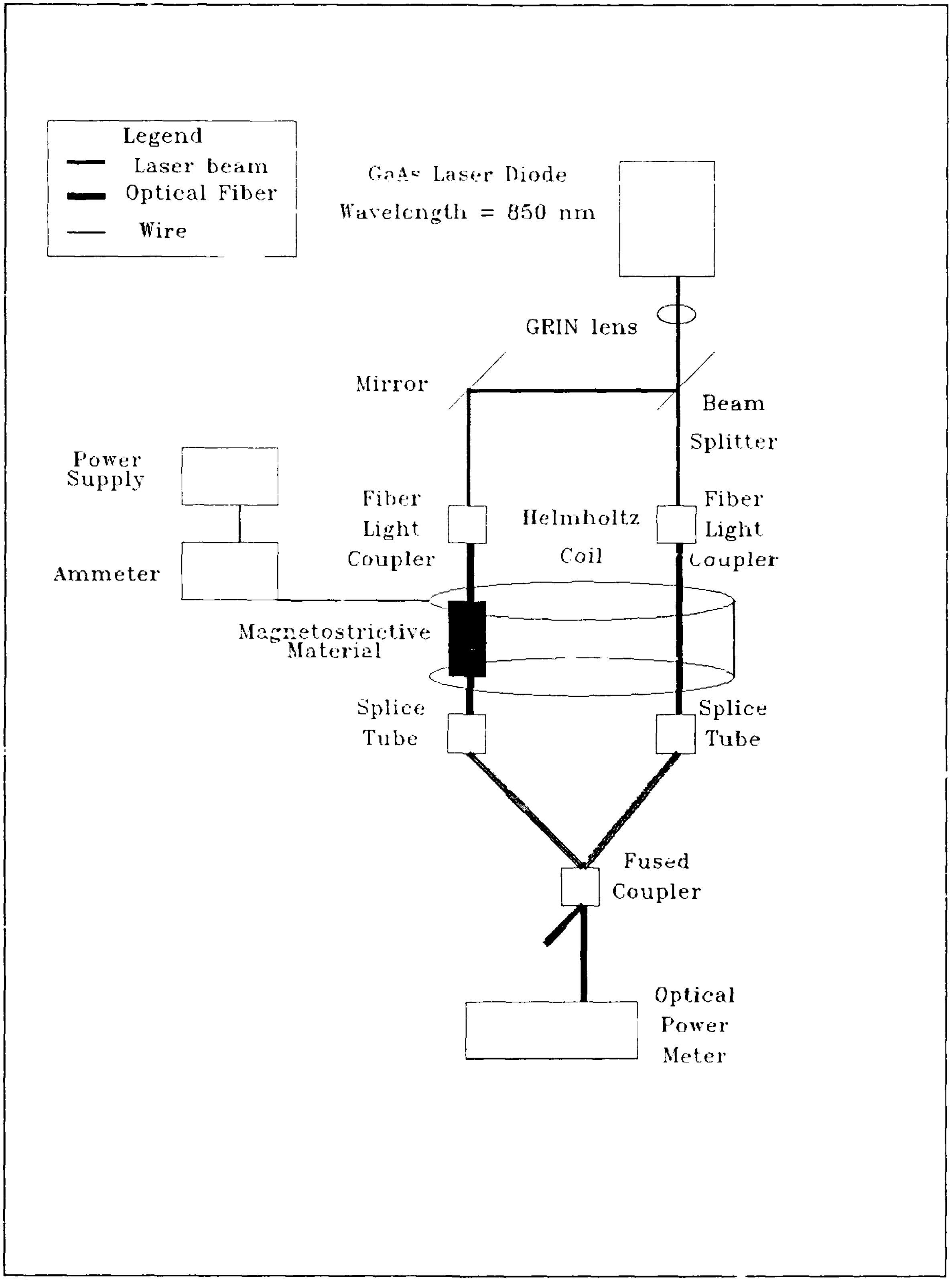

Figure IV.2. GaAs Fused Coupler Interferometer

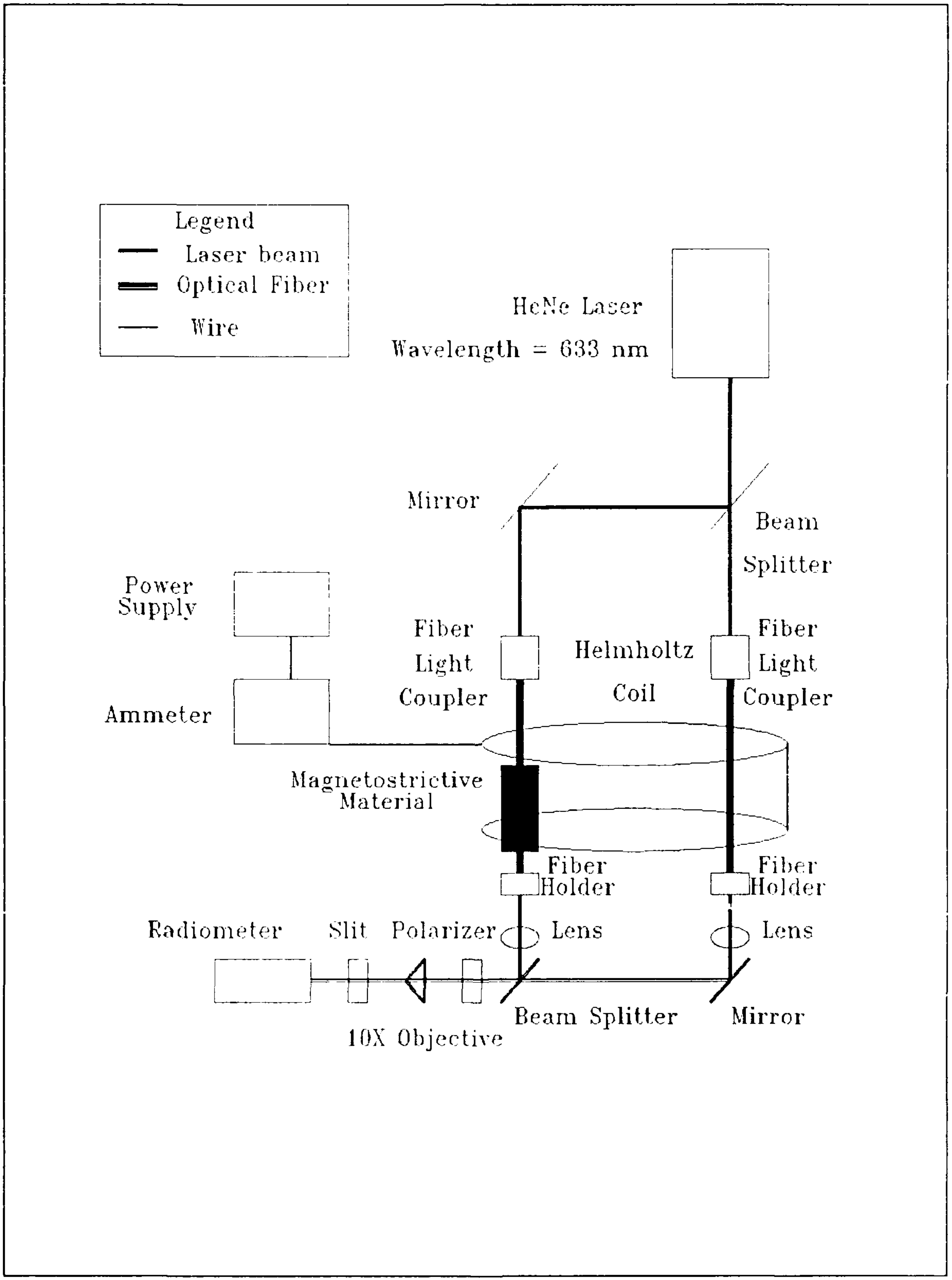

Figure IV.3. HeNe Fringe Pattern Interferometer perpendicular directions. The laser was mounted on a special stage (Oriel, Model 16162, Stratford, CT) that was specifically designed to hold a laser tube and provided translational and tilt adjustments. The rails and stages were necessary to achieve the precise optical alignment required to couple light into the fiber and form interference patterns.

The optical source used for the magnetic field fiber optic sensor was a 2 mW HeNe laser (Oriel, Model 79360, Stratford, CT). The HeNe laser was selected because of its availability and performance characteristics. The wavelength of the laser's output was 0.633 um, which is compatible with single-mode operation of the York Technology, Model SM600, fiber optic cables. As explained in the interferometer's operation section of Chapter III, the laser's output power must also be stable, polarized, and coherent. The laser's output power and polarization were measured with a radiometer and polarizer. By examining the fringe pattern of the interferometer with various differences in the length of the two arms, the coherence length of the laser was examined.

Two different light detectors were used with the different interferometer arrangements. The first detector was the optical power meter, a device made specifically to be used with optical fibers. The components of the optical power meter include: an optical adapter (Hewlett-Packard, Model HP 81510C, Palo Alto, CA) which serves to hold the optical fiber, an optical head (Hewlett-Packard, Model HP 81511A, Palo Alto, CA) which houses the optics and detector, and the optical pulse power meter (Hewlett-Packard, Model HP 8151A, Palo Alto, CA) which incorporates the detector's signal display electronics. With this combination of accessories, the optical power meter had the necessary characteristics to detect light in the fiber optic interferometer. The detector's wavelength sensitivity spanned 550 to 950 nm, which included the laser's wavelength (633 nm). The optical power meter's bandwidth of 250 MHz permitted detection of the time varying light from the interferometer. Light in the pW range could be detected with the optical power meter. Finally, the optical power meter has an optical-to-electrical transducer that provided the electrical signal used to characterize the interferometer's output light.

A radiometer (EG&G, Model 450, Salem, MA) was the second type of light detector used. The radiometer was used when bulk optics were used to recombine the light beams in the interferometer. The optical adapter prevented using the optical power meter for this application. Like the optical power meter, the radiometer's characteristics were appropriate for the interferometer. The radiometer was sensitive to the 0.633 um laser radiation, and its silicon detector's bandwidth of 6.25 MHz was sufficient to follow changes in the interferometer's light output. Although not as sensitive as the optical power meter, the nW sensitivity of the radiometer was adequate to make measurements. The radiometer also had an optical-to-electrical transducer.

The final unique component used in the fiber optic interferometer was the fiber optic fused coupler (York Technology, Model SC-633-50-0.5, Hampshire, England and Allied, Model 945-120-1001, Spring, TX). The fused coupler, as shown in Figure IV.4, is a four port device that was used to recombine the light in two of the interferometers. It is composed of dual single-mode fibers whose cladding layers has been thinned to less than a micron so that the two cores are in close proximity for a few centimeters (33:477). Through evanescent field coupling, light from one core can leak through the thinned cladding into the next core. The insertion loss, which assumes light enters only from port 1, is defined as 10 $\log_{10}[(P_2+P_3)/P_1]$ was specified as -0.34 dB. The coupling ratio, 10 $\log_{10}[P_3/(P_2+P_3)]$, was reported as -2.91 dB (34).

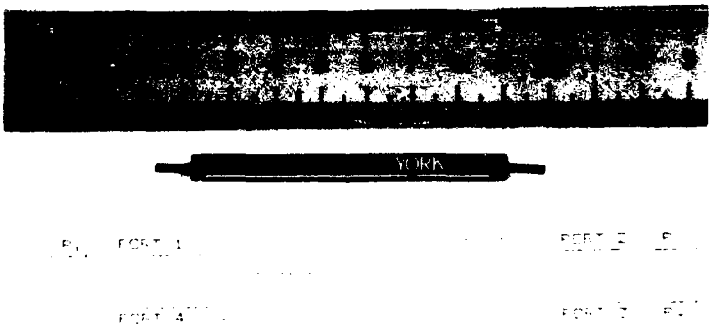

Figure IV.4. Fiber Optic Fused Coupler

Once all the major components were chosen, the interferometers were arranged as shown in Figures IV.1, IV.2, and IV.3. Techniques required for all the interferometers are described, and then the special methods required for each particular interferometer configuration are reported.

For all the interferometers, it was critical that the laser beam propagate at the same height along or perpendicular to the rails. The beam's alignment was checked using two identical apertures after it passed through each optical element. The two apertures initially were positioned close to the optical element. The alignment of the optical element was altered to keep the beam passing cleanly through both apertures when the second aperture was moved a distance of one meter from the optical element.

It was also critical that the fiber optic cable, in all the interferometer configurations, to be securely fastened to a flat surface. Any fiber suspended in the air would vibrate and cause additional noise in the sensor. All possible lengths of fiber were taped down to a flat surface. The sections that could not be in contact with a surface, such as the lengths protruding from the fiber light coupler, were held taut to minimize movement. In order to minimize the ambient air flow in the laboratory, the ventilation vents in the ceiling were obstructed. The fiber optic cable portion of the sensor was also covered with cloth to minimize any remaining ambient air turbulence.

The HeNe fused coupler interferometer did not require any further techniques to be assembled. This arrangement replicates most fiber optic interferometer sensors described in the literature with one exception. The mirror and beam splitter were used instead of another fused coupler with two additional splices. The rational for this modification was the need for equal power in each arm of the sensor. While the fused coupler would evenly split the light, there would be uncertainty in the loss of each splice. The loss of the first splice could be characterized, but the instant the second splice was connected, the measurement was affected by the operation of the interferometer. By using the beam splitter and mirror, the light in each arm was easily temporarily blocked to measure the optical power in the other arm.

The GaAs fused coupler interferometer required developing techniques for working with infrared radiation from a multi-mode fiber. The optical source for this interferometer was a GaAs laser diode which was attached to a multi-mode fiber pigtail (Spectra Diode Labs, Model SDL-2410-H1, San Jose, CA). The beam was viewed with night vision goggles (ITT, Model 4934-A, Roanoke, VA). The rapidly diverging light from the fiber pigtail could not be directly coupled into the single-mode fiber with the fiber light couplers. To collimate the radiation, a graded index (GRIN) lens (Nippon Sheet Glass, Model SRL, Somerset, NJ) was used. The profile of the index of refraction of a GRIN lens is designed to collimate an incoming diverging beam. Once the infrared radiation was collimated, no further special techniques were used to fabricate the GaAs fused coupler interferometer.

Unlike the HeNe fused coupler interferometer, the HeNe fringe pattern interferometer required more techniques to be developed since it required the light in the sensor and reference arms to be collimated and recombined. With respect to the laser and the sensor and reference arms, the two interferometers are identical. For the fringe pattern interferometer, the fibers were terminated in fiber holders which were similar to the fiber light couplers, except that they did not have the microscope objective. Since the fiber's core approximated a point source of light, the beams were collimated by placing a 25 mm focal length lens one focal length from the end of the fiber. The exact position of the lens was adjusted until the spot size of the laser beam was the same just after the lens and several meters from the lens.

A fringe pattern was formed on the radiometer by recombining the beams using a mirror and beam splitter. It was necessary to use a mirror mount with precision micrometer tilt adjustments (Newport, Model 600A-2, Fountain Valley, CA) to form a fringe pattern. The beam splitter could be mounted in a standard laboratory mount (Newport, GM-2, Fountain Valley, CA) since once it was aligned, it was not altered. The fine adjustments were achieved using the mirror mount. No fringe pattern was visible while the mirror was being adjusted. A small adjustment was made and then the interferometer was allowed to stabilize. The spacing and curvature of the fringe lines were determined by the alignment and collimation of the beams. Reflections from the front and back side of the beam splitter caused a secondary fringe pattern to be formed. This secondary fringe pattern resulted in smaller light and dark bands within the larger light and dark bands.

Once the beams were recombined, a polarizer and 10X microscope objective were used to view the fringe pattern. The polarizer was necessary to ensure that the polarization of the two recombined beams was identical. Although the light from the single mode fiber was measured to be more than ninety percent polarized in one direction, the polarization direction was dependent on the orientation of the fiber. For the highest fringe visibility, the output power from each arm after the polarizer was made equivalent. The optical power was decreased in one arm until it matched the optical power in the other by defocusing one of the fiber light couplers which caused less light to be launched into the fiber. The 10X objective was used to magnify a portion of the fringe pattern. A 0.5 mm x 0.5 mm slit was placed before the radiometer to sample a small portion of the fringe pattern.

Sensitivity Measurements

Once the sensor arms were fabricated and the interferometers were assembled, the sensor's sensitivity was measured. Signal processing equipment and techniques were required to quantify the sensor's response. This section describes the equipment and techniques used to make measurements of the sensor's response to

DC and AC magnetic fields.

DC measurements. Both the HeNe fused coupler interferometer and the HeNe fringe pattern interferometers were used to make DC magnetic field measurements. The method for quantifying the sensor's response was to make measurements of output power for different current levels in the Helmholtz coil.

To verify that the sensor sensitivity measurements were valid, a sensor arm with a known response was used. This new sensor arm was a fiber wrapped around a 5 cm wide piezoelectric (PZT) ring (Veritron, Model 24-32200-5A, New Bedford, OH). As explained before, placing a voltage across the PZT ring causes its outer dimension to change, which would simulate a fiber being stretched by a magnetostrictive material. The PZT ring was tightly wrapped with ten turns of fiber with the two end points being glued to the ring. Different DC voltage levels were applied to the PZT ring to simulate the effect of DC magnetic fields on the magnetostrictive material sensor arms.

AC measurements. The HeNe fused coupler was the only interferometer used to make AC measurements. The equipment used to make the measurements is first reported, which is followed by a description of the method used to quantify the sensor's performance.

The signals from the optical power meter and function generator served as inputs to the dual-channel signal analyzer (Bruel & Kjaer, Model 2032, Marlborough, MA), which served as a digital storage oscilloscope and spectrum analyzer. The information from the signal analyzer was output via a GPIB interface card (MetraByte, Model IE-488, Taunton, MA) to a personal computer (Zenith, Model Z-248, St. Joseph, MI). Two BASIC computer programs, which are included as Appendix D, were written to control the signal analyzer and store the measured data. The first program permitted the operator to switch between viewing single and dual displays of the signals' time- and frequency-domain characteristics. This program also stored the digitized displays. The second program was used to store the spectral information spanning 23 to 27 Hz.

The method used to determine the sensor's sensitivity was to examine the frequency content of the interferometer's output. Before the Helmholtz coil was energized, the sensor's output spectrum was measured thirty times, averaged, and stored as a baseline noise file in a BASIC data file. The magnetic field was then generated and the sensor's output spectrum was again measured thirty times, averaged, and stored as a signal file in another BASIC data file. The two files were then imported into the LOTUS 123 spreadsheet program so that the noise file could be subtracted from the signal file to form the sensor's response file. As was done with the DC measurements, the PZT ring sensor arm was used to verify that the instrumentation configuration and data processing scheme used to quantify the sensor's response was valid.

With the magnetostrictive material sensor arms as part of the interferometer, the sensor's response was investigated to ensure that the response was due to the magnetostrictive effect in the sensor arm, and not a noise source. Three experiments were conducted to prove that the sensor was operating correctly. The initial step of the first experiment involved energizing the Helmholtz coil and examining the frequency content of the output signal. The output signal was then examined when the light was only allowed to propagate in either the sensor or reference arm. This experiment proved that the sensor's response was due to an interference effect, and not some extraneous noise source, such as cross talk between the instrumentation's electrical cables. The second experiment required replacing the sensor arm with an uncoated fiber and then examining the sensor's response. The final experiment investigated the reproducibility of measurements taken with the bulk sensor arms. To ensure that any changes in the sensor's performance were not due to variations in the bonding of the fiber to the rod, the sensor's response was recorded after the same type of bulk sensor arm was constructed three times. After each measurement, the fiber was removed from the rod and re-bonded to the magnetostrictive material.

After the method of quantifying the sensor's response was validated, and the response of the sensor was verified to be the result of the external magnetic field, the sensor was evaluated with the different sensor arms. The output spectrum of the sensor with each different sensor arm was recorded for a series of different external magnetic field values.

Sensor Optimization

The AC measurements made thus far involved comparing the response of the sensor with different sensor arms relative to the same series of magnetic fields. Two final experiments were conducted to determine if the sensor's response could be improved without changing the sensor arm. In practice, the sensor should be more sensitive to a small AC magnetic field superimposed on a DC bias magnetic field compared to only a small AC magnetic field. This optimization concept corresponds to operating the sensor in the region of greatest slope depicted on the factional change in length vs the magnetic field plot shown in Figure III.9.

To examine this hypothesis, the sensor's response was tested for a 0.2 G AC magnetic field with various DC bias magnetic fields. Both magnetic fields were generated at the same time with the Helmholtz coil by adding a DC current level to the AC current from the function generator.

As the final experiment, the ultimate sensitivity of the sensor was evaluated. The sensor was composed of the sensor arm which proved to be the most responsive to the external AC magnetic fields. The sensor's response was recorded for decreasing AC magnetic fields that were superimposed on a constant DC bias magnetic field.

V. Results and Analysis

In this Chapter, the experimental results and an analysis of those results are discussed. The outcome of the Helmholtz coil calibration, sensor arm fabrication, interferometer arrangement, sensor sensitivity measurements, and sensor optimization are reported.

Helmholtz Coil Performance

The first measurements recorded were the characterization of the Helmholtz coil. Once the Hall effect magnetometer was calibrated, and the ambient magnetic field was determined, the performance of the Helmholtz coil was evaluated.

To calibrate the Hall effect magnetometer, the probe of the device was placed inside the zero gauss chamber, followed by the 95 G and 978 G reference magnets, respectively. As a result, the magnetometer measured 0 G, 90 G, and 980 G, respectively. The uncertainty of the magnetometer analog display was approximately one percent. Some of the calibration error may be due to the fact that the reference magnets have not been calibrated for several years. For the purposes of establishing the ambient magnetic field flux density and calibrating the Helmholtz coil, the magnetometer was deemed sufficiently accurate.

After the Hall effect magnetometer was calibrated, the ambient magnetic field flux density inside the magnetically shielded chamber and around the laboratory was established. Inside the test chamber, the DC magnetic field flux density measured a constant 0.215 G. Around the laboratory, the DC magnetic field flux density measured between 0.2 and 1 G. The DC magnetic field flux density did not vary with time at any location in the laboratory. The AC magnetic field flux density was correspondingly measured to be a constant 0 G both inside the test chamber and in various locations in the laboratory. The magnetically shielded chamber was not used for four reasons: (i) the ambient DC magnetic field flux density did not vary with time, (ii) the chamber did not significantly reduce the magnitude of ambient dc magnetic field flux density, (iii) there was no detectable ambient AC magnetic field flux density, and (iv) using the chamber would add additional environmental noise due to the longer lengths of fibers required.

Following the investigation of the ambient magnetic field conditions, the Helmholtz coil was characterized. The first experiment conducted with the Helmholtz coil was to record the magnetic field flux density at the on-axis center point between the two coils while varying the amount of AC and DC current flowing through the coils. The Helmholtz coil was wired such that the current flowed through 250 turns.

Figure V.1 illustrates the Helmholtz coil's experimental performance compared to its theoretical performance, which was predicted by equation 11 in chapter III. As shown, the DC magnetic field flux density is slightly greater than the theoretically predicted value. For example, at 550 mA, the dc magnetic field flux density is 102% of its theoretically

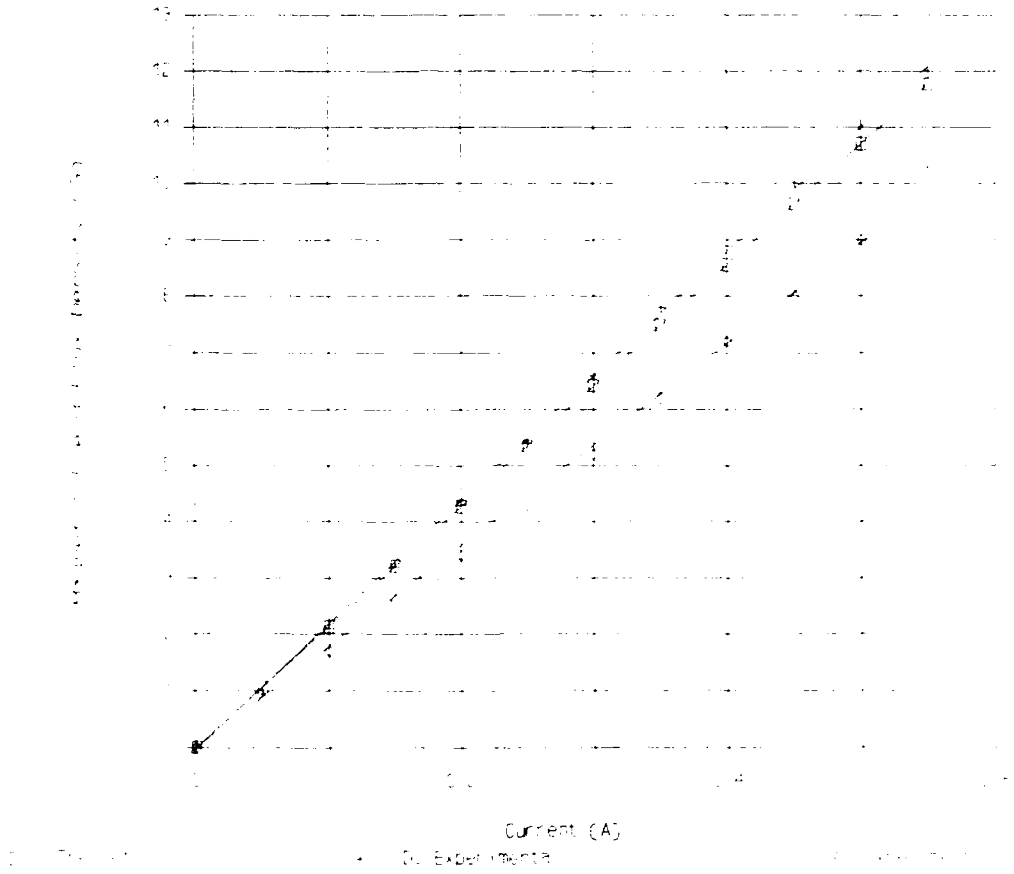

Figure V.1. Magnetic Field Flux Density Generated by the Helmholtz Coil for Varying Amounts of Current

predicted value. This small amount of error can be attributed to the measurement error of the magnetometer, and the fact that the Helmholtz coil has different coil separations and radii for each turn of wire.

For AC magnetic field flux densities, the measured value was below the theoretically predicted value. At 550 mA, the measured value was 87% of the predicted value. This discrepancy can be attributed to the distortion of the 25 Hz sine wave introduced by the power amplifier. This distortion altered the frequency content of the signal. In particular, the distortion introduced frequencies above the 400 Hz detection limit of the magnetometer. At lower currents, the distortion was not as severe, which explains why the experimental and predicted values converge at lower currents. Figures V.2, V.3, V.4, and V.5 depict the distortion of the sine wave caused by the power amplifier when 500 mA was drawn from the power amplifier.

The second experiment conducted with the Helmholtz coil was accomplished to record the magnetic field flux density at the on-axis center point between the coils for different numbers of turns of wire with a constant current of 250 mA. Figure V.6 shows the result of this experiment. The reasons for the discrepancy between the predicted and experimental values in this experiment are the same as for the first experiment.

The final experiment conducted with the Helmholtz coil was accomplished to examine the spatial variations of the magnetic field flux density generated. No variations in magnetic field flux density could be detected along the 10.5 cm centerline between the coils for AC or DC magnetic fields. No variations could be detected for 4 cm in a radial direction measured outward along the center line relative to the center point between the two coils.

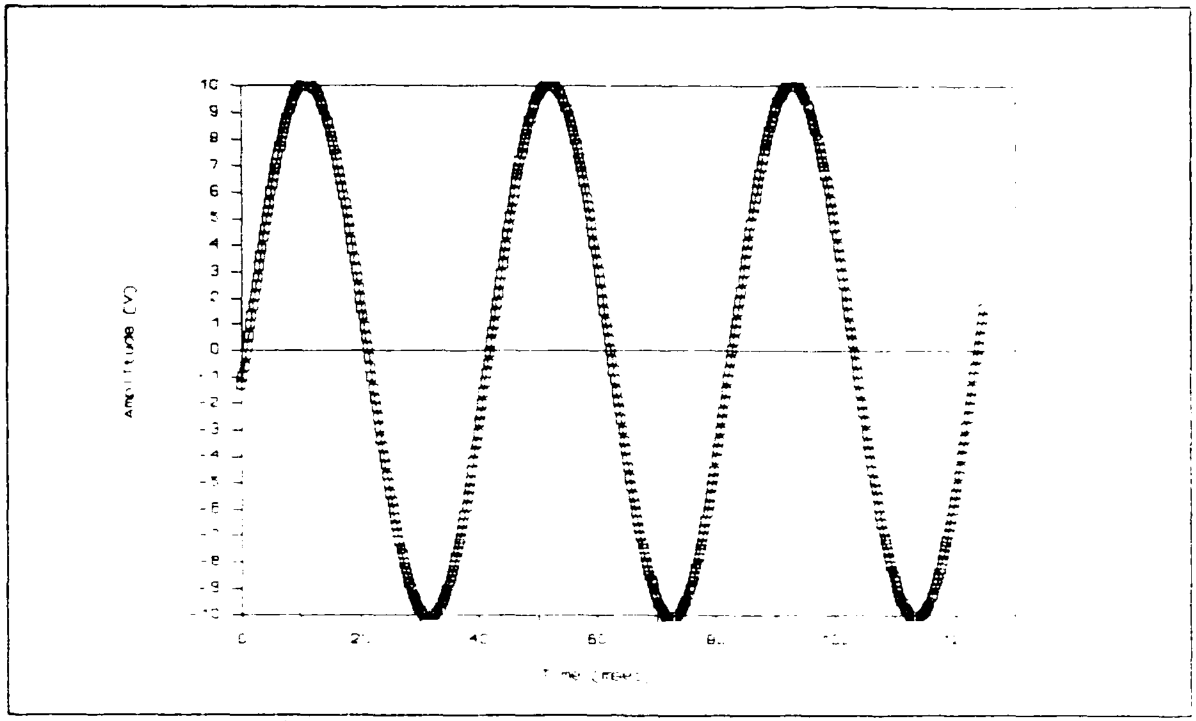

Figure V.2. Time-Domain Display of the Function Generator's Output

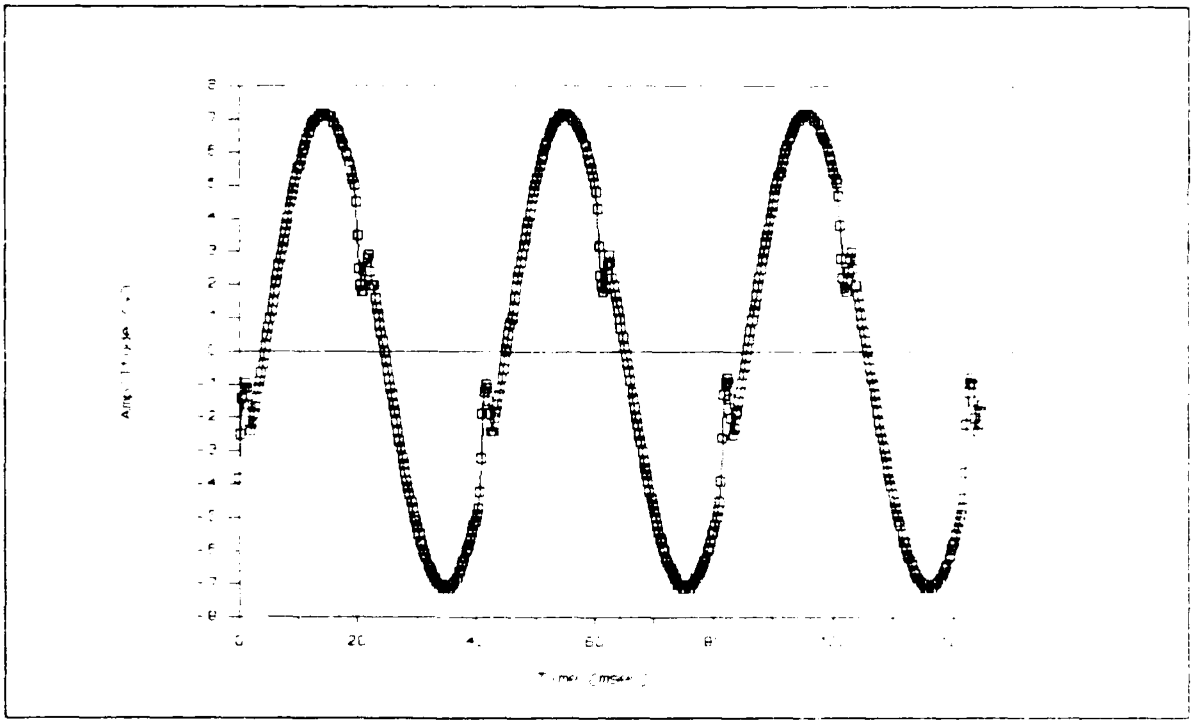

Figure V.3. Time-Domain Display of the Power Amplifier's Output

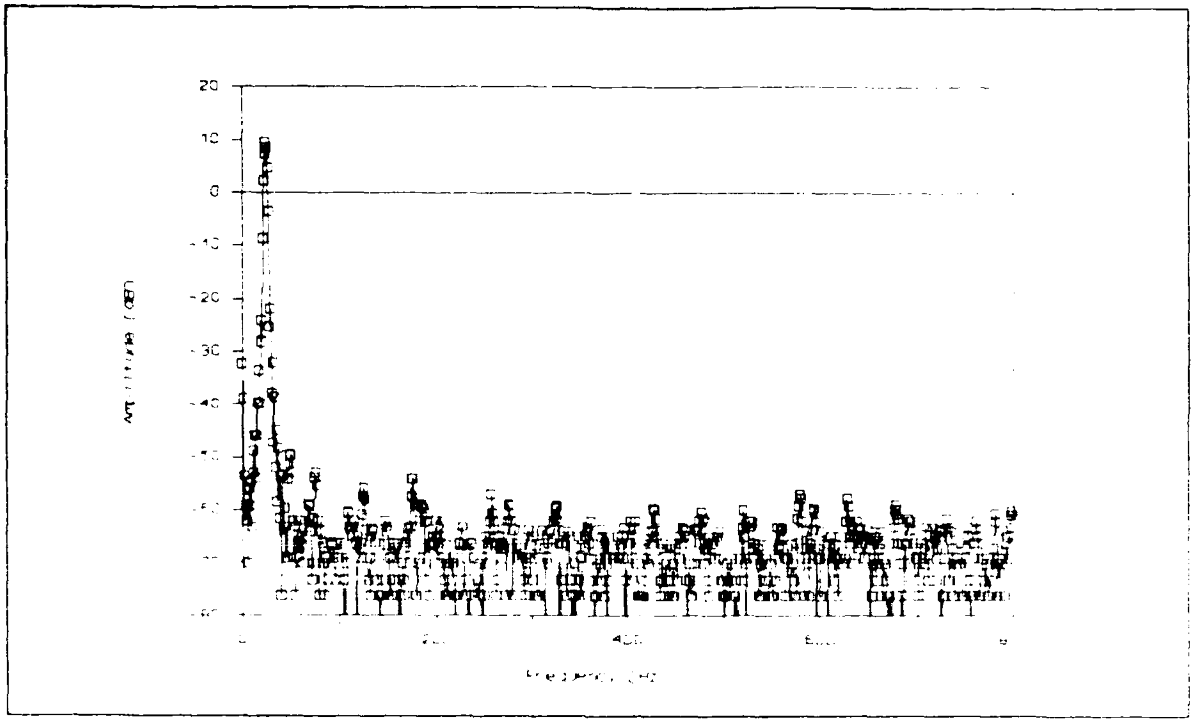

Figure V.4. Frequency-Domain Display of the Function Generator's Output

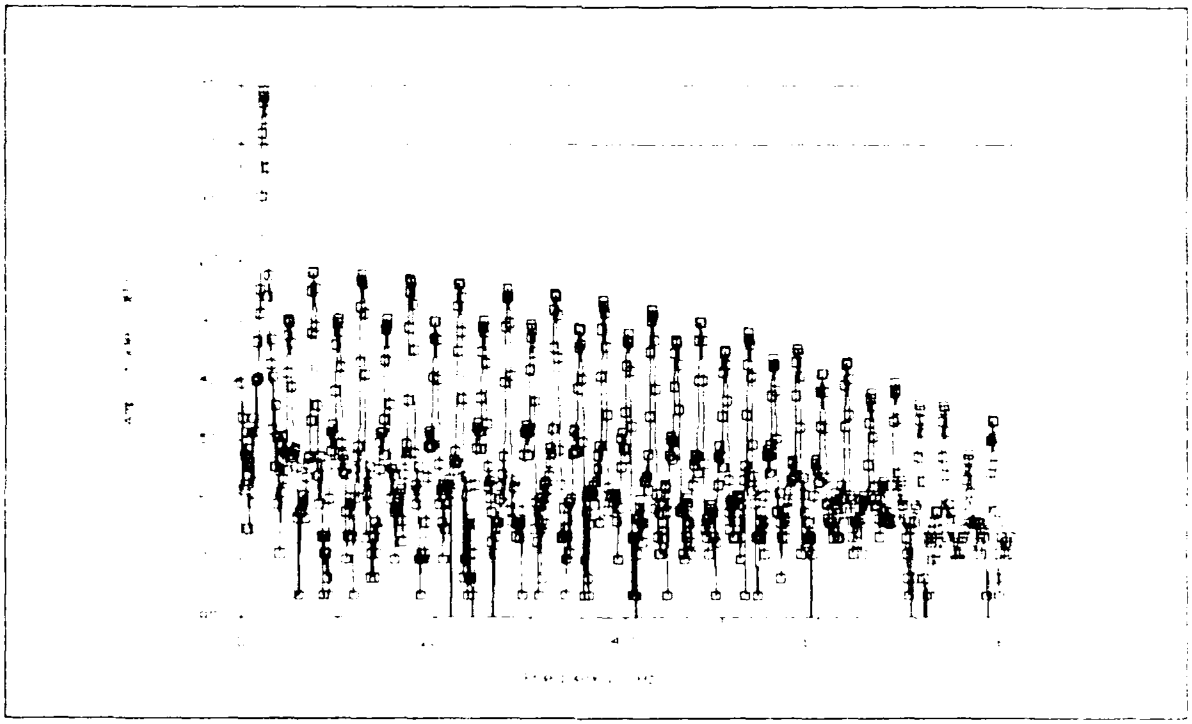

Figure V.5. Frequency-Domain Display of the Power Amplifier's Output

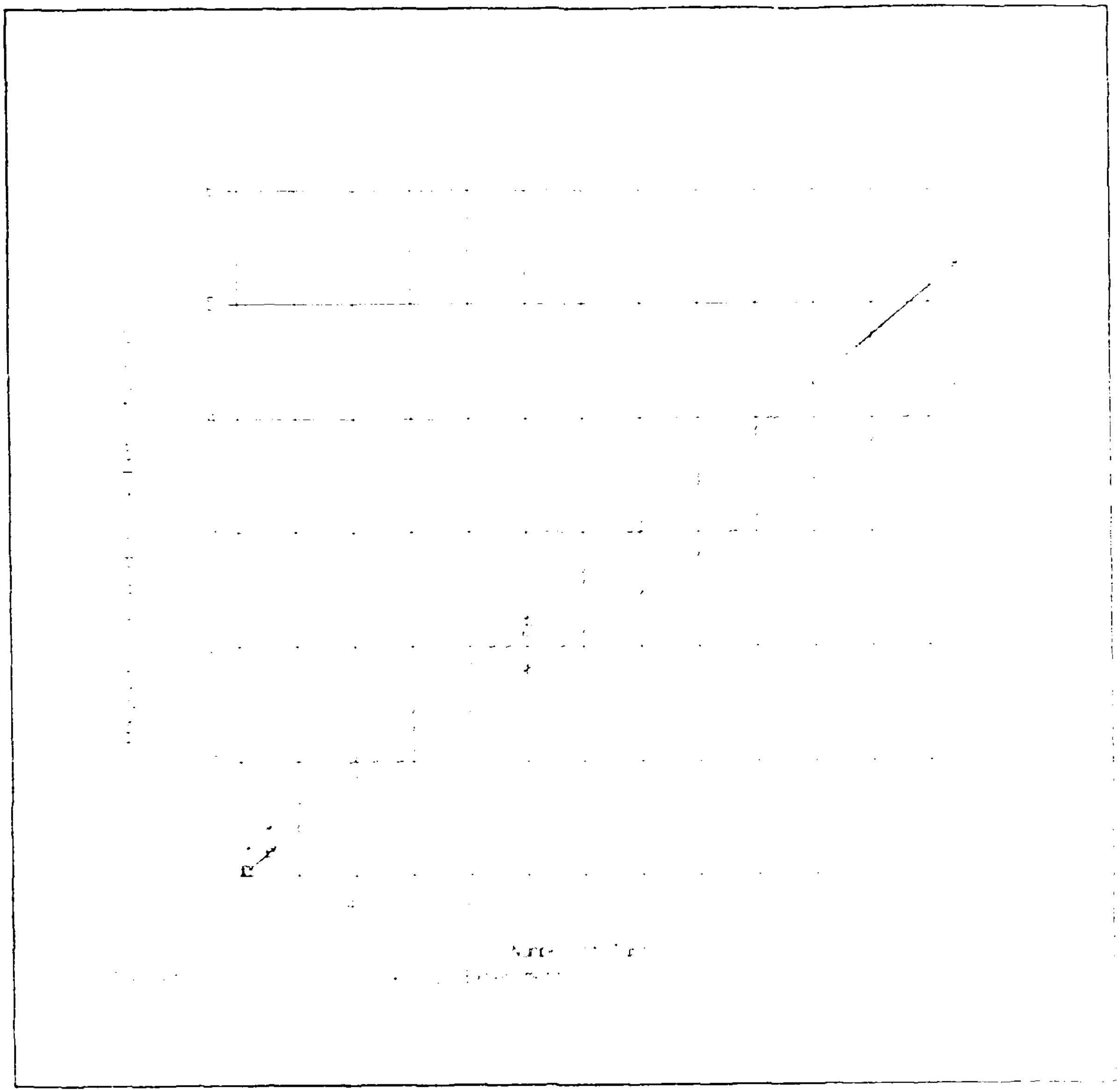

Figure V.6. Magnetic Field Flux Density Generated by the Helmholtz Coil for Varying Numbers of Turns [illegible]

To summarize the Helmholtz coil's performance, it was concluded that the difference between the predicted performance of an ideal Helmholtz coil and the performance of one [illegible] in a laboratory was sufficiently small to be acceptable. The

Helmholtz coil was capable of simulating biomagnetic fields, and consequently, it was used to challenge the fiber optic magnetic field sensor.

Fabricated Sensor Arms

Following the characterization of the Helmholtz coil, the sensor arms were fabricated. This section reports the results of fabricating the two classes of sensor arms: thin film sensor arms and bulk material sensor arms. Table V.1 summarizes the sensor

Table V.1. Fabricated Sensor Arms

Sensor Arm	Thin/Bulk	Material	Film Thickness	Comment
1	Bulk	PZT	N/A	Validation tool
2	Thin	Ni	9.5 um	-
3	Thin	Ni	4.8 um	-
4	Thin	Ni	9.5 um	Spiral design
5	Thin	Ni	8 um	9 lengths
6	Thin	Co	0.3 um	-
7	Thin	Fe	< 0.1 um	Possible Cu content
8	Bulk	Ni	-	As received
9	Bulk	Ni	-	Thermally annealed
10	Bulk	Ni	-	Thermally annealed with B field
11	Bulk	Ni	-	Thinned fiber
12	Bulk	Ni	-	3 lengths

arms fabricated for this research project.

Thin film sensor arms. Thin films of cobalt, iron and nickel were deposited on the fiber optic cables. It was an objective to fabricate the fibers with equal metal thicknesses. This part reports the difficulties encountered which prevented the designed sensor arms from being fabricated, and discusses the results of characterizing the metal coated fibers.

Cobalt and iron were difficult metals to deposit. Three and one half hours of sputtering cobalt resulted in a film thickness of only 0.3 um. Sputtering iron for one and one half hours produced a film thickness that was so thin that it could not be measured; it was sufficiently thin to be partially transparent. Based on the sensitivity limit of the profilometer when used to determine a film thickness on a glass microscope slide, an estimate of the iron film thickness was determined to be less than 0.1 um. The sputtering system may have not been operating correctly when the iron layer was deposited since some copper from the sputtering target base may have been deposited with the iron. Copper content in the deposited film was suspected due to the bronze tint of the deposited metal. Additional cobalt and iron coated fibers were not produced due to the disappointing sensor results of the nickel sputtered fibers.

As a softer metal than cobalt and iron, nickel was more easily sputtered. A 9.5 um thick layer of nickel was deposited in eight hours. Based on the relatively quick deposition rate and Figure III.9, which indicated that nickel experiences the largest magnetostriction effects, many different nickel fibers were fabricated as reflected in Table V.1.

To test the effect of sensor arm metal thickness on sensor performance, two fibers of different nickel film thickness were created. The first fiber was coated with a 9.5 um thick layer of nickel. A second fiber was sputtered for four hours, which resulted in a film thickness of 4.8 um. The fact that the film thicknesses were not exactly proportional to the duration of the metal deposition is not surprising since sputtering is not a linear deposition process.

To create fibers with different geometrical patterns, the fibers were partially masked during metal deposition. The semi-cylindrical patterns could not be fabricated because the tape used to mask the fiber could not be removed without breaking the fiber. Only one fiber was created with a spiral pattern due to the handling difficulties of wrapping a 0.05 mm wire around the bare fiber.

Three attempts were made to thermally anneal a sputtered nickel fiber, but each time the fiber broke inside the oven. As the fiber cooled, the thermal expansion coefficient mismatch must have been sufficient to break the fiber. For example, when the temperature of a nickel sample is raised from 293 to 400° K, the change in length relative to a nominal length is 0.15% (35:225). For a sample of silica experiencing the same change in temperature, the change in length relative to a nominal length is 0.12% (35:290).

The broken thermally annealed fibers do indicate that the metal adhered well to the fiber. The results of the optical microscope inspection indicate that metal film's surface was smooth and uniform. Figure V.7 illustrates an example of the nickel surface which also shows the notch from the spiral design on the fiber. The surface quality of the iron and cobalt coated fibers was similar to the nickel fiber. Various metalized fibers were cleaved to determine the uniformity of the deposited layers. The metal coating was not visible from the end view of the fiber, which was probably due to the thin coating thickness and uneven cleaving of the metal coated fiber.

Bulk material sensor arms. Bulk material sensor arms were fabricated as summarized in Table V.1. The fiber in one sensor

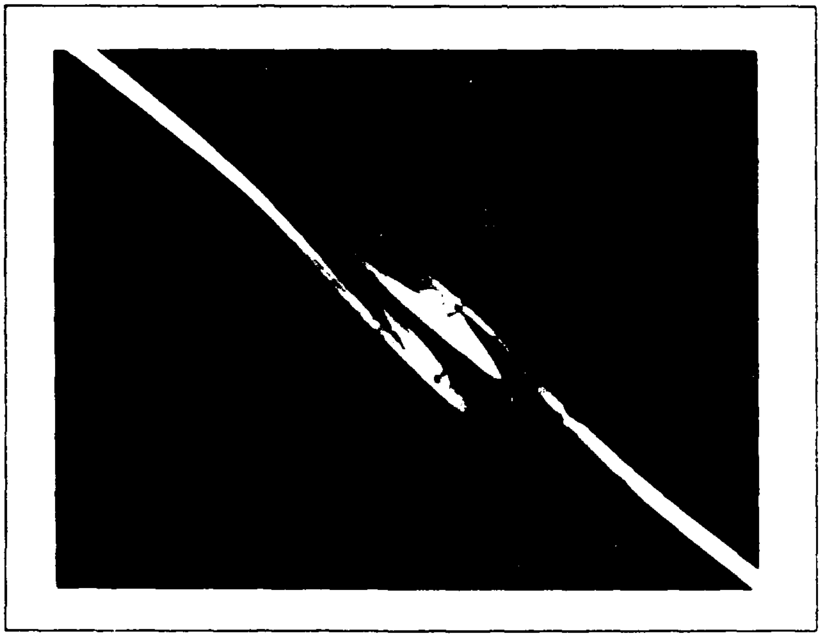

Figure V.7. Nickel Coated Fiber Surface Showing the Spiral Notch Pattern arm was thinned as shown when compared to a full-sized fiber in Figure V.8. Based on this photograph, the fiber's diameter was reduced approximately 48%, which corresponds to a 23% reduction in cross-sectional area.

Overall, fabricating the sensor arms from bulk materials was much easier than RF sputtering due to the fiber handling considerations and metal bonding techniques. The RF sputtering system was not an ideal system to apply metal to fibers. The most serious problem with the sputtering system was the amount of time required to deposit layers greater than 10 um thick. The sputtering system also suffered numerous mechanical malfunctions that not only delayed processing, but occasionally destroyed the samples.

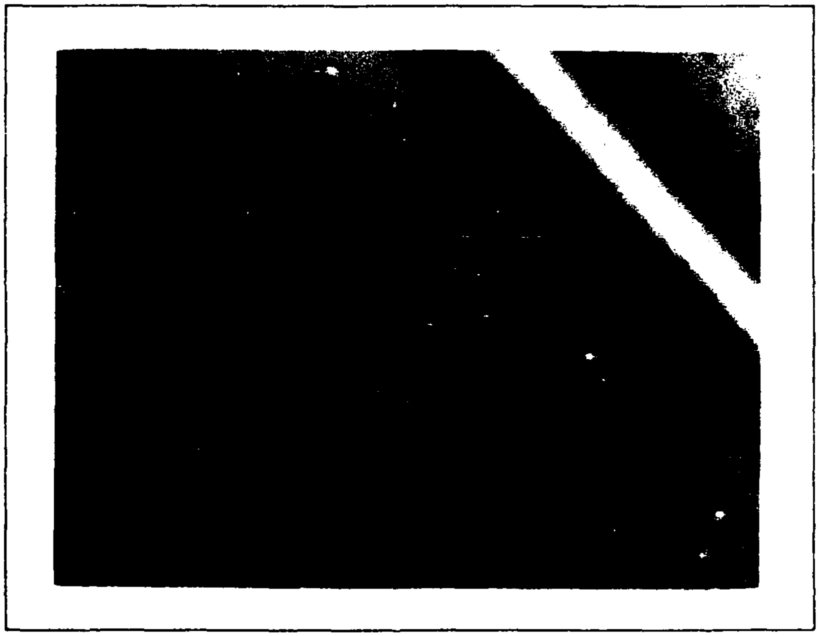

Figure V.8. Comparison of the Thinned Fiber with a Full Size Fiber

Interferometer Parameters

Once the sensor arms were fabricated, all the components were available to assemble the interferometers. This section reports the results of fabricating the interferometers in two parts. The first part describes the results of the procedures developed to work with fiber optic cables. The results associated with fabricating the interferometers are included in the second part.

Fiber optic cable results. This part documents the consequences of the techniques developed to cleave the ends of fibers, couple light into the end of the fiber, and make fiber splices. Except when otherwise noted, the maximum uncertainty in the optical power measurements was approximately five percent.

The initial fiber cleaver obtained did not produce adequate quality cleaves. When viewed with the fusion splicer optics, the ends of the fibers were observed to be not smooth and perpendicular to the optic axis of the fibers. The poor quality cleaved edges were attributed to the finite lifetime of the carbide edge and bending mechanism of the fiber cleaver. A newer fiber cleaver was borrowed from Dale Stevens of the Electronic Technology Laboratory. This cleaver produced high quality cleaved ends practically every time.

High quality cleaved fiber ends were necessary to couple light into the end of the fiber. Using the method outlined in the previous chapter, 400 uW from a 1.914 mW laser was coupled into the fiber. This loss of 7 dB was due to two following reasons: i) mismatch in the area of the focused laser spot size and the fiber's core and ii) mismatch in the numerical aperture (NA) between the microscope objective and the optical fiber. As a first level approximation, the laser spot size is considered a uniform circular beam of light whose area is 4.91×10^{-8} m^2. After passing through the 20X microscope objective, the focused spot size would then have an area of 1.23×10^{-10} m^2. With a fiber's core area of only 9.62×10^{-12} m^2, the expected loss would be 11 dB. Ignoring the gaussian nature of the laser beam and its actual interaction with optics accounts for the difference between the achieved light coupling and the expected light coupling. The numerical aperture (NA) affects the light coupling since it describes the solid angle of light focused from the microscope and the solid angle of light that will be accepted into the optical fiber (29:51). The NA of the microscope objective was 0.4, and the optical fiber's NA was 0.1. This mismatch in NA indicates that a portion of the light focused from the microscope objective will enter the fiber at an angle too large as measured from the optic axis to be propagated along the fiber. The only undesirable feature of the fiber light coupler was the plastic screw micrometers which required a fine touch during the final adjustment process.

Low loss splices also required high quality cleaved fiber ends. The fusion splicer proved to be inadequate to form splices. The available fusion splicer had only micrometer adjustments along the optical axis of the two fibers. The lack of adjustments in the outward radial directions prevented reproducible low loss splices, with most fusion splices resulting in over 5 dB of loss. The fusion splicer would be adequate for multi-mode fiber splices since the fiber core size is much larger than in single-mode fibers. The glass ferrule splice tube established itself as the superior technology needed for making single-mode optical fiber splices. Using the glass tubes, splices with less than 0.5 dB of loss were formed. A further advantage of using the glass ferrules is that the splices were temporary. However, as the glass tubes were reused, index matching gel bubbles accumulated in the tube causing higher losses of 1 to 2 dB.

In summary, the initial techniques required to use optical fibers were very time consuming. However, once the techniques were refined and practiced, optical fibers could be treated as any other optical component in the interferometer.

Interferometer Performance. The three interferometer configurations were assembled once the techniques to work with the fibers were developed. This part discusses the results of the characterization of the remaining optical equipment and describes the performance of the three interferometer configurations.

The optical power of the HeNe laser measured with the radiometer was 1.914 mW. The laser's optical power varied less than one percent of this value after it was allowed to stabilize for thirty minutes. HeNe laser output stability problems were experienced when reflections from the end of the optical fiber were directed back into the laser. This problem was corrected by providing a sufficient distance between the HeNe laser and the optical fiber. Since the laser could not be perfectly aligned with the optical fiber, the reflection deviated from the axis of the laser's output beam. When the distance between the laser and optical fiber was greater than 0.3 m, the reflected laser power did not couple back into the laser.

In addition to optical power, the laser's output was investigated for polarization and coherence. The polarization of the HeNe laser's output was measured to be linear. With a polarizer placed with its transmission axis parallel to the laser's polarization, the output power was measured to be 1.913 mW. When the laser's polarization was perpendicular to the transmission axis of the polarizer, the output power was measured to be 0.001 mW. The exact coherence length was not determined because the longest difference in path lengths was less than 1 m. Observed interference effects indicated that the coherence length of the laser's output must be greater than 1 m.

The final optical component to be characterized was the fused coupler. The coupling ratio agreed with the manufacturers reported figure of 2.91 dB within ten percent (34). An experiment was conducted to measure the coupling ratio by inserting light into port 1 of the fused coupler, and then measuring the output power in ports 2 and 3. The output power was measured to 155 uW and 180 uW for ports 2 and 3, respectively. These values indicate a coupling ratio of -2.70 dB. The insertion ratio was more difficult to measure since it involved other variables such as splicing efficiency or input light coupling. However, the insertion loss of the device was probably close to the stated value based on the average output power of the interferometer. More information on the fused coupler is included in the following discussion concerning the interferometer configurations.

After all the optical components were evaluated separately, the HeNe fused coupler interferometer was assembled as shown in Figure V.9. Table V.2 summarizes the measured power budget for the HeNe fused coupler interferometer. The value associated with the optical power measured by the detector is an average value (the minimum and maximum values were 1 uW and 67 uW).

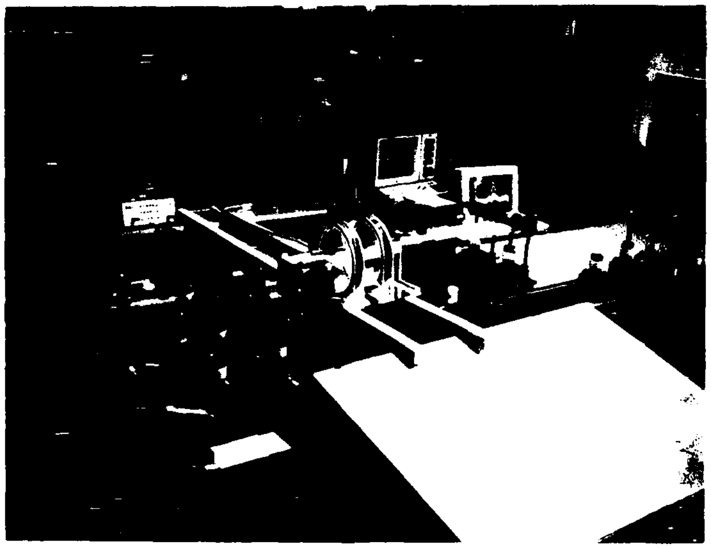

Figure V.9. HeNe Fused Coupler Interferometer

Table V.2. Example of the Power Budget for the HeNe Fused Coupler Interferometer Configuration

Component	Attenuation	Power
Laser	0 dB	1.91 mW
Beam Splitter	-0.05 dB	1.89 mW
Fiber Light Coupler	-11 dB (2)	75 + 75 = 150 uW
1 m of Optical Fiber	-0.01 dB (2)	74.8 + 74.8 = 149.6 uW
Splice	-3 dB (2)	37.5 + 37.5 = 75 uW
Fused Coupler	-0.3 dB	70 uW
Detector	-0.2 dB	34 uW

Unfortunately, when the interferometer was completely assembled, the output power measured by the detector was not constant. However, with light only propagating in one arm of the interferometer, the output power was constant within ten percent. As soon as light propagated in both arms to complete the interferometer configuration, the output power was no longer constant. For example, with 30 uW of light inserted into each arm of the interferometer, the output power measured by the optical power meter would vary from 1 to 60 uW with a randomly changing frequency of a few hertz. It was observed that when the power from one output leg of the fused coupler was a maximum, the power from the other output leg of the fused coupler was a minimum. Combining the power from both legs yielded a more constant total output power value, which now varied to within twenty percent of its nominal value.

The problem of excessive noise in the fused coupler was initially attributed to be a defect in the fused coupler. To test this hypothesis, eight different samples of the same model of fused coupler were inserted into the interferometer; all the couplers produced identical results. Consequently, the GaAs fused coupler interferometer was then constructed to test whether the excessive noise was due to any particular component in the HeNe fused coupler interferometer. The different optical source wavelength requirement dictated that the GaAs fused coupler interferometer be constructed with a different optical source, optical fiber, and fused coupler compared to the HeNe fused coupler interferometer. However, the same excessive noise occurred in the GaAs fused coupler interferometer. As a final check of the equipment, Dr. Dale Sarrafzaeh of the American Research Corporation of Virginia, who is also researching the fiber optic magnetic field sensor concept, was contacted (36). Dr. Sarrafzaeh indicated that the same effect occurred in the interferometer that he constructed. This result indicates that the phenomena is not equipment dependent, but rather due to the inherent physics of the fused coupler Mach-Zehnder interferometer configuration.

Two possible explanations for the excessive noise were offered by two engineers in industry who are familiar with the fused coupler. Dr. Sarrafzaeh attributed the excessive noise to the fact that the interferometer was very sensitive to any environmental perturbations such as infinitesimal temperature variations and vibrations. In addition, Brad Sousa of York Technology, the firm that manufactures the HeNe fused couplers, suggested a different explanation (37). He stated that the excessive noise was due to interference between the different polarizations of light in each input of the coupler. Mr. Sousa stated that the excessive noise would not occur if the interferometer incorporated polarization-preserving, single-mode optical fiber and fused couplers. Due to the unavailability of the polarization-preserving components, this hypothesis was not tested.

Since the excessive noise in the fused couplers could not be eliminated, the HeNe fringe pattern interferometer was constructed. In this interferometer configuration, the output beams are recombined using bulk optics instead of a fused coupler. The HeNe fringe pattern interferometer, as shown in Figure IV.3, was produced. Reflections from the front and back side of the beam splitter caused a secondary fringe pattern to be formed. This secondary fringe pattern produced smaller light and dark bands within the primary fringe pattern.

The secondary fringe pattern could have been removed by two methods. The first technique is to use a beam splitter that was slightly wedged-shaped such that the secondary fringe pattern would form at an offset relative to the primary fringe pattern. This technique was not used since a wedged-shaped beam splitter was not available. A second option for correcting this aberration is to utilize a pellicle, or thin membrane beam splitter. By reducing the distance between the front and back surfaces of the beam splitter, the secondary fringe pattern is minimized. The pellicle method was rejected since the pellicle is very sensitive to air movement and vibration which would have added another noise source to the sensor.

The existing fringe pattern presented two sources of uncertainty in the sensor. First, the fringe pattern drifted with time. As the fringes swept by the slit, the output power measured by the radiometer varied from a maximum to minimum value with a randomly changing frequency of a few hertz. Second, each time a sensor arm was changed, a new fringe pattern had to be formed. The fringe pattern could not be exactly reproduced due to the slight curve and width of each line in the fringe pattern. As a consequence, the response of the sensor would be slightly different for each of the different fringe patterns because the slit would be sampling a different amount of each fringe pattern.

In summary, the three interferometer configurations were assembled. The GaAs fused coupler interferometer was only used to examine whether the excessive noise contributed from the fused coupler was dependent on the model of the fused coupler. The HeNe fringe pattern was assembled, but due to the uncertainty involved with the fringe pattern, was only used to in an attempt examine the sensor's response to DC magnetic fields. Although the HeNe fused coupler interferometer suffered from excessive noise associated with the fused coupler, this interferometer was used to measure the sensor's response to DC and AC magnetic fields.

Sensitivity Measurements

After the interferometers were assembled, the sensor's response for DC and AC magnetic fields was quantified. After describing the DC measurements, the verification of the measurement method for the AC sensor response is detailed. This section concludes with the results associated with the sensor's response to several magnetic field strengths when the sensor incorporated of the different sensor arms.

DC measurements. DC measurements were initially attempted with the PZT ring as the sensor arm in both the HeNe fused coupler interferometer and the fringe pattern interferometer. Both steady voltage levels and ramping voltages were applied to PZT ring. Due to the excessive noise from the fused coupler and the fringe pattern drift, the external stimulus could not be detected. With the magnetostrictive material sensor arms placed in both type of interferometers, the same negative result was observed. This result indicates that the fiber optic interferometers constructed for this research project are not appropriate for detecting DC magnetic fields.

AC measurements. Prior to measuring the response of the sensor to AC magnetic fields, the measurement method was validated using the PZT ring sensor arm. After the measurement method was confirmed, and the sensor's response with magnetostrictive coating sensor arms was verified to be from the magnetic field, the sensor's performance was evaluated for different sensor arms.

Due to the uncertainty involved with the fringe pattern interferometer, only the HeNe fused coupler interferometer was used to accomplish the AC measurements. The sensor was first characterized with the PZT ring as the sensor arm. Figure V.10 illustrates the averaged spectrum of the interferometer's output with no voltage applied to the PZT ring. Figure V.11 depicts the averaged spectrum of the sensor's output with 10 Vp-p signal applied to the PZT ring, and Figure V.12 shows the difference spectrum which is the result of subtracting the noise spectrum from the response spectrum. As shown in Figure V.12, the excitation signal at 25 Hz and its harmonics were easily detected. The harmonics are due to the fact that the PZT ring induced a phase change difference greater than one wavelength with respect to the optical source. Figure V.13 illustrates the sensor's difference spectrum for different voltage levels applied to the PZT ring. Figure V.14 depicts a plot of the amplitude of the interferometer's difference spectral response at 25 Hz for decreasing values of the externally applied voltage. Figure V.14 verifies that the amplitude of the difference spectrum at 25 Hz is a direct indication of the strength associated with an external stimulus. The change in the radius of the PZT ring as a function of the externally applied voltage signal level is given by (38:19):

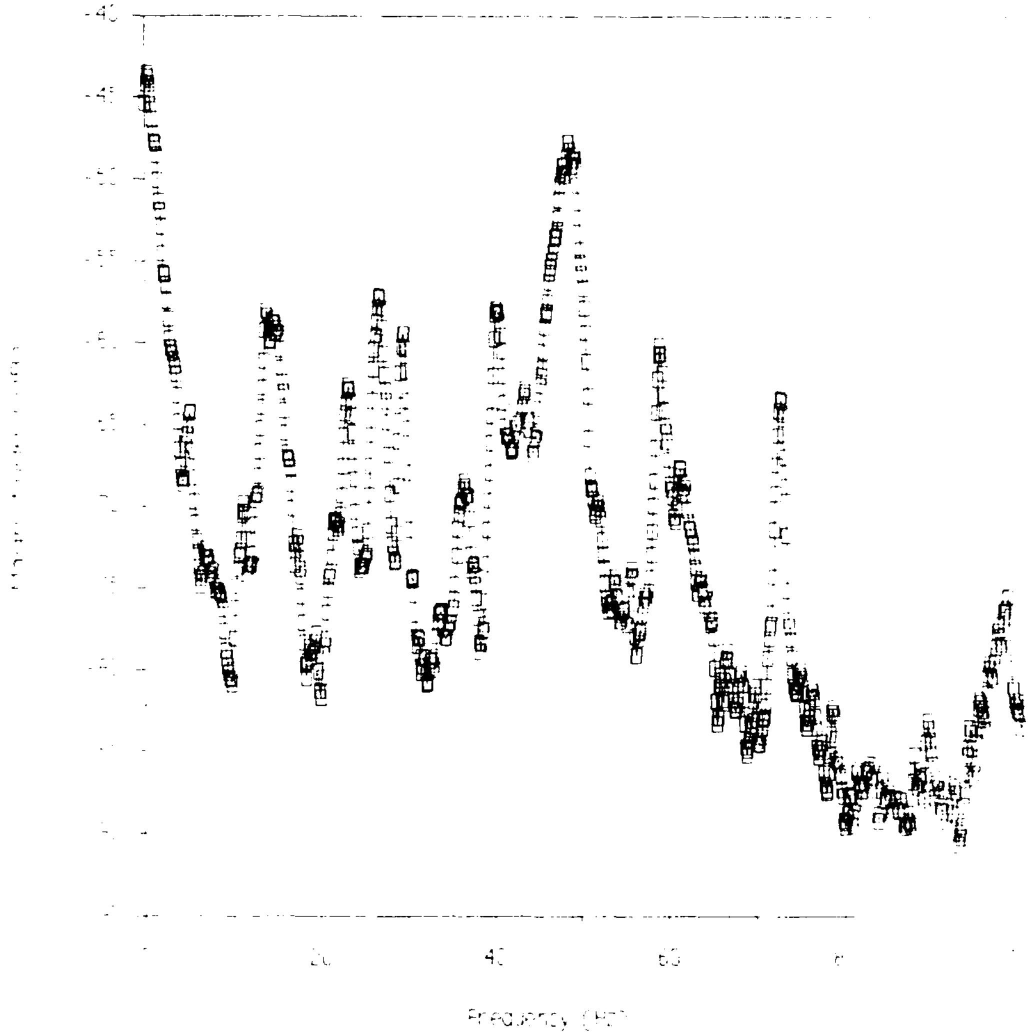

Figure V.10. Output Spectrum of the HeNe Fused Coupler Interferometer with the PZT Ring Sensor Arm but No Externally Applied Voltage Signal

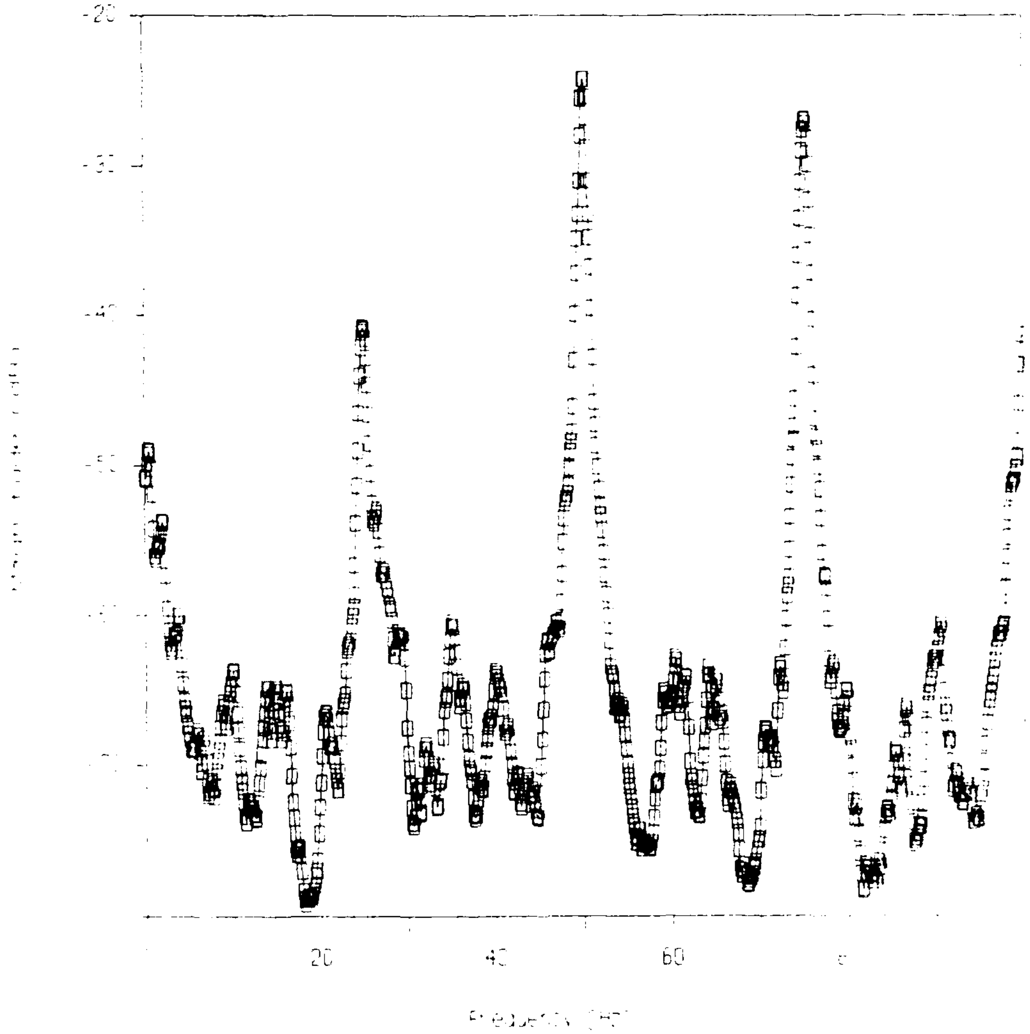

Figure V.11. Output Spectrum of the HeNe Fused Coupler Interferometer with the PZT Ring Sensor Arm and a 25 Hz, 10 Vp-p Externally Applied Voltage Signal

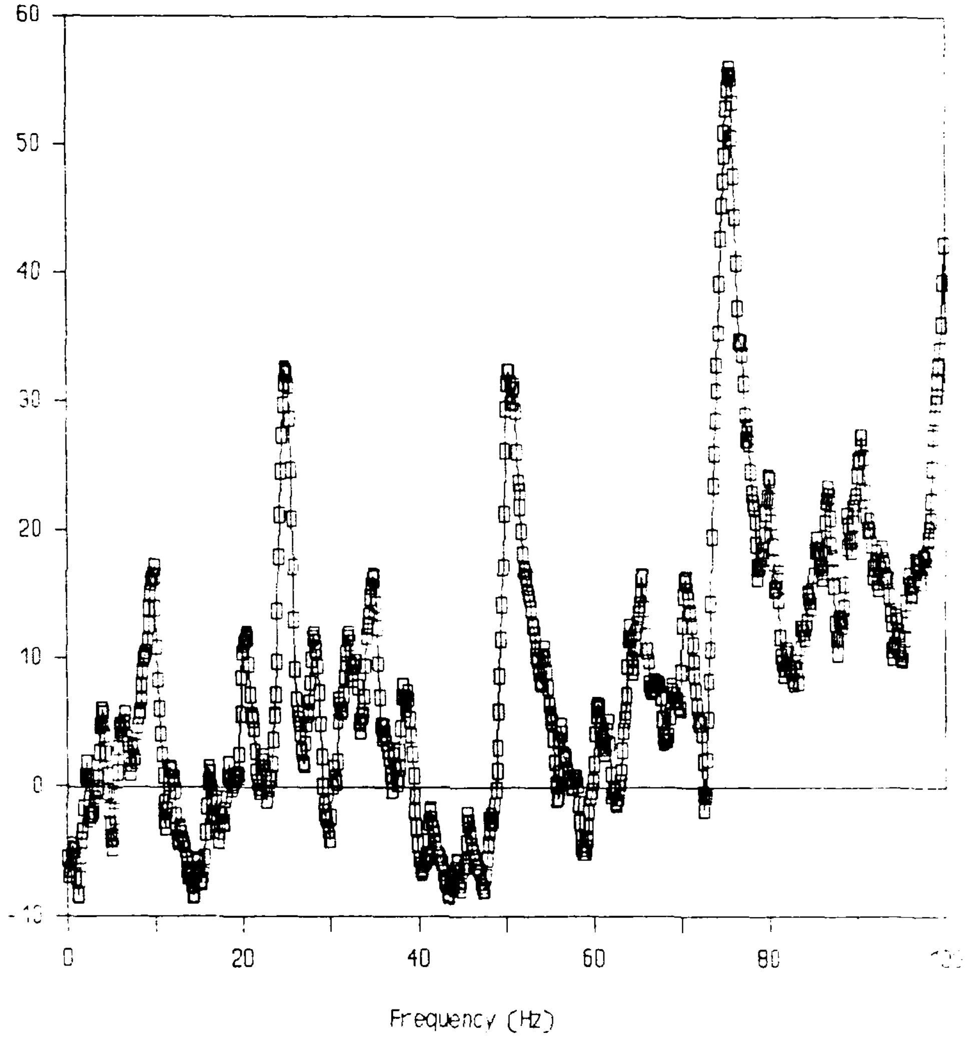

Figure V.12. HeNe Fused Coupler Interferometer's Output Noise Spectrum (Figure V.10) Subtracted from the Signal Spectrum (Figure V.11)

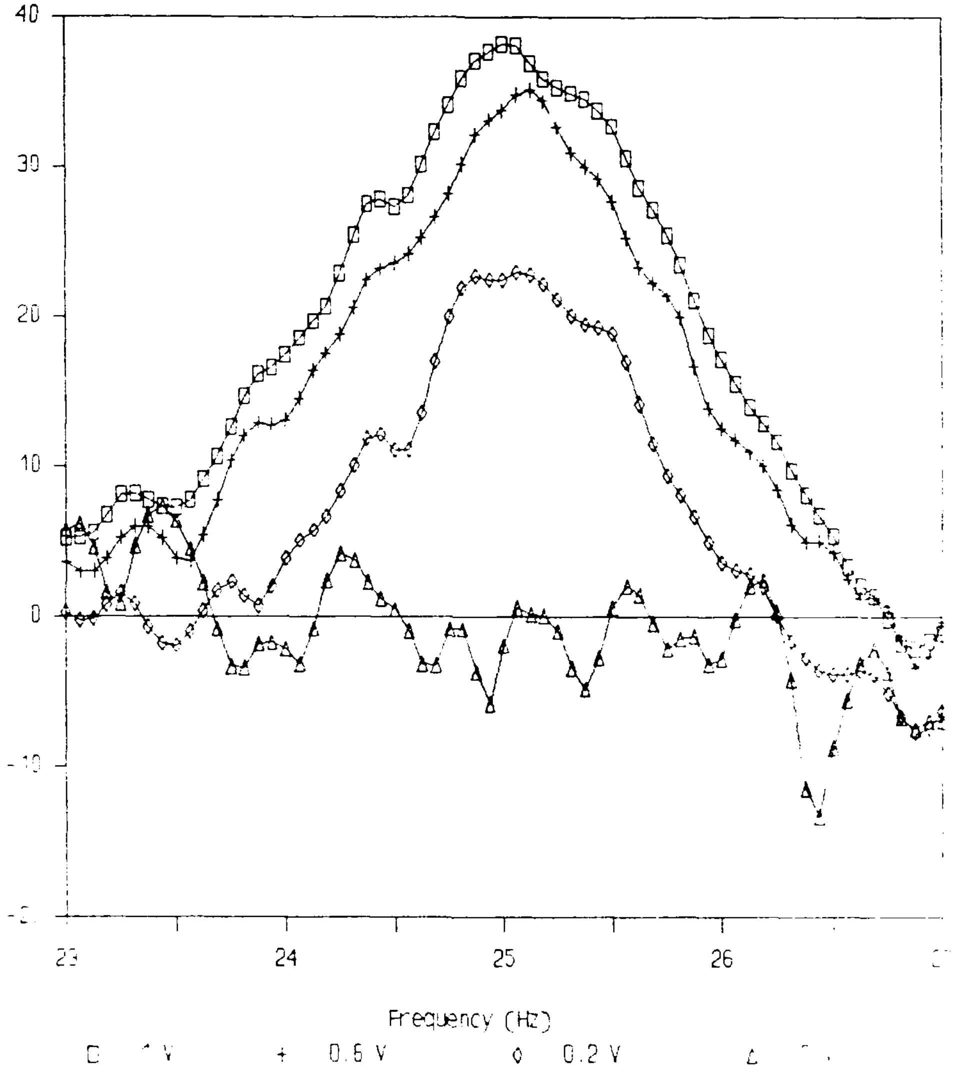

Figure V.13. HeNe Fused Coupler Interferometer Difference Response for Different Applied Voltages to the PZT Ring Sensor Arm

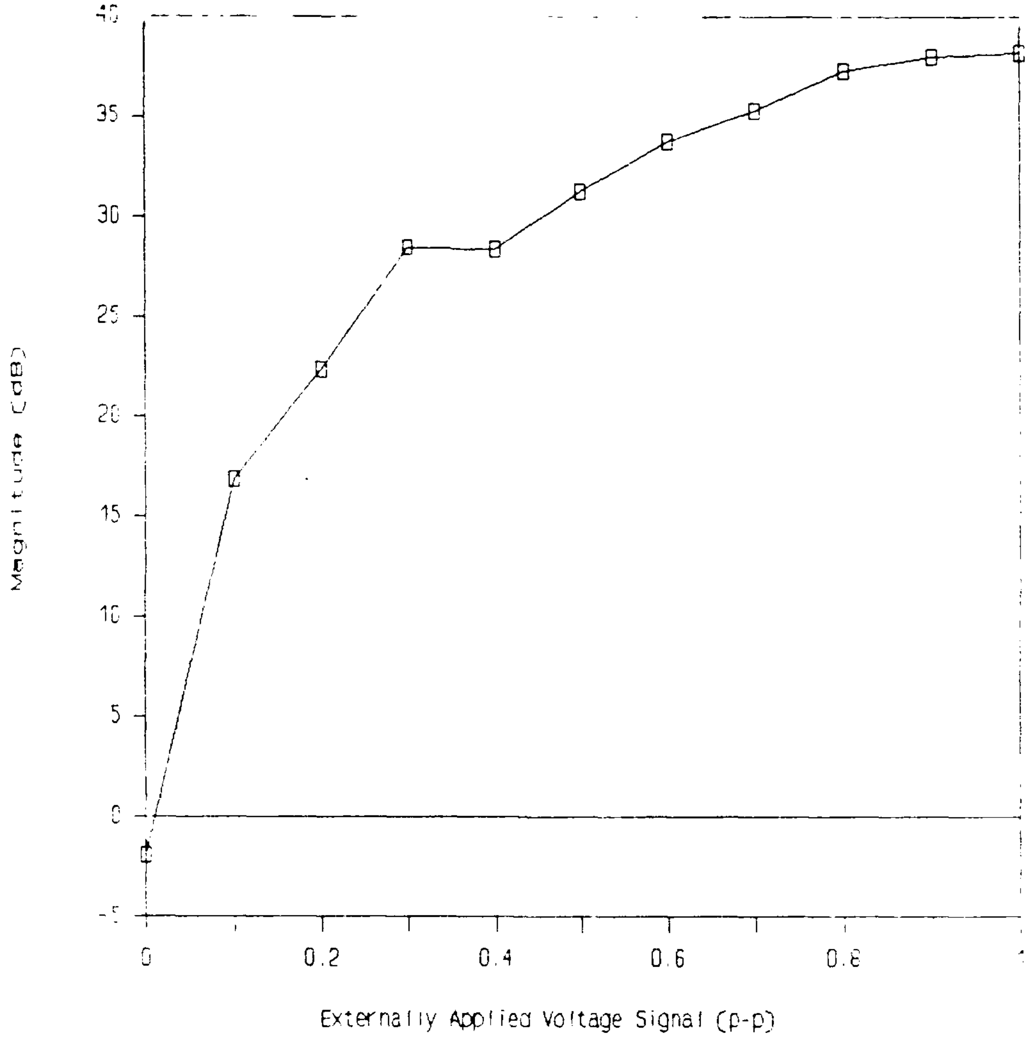

Figure V.14. HeNe Fused Coupler Interferometer Difference Spectral Component Magnitude at 25 Hz for Different Applied Voltage Signals to the PZT Ring Sensor Arm

$$\Delta r = d_{33}V \quad (112)$$

where Δr = change in radius of the ring

d_{33} = piezoelectric constant

V = applied voltage.

Therefore, the change in length of the PZT sensor arm is given by:

$$\Delta l = 2\pi\Delta r = 2\pi d_{33}V \quad (113).$$

Equation 113 states that the sensor's response in Figure V.14 is representative of a linear input response.

In addition to verifying the measurement scheme with the PZT ring sensor arm, the magnetostrictive material sensor's response was investigated to ensure that the response was due to the magnetostrictive effect in the sensor arm and not some other source. Two experiments were conducted to prove that the sensor was operating correctly.

The first experiment involved energizing the Helmholtz coil, which produced a sensor response similar to Figure V.11. When the laser light was only allowed to propagate in one arm at a time, the output signal at 25 Hz became indistinguishable from the noise, which indicated that the response was due to an interference effect and not some extraneous source, such as cross-talk between electrical cables.

The second experiment was implemented by replacing the sensor arm with an uncoated fiber and measuring the sensor's response. Initially, the sensor responded as depicted in Figure V.15. This response was attributed to the small vibrations

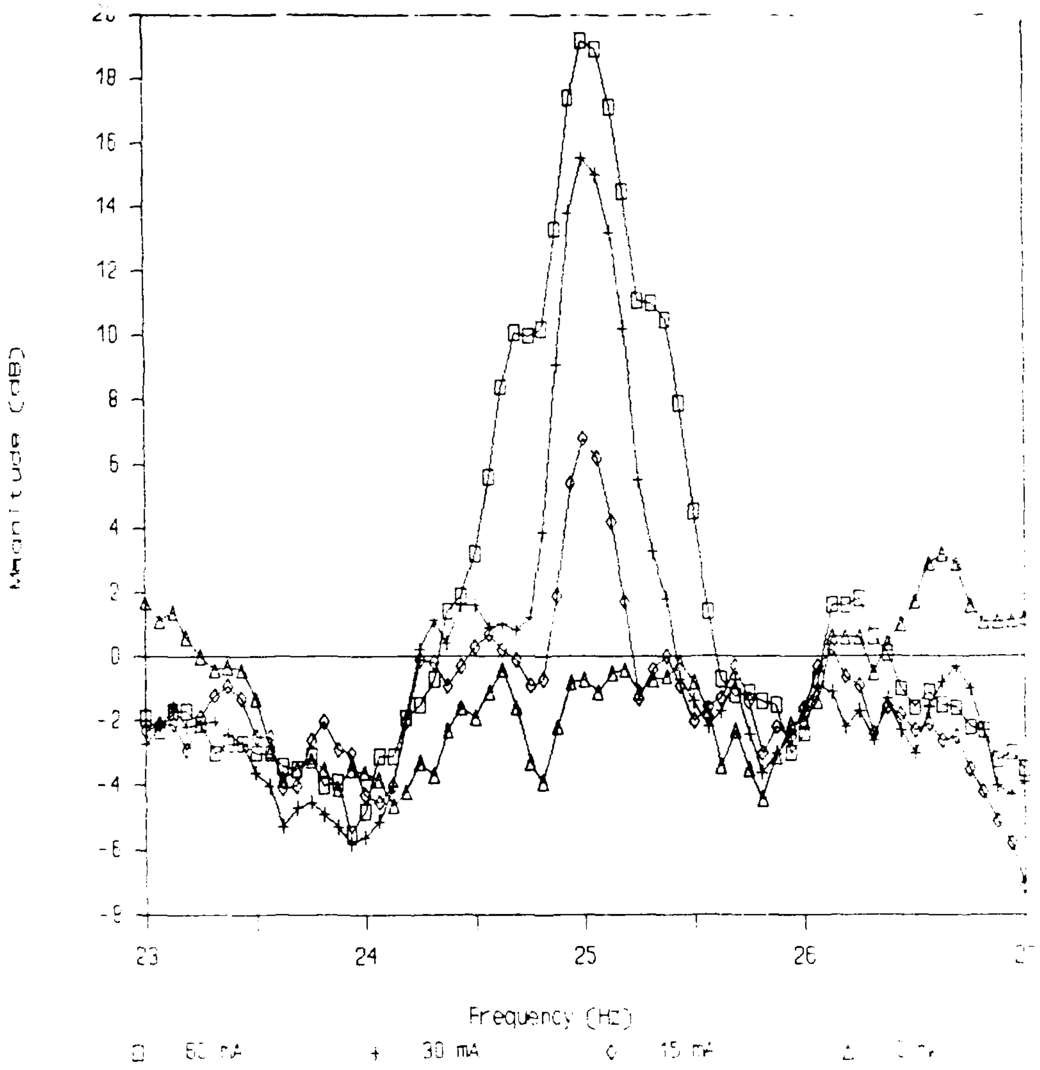

Figure V.15. HeNe Fused Coupler Interferometer Difference Response Spectrum Due to Low-level, 25 Hz Vibrations generated by the Helmholtz coil that are similar to transformer hum. Once the Helmholtz coil was suspended above the air table, the vibrational response disappeared. This experiment illustrated the extreme sensitivity of the sensor to environmental noise. Based on these two experiments, it was concluded that the sensor's response was due to the magnetostrictive effect of the sensor arm.

After the sensor's response was demonstrated to be directly related to the external magnetic field, the sensor's response was evaluated for both thin film coatings and bulk material configured sensor arms. Unfortunately, none of the sputtered thin film sensor arms produced a measurable response, even with the maximum AC magnetic field flux density of 11.8 G.

The failure of the sputtered fibers to respond to the AC magnetic field was attributed to the thinness and adhesion of the metal coating on the fiber not generating enough force to compress or stretch the fiber. The thickest sputtered film (9.5 um) coated a 125 um diameter silica fiber. Using equation 17 from the theory discussion of fiber optic cables in Chapter III, the force required to change the fiber's length is given by:

$$F = \frac{\Delta LEA}{L_o} \qquad (17)$$

where F = magnitude of the applied force

ΔL = change in length

L_o = initial length (0.1 m)

E = Young's modulus of the silica (6.89×10^{10} N/m^2)

A = cross sectional area of the fiber (1.23×10^{-8} m^2).

To induce a quarter wavelength equivalent change in the fiber's length (158 nm) requires the magnetostrictive material to exert a force of 1.34 mN. Although 1.34 mN is not a large force, it was more than the thin metal film coatings could generate.

Fortunately, the nickel rod generated a sufficient force level for the sensor to detect, which allowed a series of experiments to be conducted. Figure V.16 depicts an example of the difference response spectrum of the sensor with the as received nickel rod for several magnetic field levels. The first and second derivatives of the response curves provided no further information due to the noise in the signal.

Before attributing any changes in the sensor's response with different bulk sensor arms, a reproducibility study was conducted. The sensor's response was recorded after the same sensor arm was bonded three times. Figure V.17 shows that the sensor's response for each trial was similar for small AC magnetic flux densities, which indicates that changes in the sensor's response are not due to the bonding techniques used in the fabrication of the sensor arm.

After the effect of the fiber-nickel bonding technique was investigated, the influence associated with thermal and magnetic field processing of the nickel rod was determined. The nickel rod was first characterized as it was received, after thermal annealing, and after thermal annealing in the presence of an external magnetic field. Figure V.18 illustrates the results of that experiment. Thermal annealing without an external magnetic

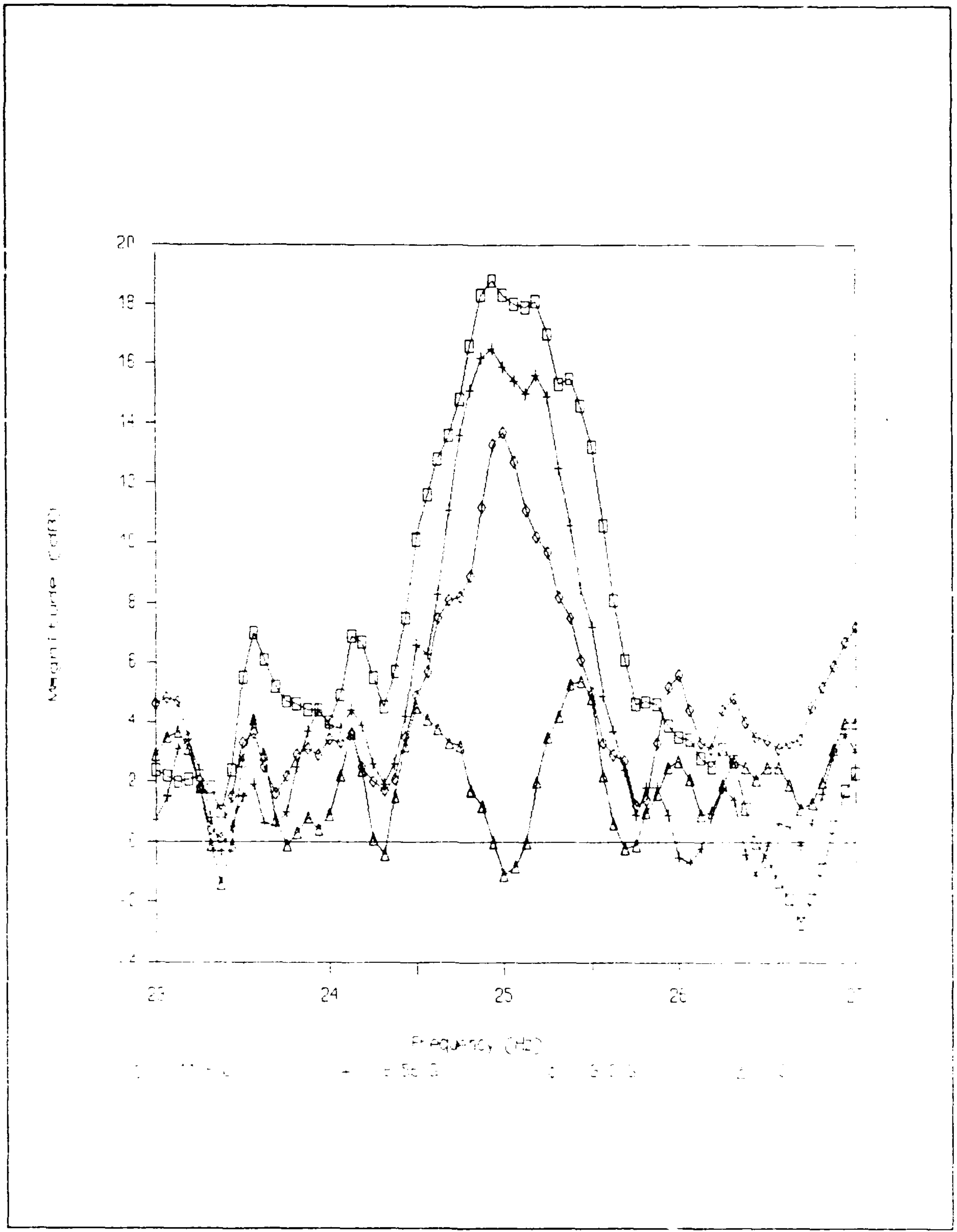

Figure V.16. Spectral Response of the Sensor with the as Received Bulk Nickel Sensor Arm for Several Magnetic Field Levels

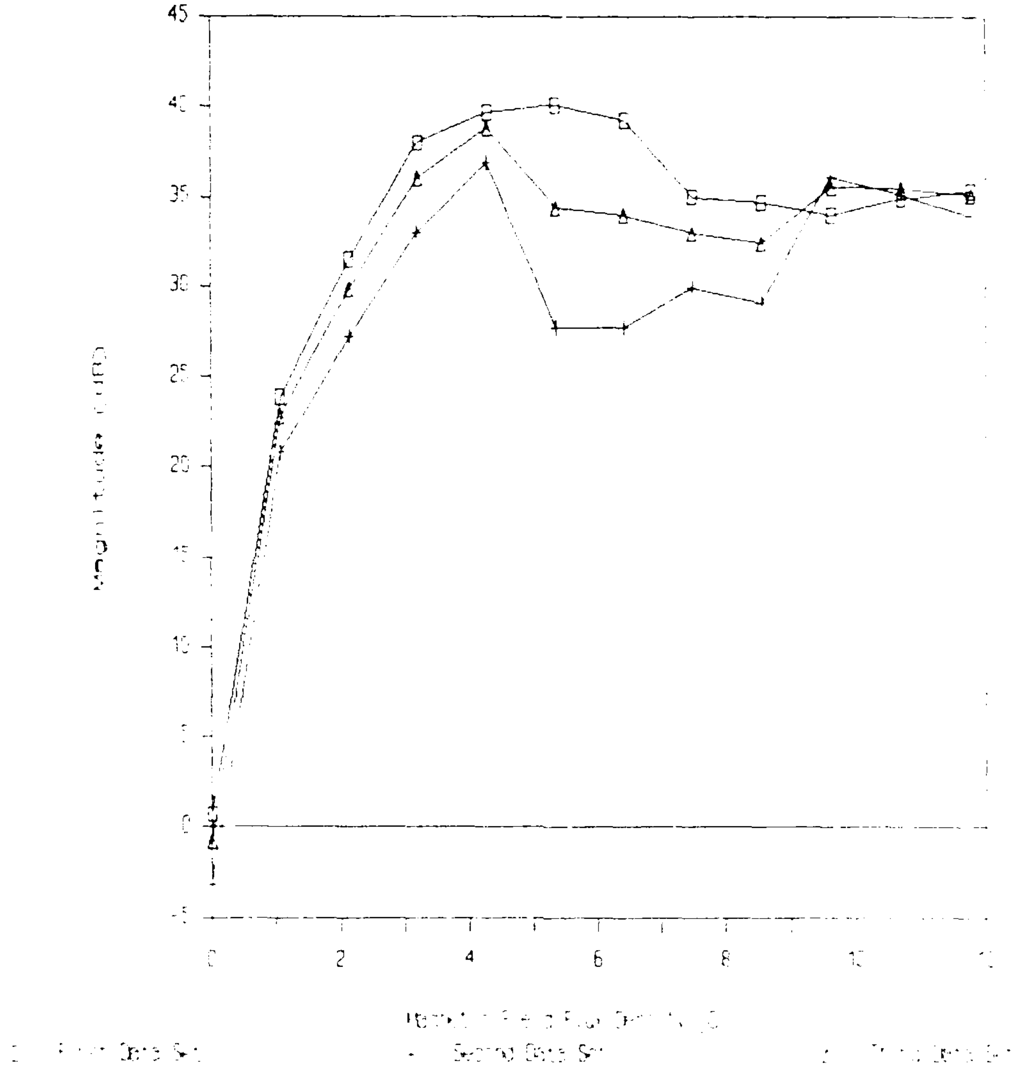

Figure V.17. Spectral Response of the Sensor for Three Similarly Fabricated Nickel Sensor Arms

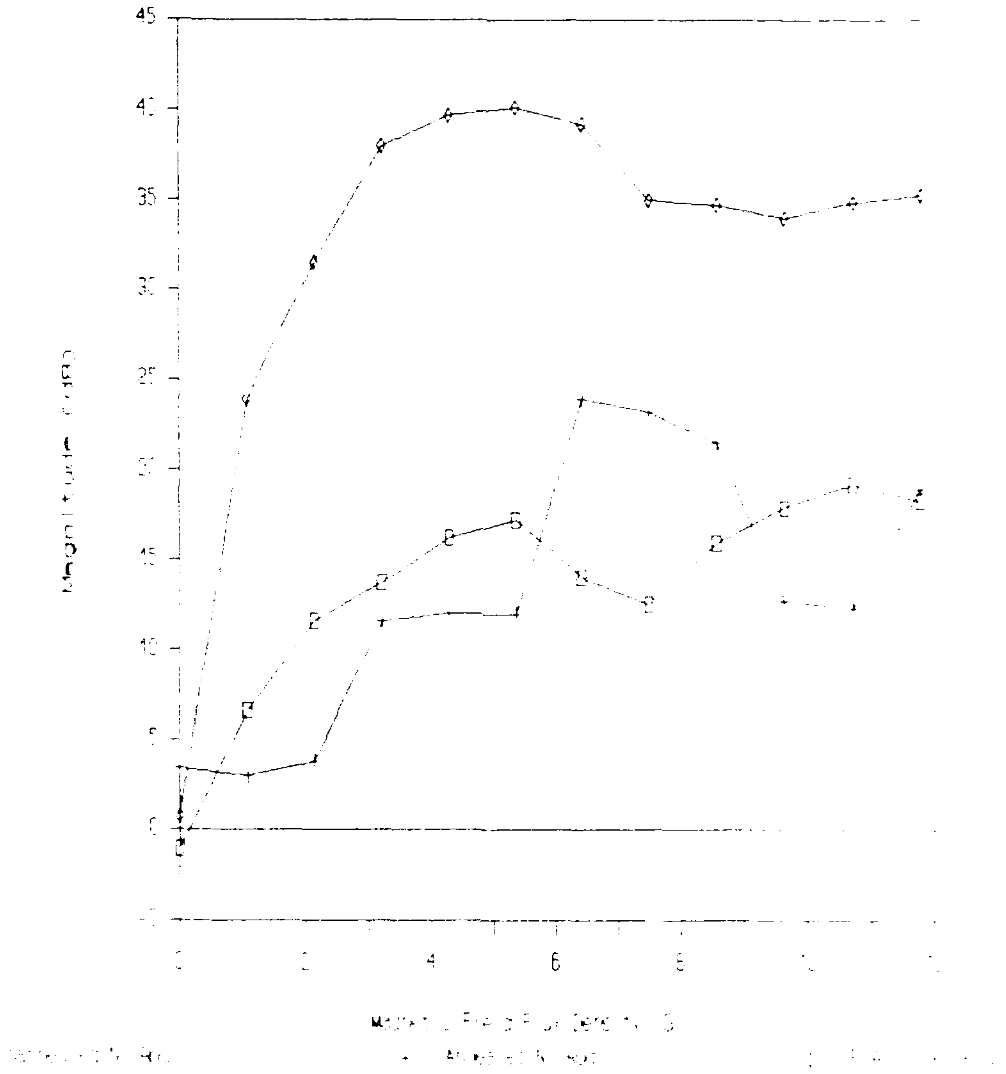

Figure V.18. Effect of Thermal Annealing with and without an External Magnetic Field on the Sensor's Performance field in addition to the earth's ambient magnetic field did not have an effect on the performance of the sensor. This result was not unexpected since the rod was heated in its formation. However, when the rod was cooled in the presence of a 1000 G external magnetic field flux density, the magnetic domains partially aligned with this external field, which resulted in an improved magnetostriction effect.

The next experiment was conducted to determine experimentally the effect of the optical fiber's geometry on the sensor's response. The two sensor arms evaluated in this experiment were the thinned fiber sensor arm and the sensor arm incorporating three lengths of fiber. Figure V.19 illustrates the results of this experiment. Thinning the fiber did not affect the sensor's performance. When the bulk nickel rod experienced magnetostriction, it must have generated enough force to compress the fiber regardless of the fiber's cross-sectional area. The sensor's performance improved with longer optical fiber lengths as the theory predicted.

Figures V.18 and V.19 provide information concerning the sensor's response and measurement methods. For small magnetic field flux densities (< 4 G), the sensor's response with the magnetostrictive sensor arms was similar to the sensor's performance with the PZT ring sensor arm. This fact indicates that the magnetostrictive effect was approximately linear for small magnetic flux densities. This situation corresponds to operating on a small linear region on the fractional change in

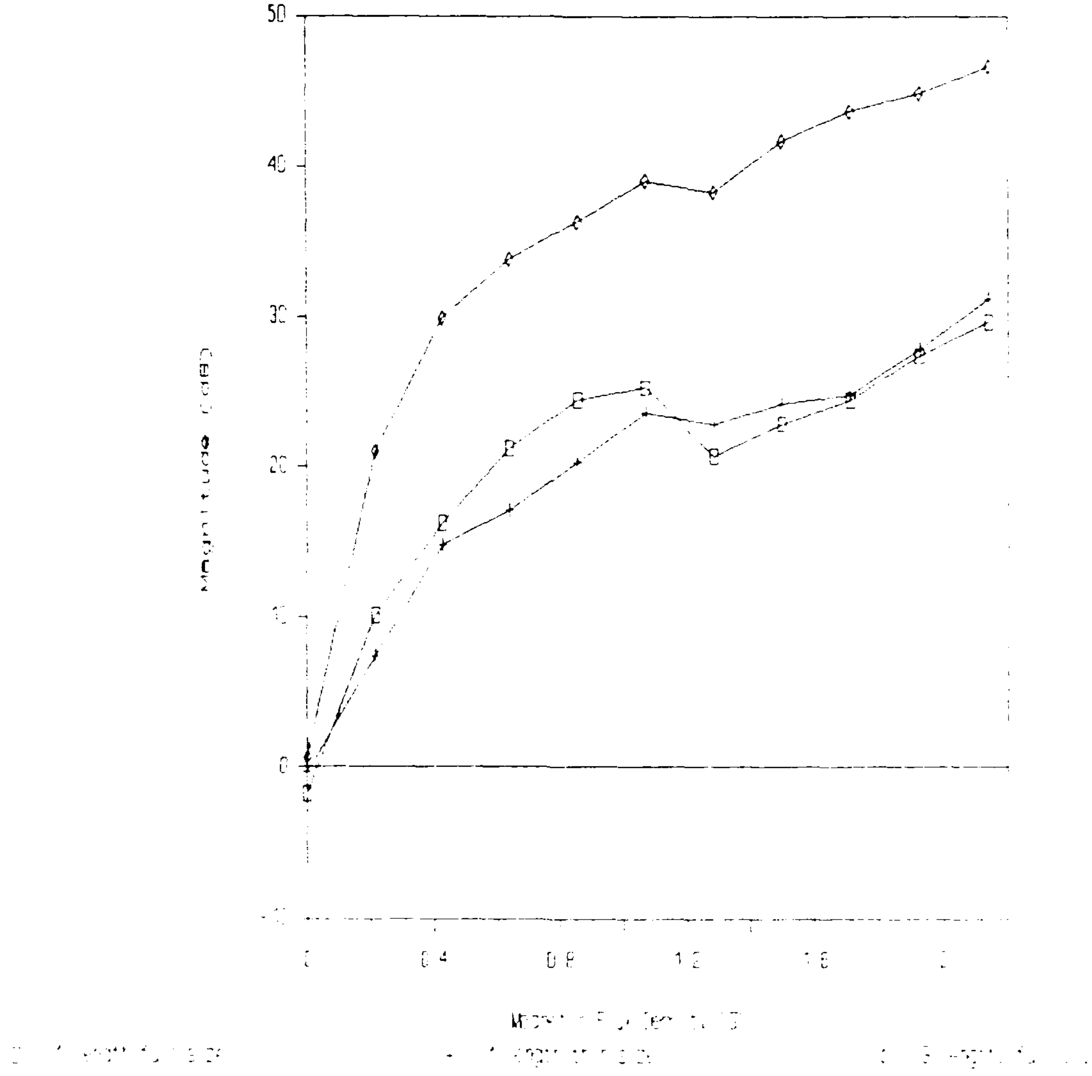

Figure V.19. Effect of the Optical Fiber's Geometry on the Sensor's Response length vs magnetic flux density curve (Figure III.9). Figures V.18 and V.19 also indicate that the sensor's response saturates above 4 G. From Figure III.9, this saturation behavior is attributed to the measurement scheme, and not the magnetostrictive effect. Figure V.17 also illustrates a flaw in the measurement scheme. Each set of data corresponding to a curve in Figures V.17, V.18, and V.19 should have been recorded several times and averaged to yield a more representative curve for the test conditions. This observation was not made until the nickel rod had been irrevocably processed, which prevented additional data from being gathered.

Sensor Optimization

The final experiments conducted involved improving the sensor's performance without altering the fiber or the magnetostrictive material. Instead, the effect of a DC bias magnetic field flux density on the sensor's response to an AC magnetic field was investigated. The sensor arm used for this experiment contained three lengths of optical fiber. Figure V.20 shows the effect of different DC bias magnetic flux densities on the sensor's response for an AC magnetic field flux density of 0.2 G. Although the curve is not smooth, the trend indicates that the sensor is more sensitive under the influence of a larger DC bias magnetic field flux density. From the data, it cannot be determined if there is an optimum value of DC bias magnetic flux density. If a larger DC magnetic flux density could have been generated, the peak sensitivity in the vicinity of 10 G might

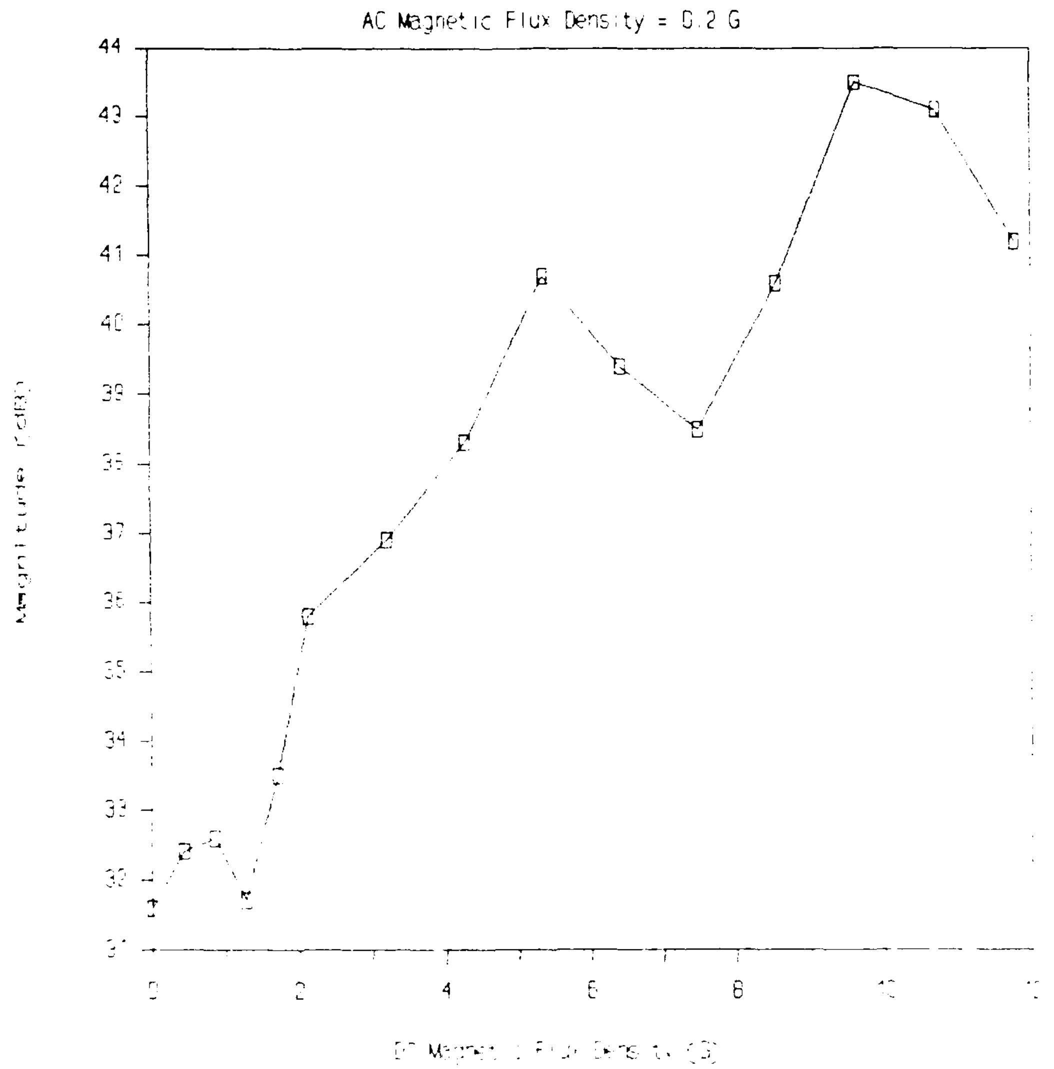

Figure V.20. Effect of a DC Bias Magnetic Flux Density on the Sensor's Response for a Given AC Magnetic Flux Density have been identified as a local or absolute maximum.

The final sensor characterization experiment involved determining the smallest AC magnetic field flux density that could be detected. The optimum configuration of the sensor utilized the nickel rod sensor arm that had been thermally annealed in the presence of an external magnetic field (1000 G) with three lengths of optical fiber attached to it. A DC bias magnetic field flux density of 0.428 G was then applied to the sensor arm. With only 10 turns of the Helmholtz coil energized (instead of 250), this situation represented the largest DC magnetic field flux density that could be generated. Only 10 turns of the Helmholtz coil were energized to produce a small AC magnetic flux density. Figure V.21 depicts the sensor's response for decreasing values of the AC magnetic field flux density. The smallest AC magnetic field flux density that could be generated and observed was 10 mG, which was 5 dB above the average noise level.

In summary, this research effort was successful in characterizing certain aspects of the sensor's performance. Although the sensor did not detect DC or AC magnetic fields with RF sputtered sensor arms, the sensor did detect AC magnetic fields using a bulk nickel sensor arm configuration. Using this one bulk sensor arm, it was determined that the sensor was more sensitive when the magnetostrictive material was thermally annealed in the presence of a magnetic field. The sensor was also more sensitive with longer lengths of optical fibers bonded

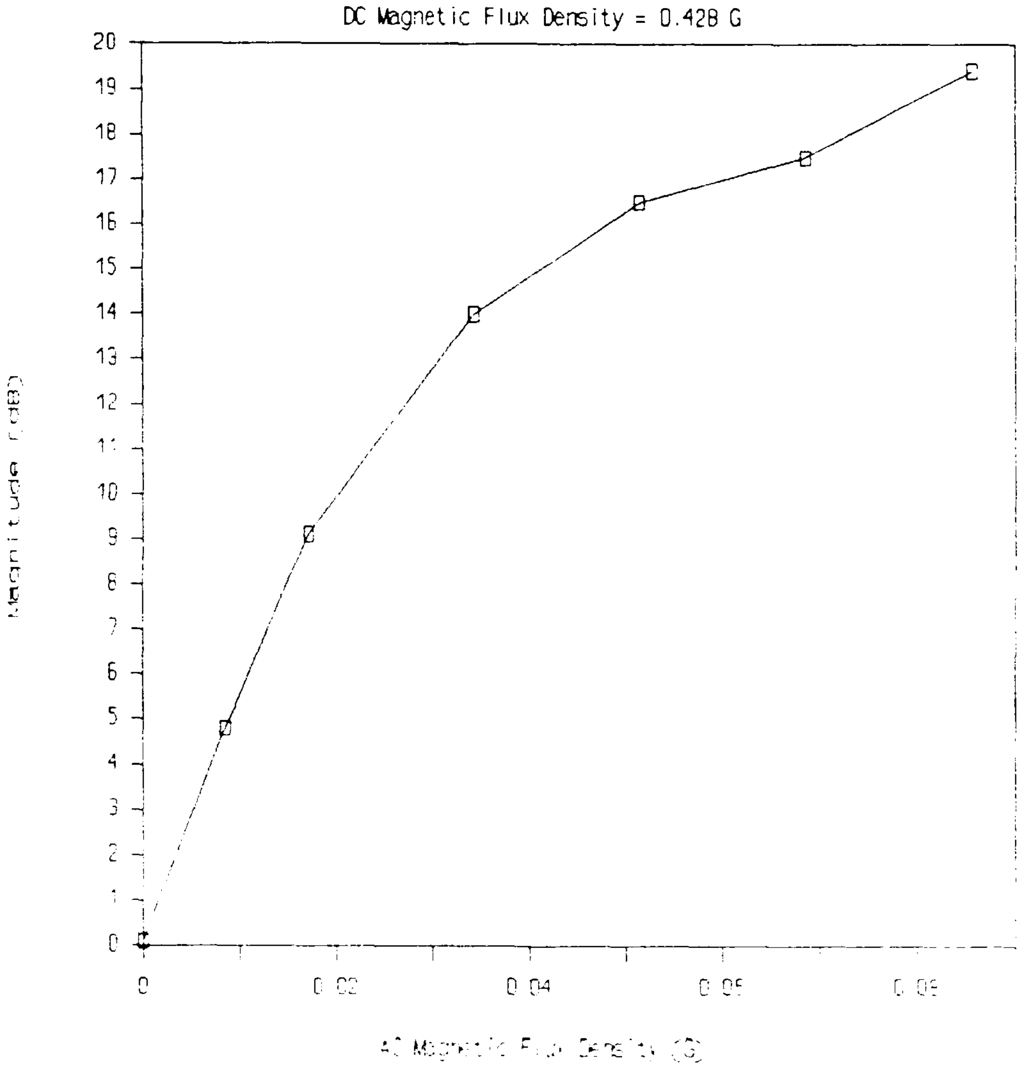

Figure V.21. Sensor's Response for the Optimum Conditions to the sensor arm and when the AC magnetic field to be detected was superimposed on a DC magnetic field flux density. Thinning the fiber and thermally annealing the nickel rod did not affect sensor performance. A complete summary of the research project is included in the next Chapter.

VI. Conclusion and Recommendations

This Chapter summarizes the results of this research project and provides recommendations for further study of the sensor.

Conclusion

A magnetostrictive fiber optic interferometric sensor was fabricated and evaluated. To evaluate the sensor, a Helmholtz coil was designed, fabricated, and calibrated. A measurement scheme was then developed to determine the sensor's sensitivity. Once the sensor's response could be quantified, the sensor's performance was evaluated for different sensor arms. Finally, the sensor's effectiveness was optimized using a DC bias magnetic field flux density.

The goal of this research project was to investigate a magnetic field sensor that has the potential to detect a pilot's biomagnetic fields. A Helmholtz coil was used to simulate the biomagnetic fields. This Helmholtz coil was designed to generate a uniform magnetic field flux density whose magnitude could be varied. To verify the Helmholtz coil's performance, it was calibrated with a Hall effect magnetometer, and was found to generate magnetic field flux densities to within fifteen percent of the theoretically predicted values.

Once the source of the magnetic field was characterized, three different interferometer configurations were assembled, and a measurement method was developed and validated. After each interferometer configuration was fabricated, its output optical power level and stability were examined. The fused coupler, which was used to recombine the light propagating in each arm of the interferometer, contributed the largest source of noise. A piezoelectric ring sensor arm was used to verify that, as the signal strength at 25 Hz decreased, the amplitude of the frequency component at 25 Hz of the sensor's response also decreased.

Sensor sensitivity measurements were then made with various sensor arms. No DC magnetic field flux density measurements could be made due to the noise contributed by the fused coupler. However, the sensor did detect a 25 Hz AC magnetic field using sensor arms composed of a bulk nickel rod. Sensors consisting of RF sputtered thin films of cobalt, iron, and nickel on the optical fiber did not detect an AC magnetic field flux density whose magnitude approached 12 G. The failure of the thin films was attributed to fact that the thin film could not generate sufficient force to change the fiber's length a detectable amount.

Experiments were also conducted to determine the effect on the sensor's response as a result of processing the nickel rod and altering the optical fiber. Thermally annealing the nickel rod at 758° C did not change the sensor's performance. However, as theoretically predicted, thermally annealing the nickel rod in the presence of an external magnetic field (1000 G) did produce improved sensor sensitivity. Thinning the optical fiber that was bonded to the nickel rod did not affect the sensor's response because the nickel rod produced sufficient force to stretch the fiber whether the fiber was full size or reduced. However, a three fold increase in the length of the fiber bonded to the nickel rod improved the sensor's sensitivity.

To optimize the sensor's performance, a DC bias magnetic field flux density was generated in addition to the AC magnetic field flux density that was to be detected. Increasing the DC bias magnetic field flux density improved the sensor's response for a particular AC magnetic field flux density level. To determine the ultimate sensitivity of the sensor, a DC bias magnetic field flux density of 0.4 G was applied to the nickel rod that had been thermally annealed in the presence of an external magnetic field, and it was bonded to a length of fiber that was three times the nominal length of fiber (10 cm). With this optimal configuration, the sensor detected an AC magnetic field of 10 mG at 25 Hz.

Recommendations

This research effort demonstrated that a magnetostrictive fiber optic interferometer can detect low-level magnetic fields, and it also provided some insight into the behavior of the sensor. However, much of the sensor's characteristics are still unknown. Additional work needs to be performed to optimize the sensor so that it may one day achieve its theoretical sensitivity. Specifically, the following research topics should be investigated:

1. The magnetostrictive material needs to be more

thoroughly understood. A model needs to be developed that can predict the amount of force generated by a magnetostrictive material. This model should include the following material parameters: type (including alloys), structure (crystalline, polycrystalline, and amorphous), thickness, and geometry.

2. The fused coupler, which provided the largest noise source, should be investigated. A model should be developed to explain the interaction of the fields in the device. This model could then be used to vary the design of the fused coupler to minimize the noise.

3. Another approach to reduce the noise from the fused coupler involves evaluating polarization-preserving optical fibers and fused couplers.

4. Alternate methods of depositing metal (such as electroless plating) on the optical fibers should be evaluated. The combination of two or more metal deposition methods may produce adequate quality films of sufficient thickness.

5. Different cooling procedures for the fabrication of thermally annealed thin film coated optical fibers should be explored to prevent the fibers from breaking. A microprocessor controlled oven should be used to carefully control the temperature processing profile of the fiber.

6. Bulk magnetostrictive materials should also be furtner investigated. Different materials (such as met-glass alloys) should be evaluated. The method of bonding the fiber to the bulk material should be refined.

7. The method of determining sensor sensitivity should be reexamined. The use of different signal analysis equipment, such as a lock-in amplifier, may provide an improved signal-to-noise ratio.

8. To improve the sensor's sensitivity, the length of the fiber in contact with the magnetostrictive material should be increased.

9. To examine the response of the sensor with thin film sensor arms, a larger magnetic field may be required. To generate a larger magnetic field, a Helmholtz coil should be fabricated with more turns of wire.

10. The noise in the sensor could be reduced by minimizing the separation between the sensor arm and reference arm. One method to accomplish this that should be investigated is to use two fused couplers and bond the sensor and reference arms together.

11. To further reduce the sensor's noise, an improved test chamber should be constructed. This test chamber should shield the optical fiber components from the ambient magnetic field, thermal variations, and vibrations.

12. The possibility of a fabricating a single-mode metallic glass waveguide should be investigated. This device would remove the fiber-magnetostrictive material bonding problems by allowing the waveguide to interact directly with the magnetic field that is to be detected.

Appendix A

Magnetic Units

This appendix reviews the units of magnetism that are relevant to the discussion of fiber optic magnetic field sensors (10:57). For this thesis, an important quantity is the magnetic field flux density, (B) which is measured in units of Gauss. This figure of merit is directly proportional to magnetic field (H) since $B = \mu H$, where μ is the permeability of the material. For this application, the permeability of the medium inside the Helmholtz coil is approximated to be that of free space ($\mu=\mu_o\mu_r=\mu_o(1)=4\pi \times 10^{-7}Hm^{-1}$). Table A describes the relationship between these two quantities in the various system of units.

Table A. Magnetic Unit Conversion

	System of Units		
Quantity	cgs	SI	other
Magnetic Flux Density, B	1 Gauss(G)	10^{-4} Tesla(T) 10^{-4} Weber/m^2	10^{-5} Gamma
Magnetic Field, H	1 Oersted(Oe)	79.6 A/m	

Appendix B

MATHCAD Template Used for Helmholtz coil off-axis magnetic flux density calculation

This is a MATHCAD template which was used to calculate the magnetic flux density for a Helmholtz coil arrangement using a numerical summation technique applied to the differential form of the Biot-Savart law.

An explanation of the Biot-Savart law and a figure (Figure III.3) illustrating the geometry of the problem is included in the text of this thesis (Chapter III).

In the text, an expression for the magnetic flux density along the axis between the two coils was derived in closed form. In order to calculate the off-axis magnetic flux density, a numerical summation technique was used.

$a := 0.105$	Coil radius (m).
$y := 0, 0.001 .. 0.02$	Off axis positions (m).
$N := 250$	Number of turns.
$\mu := 4 \cdot \pi \cdot 10^{-7}$	Permeability (H/m).
$I := 0.2$	Current (A).
$z := 0.0525$	Axial position between coils (m).
$n := 32$	Number of coil divisions.
$d\theta := 2 \cdot \frac{\pi}{n}$	Rotation increment.
$\theta := 0, d\theta .. 2 \cdot \pi - d\theta$	Range of rotation values.
$r1(\theta) := \begin{bmatrix} a \cdot \cos(\theta) \\ a \cdot \sin(\theta) \\ 0 \end{bmatrix}$	Vector describing the position on the circumference of a coil.
$r2(y) := \begin{bmatrix} 0 \\ y \\ z \end{bmatrix}$	Vector describing the position of interest between coils.
$dl(\theta) := \begin{bmatrix} -a \cdot d\theta \cdot \sin(\theta) \\ a \cdot d\theta \cdot \cos(\theta) \\ 0 \end{bmatrix}$	Vector describing the incremtal position on the cicumference of a coil.

$r(y,\theta) := r2(y) - r1(\theta)$

Vector measured from a point on the circumference of a coil to a point of interest.

$R(y,\theta) := \sqrt{r(y,\theta)\cdot r(y,\theta)}$

Magnitude of the previous vector.

$$dB(y,\theta) := N\cdot\mu\cdot I\cdot 2\cdot\frac{dl(\theta)\times r(y,\theta)}{R(y,\theta)^{3}}$$

Incremental flux density contribution from one position on a coil. The factor of "2" is for the two coils.

$$B(y) := \frac{10^{4}}{4\cdot\pi}\cdot\sum_{\theta} dB(y,\theta)$$

Vector describing the sum of all flux density contributions from all points on the circumference of a coil.

$$B(0) = \begin{bmatrix} 0 \\ 0 \\ 4.281792 \end{bmatrix}$$

Vector expression for the magnetic flux density at the center of the axis. Closed form solution = 4.28179 G.

$BB(y) := \sqrt{B(y)\cdot B(y)}$

Scaled magnitude of the above vector.

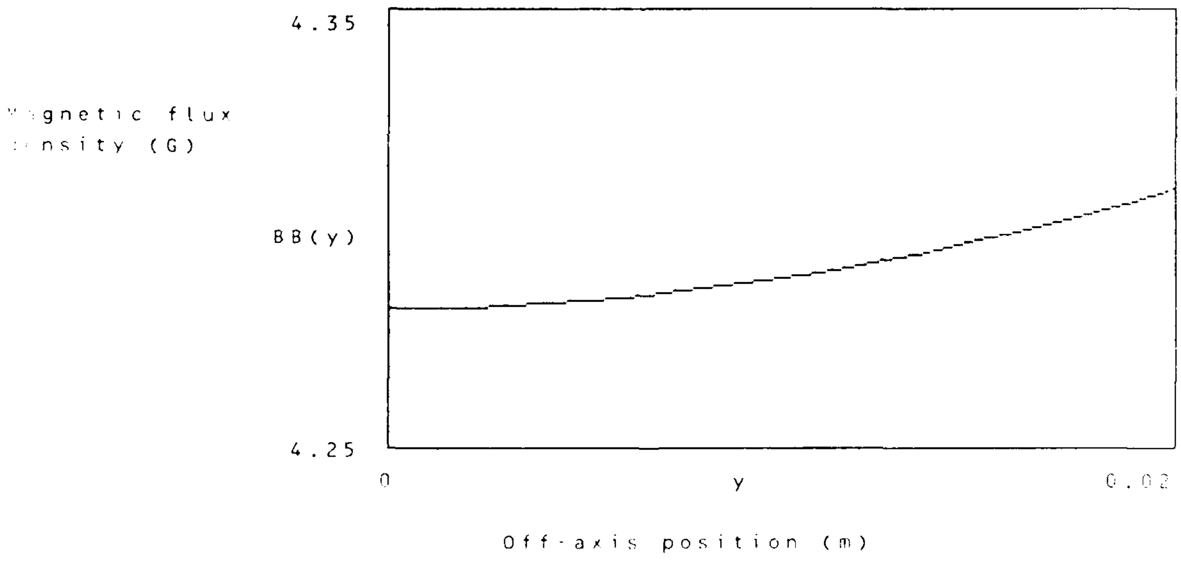

Vector expressions for the magnetic flux density for the off-axis points:

$$B(0) = \begin{bmatrix} 0 \\ 0 \\ 4.281792 \end{bmatrix}$$

$$B(.002) = \begin{bmatrix} 0 \\ 0.048949 \\ 4.281792 \end{bmatrix}$$

$$B(.004) = \begin{bmatrix} 0 \\ 0.097983 \\ 4.281788 \end{bmatrix}$$

$$B(.006) = \begin{bmatrix} 0 \\ 0.147188 \\ 4.281772 \end{bmatrix}$$

$$B(.008) = \begin{bmatrix} 0 \\ 0.196649 \\ 4.281729 \end{bmatrix}$$

$$B(.010) = \begin{bmatrix} 0 \\ 0.246451 \\ 4.281638 \end{bmatrix}$$

$$B(.012) = \begin{bmatrix} 0 \\ 0.296682 \\ 4.281473 \end{bmatrix}$$

$$B(.014) = \begin{bmatrix} 0 \\ 0.347426 \\ 4.281198 \end{bmatrix}$$

$$B(.016) = \begin{bmatrix} 0 \\ 0.398772 \\ 4.280773 \end{bmatrix}$$

$$B(.018) = \begin{bmatrix} 0 \\ 0.450805 \\ 4.280151 \end{bmatrix}$$

$$B(.020) = \begin{bmatrix} 0 \\ 0.503613 \\ 4.279276 \end{bmatrix}$$

Magnitude of the magnetic flux density vector:

y	BB(y)
0	4.281792
0.001	4.281862
0.002	4.282071
0.003	4.282421
0.004	4.282909
0.005	4.283536
0.006	4.284301
0.007	4.285204
0.008	4.286243
0.009	4.287417
0.01	4.288725
0.011	4.290167
0.012	4.291739
0.013	4.293442
0.014	4.295272
0.015	4.297227
0.016	4.299307
0.017	4.301507
0.018	4.303826
0.019	4.306261
0.02	4.308808

Appendix C

BASIC Computer Programs Used to Calculate the Electric and Magnetic Fields in an Optical Fiber

```
10    '*****************************************************
20    '
30    '
40    '
50    ' FILENAME: FIELD
60    '
70    ' THIS PROGRAM WAS USED TO CALCULATE THE ELECTRIC AND
80    ' MAGNETIC FIELDS PROPAGATING IN THE FIBER OPTIC CABLE USED
90    ' USED IN THIS RESEARCH PROJECT. THE FIELDS ARE CALCULATED
100   ' FOR A FIXED ANGLE OF 0 WITH VARIABLE DISTANCE FROM THE
110   ' OPTICAL AXIS.  NUMERICAL SERIES APPROXIMATIONS FOR THE
120   ' BESSEL FUNCTIONS AND MODIFIED BESSEL FUNCTIONS ARE USED.
130    ' THESE NUMERICAL APPROXIMATIONS ARE ONLY VALID WHEN THEIR
140   ' ARGUMENT IS LESS THAN OR EQUAL TO 3.
150   '
160   ' ****************************************************
170   '
180   '           CONSTANTS DEFINED
190   '
1000 V = 1.88                         'NORMALIZED FREQUENCY
1010 U=1.48                           'NORMALIZED TRANSVERSE PHASE
1012 '                                 CONSTANT IN THE CORE
1020 W=(V^2-U^2)^.5                   'NORMALIZED TRANSVERSE PHASE
1022 '                                 CONSTANT IN THE CLADDING
1030 A=1.75*10^-6                     'CORE RADIUS
1040 L=.6328*10^-6                    'OPTICAL SOURCE WAVELENGTH
1050 N1=1.461                         'CORE INDEX OF REFRACTION
1060 N2=1.457                         'CLADDING INDEX OF REFRACTION
1062 EO=8.85E-12                      'FREE SPACE PERMITTIVITY
1064 E1=N1^2*EO                       'CORE PERMITTIVITY
1066 E2=N2^2*EO                       'CLADDING PERMITTIVITY
1070 C=3*10^8                         'SPEED OF LIGHT IN VACUUM
1080 UO=1260*10^-9                    'PERMEABILITY
1090 PI=3.14159                       'PI
1100  K=2*PI/L                             'WAVE NUMBER OF OPTICAL
SOURCE
1110 B=((K*N1)^2-(U/A)^2)^.5         'PHASE CONSTANT
1120 F=2*PI*C/L                        'FREQUENCY OF OPTICAL SOURCE
(RADS)
1122 '
1124 '*****************************************************
1126 '
1128 '        A,B,C,AND D CONSTANTS CALCULATION
1130 '
1190 X=U:GOSUB 3000                   'J0,J1,J2,J1' CALCULATED
1195 X=W:GOSUB 3036                   'K0,K1,K2,K1' CALCULATED
```

```
1200 AA=1                                 'NORMALIZE CONSTANTS
1210 CC=J1/K1                             'C CALCULATED
1240 BB = B/(F*UO)*(U^(-2)+W^(-2))/(J1P/(U*J1)+K1P/(W*K1))
1245 '                                    'B CALCULATED
1246 DD = BB*J1/K1                        'D CALCULATED
1247 '*********************************************************
1248 '
1249 '           CALCULATION FOR FIELDS IN CORE
1250 '
1251 LPRINT " "
1252 LPRINT " "
1253  LPRINT "                ************************      CORE
*****************************"
1254 LPRINT "                    R          EX         EY         EZ
  HX         HY         HZ"
1255 FOR R = 0 TO 1.1 STEP .1             'SCALED DISTANCE FROM OPTICAL
AXIS
1257 R = R +.0000001                      'OFFSET FOR SINGULARITY
1260 X = U*R                              'ARGUMENT FOR J AND K
1262 GOSUB 3000                           'J0,J1,J2,J1' CALCULATED
1265 RS = R*A                             'ACTUAL DISTANCE FROM OPTICAL
AXIS
1266 T=T*PI/180                           'ANGLE
1270 ER = (-B*J1P/(U/A)+BB*F*UO*J1/((U/A)^2*RS))*SIN(T)
1280 ET = (-B*J1/((U/A)^2*RS)+BB*F*UO*J1P/(U/A))*COS(T)
1282 HR = (F*E1*J1/((U/A)^2*RS)-BB*B*J1P/(U/A))*COS(T)
1284 HT = (-F*E1*J1P/(U/A)+BB*B*J1/((U/A)^2*RS))*SIN(T)
1290 EX = ER*COS(T)-ET*SIN(T)
1300 EY = ER*SIN(T)+ET*COS(T)
1304 EZ=J1*SIN(T)
1310 HX = HR*COS(T)-HT*SIN(T)
1320 HY = HR*SIN(T)+HT*COS(T)
1322 HZ=BB*J1*COS(T)
1323 '
1324 '*********************************************************
1325 '
1326 '          CALCULATION FOR FIELDS IN CLADDING
1327 '
1328 LPRINT TAB(10);
1330 LPRINT USING "+##.##### ";R;EX,EY,EZ,HX,HY,HZ
1332 NEXT R
1334  LPRINT "              ************************      CLADDING
***************************"
1336 LPRINT "                    R          EX         EY         EZ
  HX         HY         HZ"
1338 FOR R = 1 TO 3.1 STEP .1
1339 R = R + .0000001
1350 X=W*R
1351 GOSUB 3000
1352 GOSUB 3036
1360 ERC = (CC*B*K1P/(W/A)-DD*F*UO*K1/((W/A)^2*RS))*SIN(T)
1370 ETC = (CC*B*K1/((W/A)^2*RS)-DD*F*UO*K1P/(W/A))*COS(T)
```

```
1380 EXC = ERC*COS(T)-ETC*SIN(T)
1390 EYC = ERC*SIN(T)+ETC*COS(T)
1392 EZC = CC*K1*SIN(T)
1400 HRC = (-CC*F*E2*K1/((W/A)^2*RS)+DD*B*K1P/(W/A))*COS(T)
1410 HTC = (CC*F*E2*K1P/(W/A)-DD*B*K1/((W/A)^2*RS))*SIN(T)
1412 HYC = HRC*SIN(T)+HTC*COS(T)
1414 HXC = HRC*COS(T)-HTC*SIN(T)
1416 HZC = DD*K1*COS(T)
1418 LPRINT TAB(10);
1420 LPRINT USING "+##.##### ";R;EXC;EYC;EZC;HXC;HYC;HZC
1425 NEXT R
1430 END
2990 '
2992 '*********************************************************
2993 '
2994 '  SUBROUTINES THAT CALCULATE J0,J1,J2,J1',K0,K1,K2,K1'
2995 '
3                     0                    0                    0
J0=1-2.2499997#*(X/3)^2+1.2656208#*(X/3)^4-.3163866*(X/3)^6+.0444
479*(X/3)^8-.0039444*(X/3)^10+.00021*(X/3)^12
3                     0                    1                    0
J1=X*(.5-.56249985#*(X/3)^2+.21093573#*(X/3)^4-3.954289E-02*(X/3)
^6+4.43319E-03*(X/3)^8-3.1761E-04*(X/3)^10+1.109E-05*(X/3)^12)
3020 J2=2*J1/X-J0
3030 J1P=.5*(J0-J2)
3032 'RETURN
3036 IF X>2 THEN 4000
3                     0                    3                    7
I0=1+3.5156229#*(X/3.75)^2+3.0899424#*(X/3.75)^4+1.2067492#*(X/3.
75)^6+.2659732*(X/3.75)^8+.0360768*(X/3.75)^10+.0045813*(X/3.75)^
12
3                     0                    3                    8
I1=.5+.87890594#*(X/3.75)^2+.51498869#*(X/3.75)^4+.15084934#*(X/3
.75)^6+2.658733E-02*(X/3.75)^8+3.01532E-03*(X/3.75)^10+3.24111E-0
4*(X/3.75)^12
3039 I1=I1*X
3                     0                    4                    0
K0=-LOG(X/2)*I0-.57721566#+.4227842*(X/2)^2+.23069756#*(X/2)^4+.0
348859*(X/2)^6+2.62698E-03*(X/2)^8+.0001075*(X/2)^10+.0000074*(X/
2)^12
3                     0                    4                    5
K1=X*LOG(X/2)*I1+1+.15443144#*(X/2)^2-.67278579#*(X/2)^4-.1815689
7#*(X/2)^6-1.919402E-02*(X/2)^8-1.10404E-03*(X/2)^10
3050 K1=X^(-1)*K1
3060 K2=2*K1/X+K0
3070 K1P=-.5*(K0+K2)
3080 IF X<=2 THEN 4070
4                     0                    0                    0
K0=1.25331414#-.07832*(2/X)+2.189568E-02*(2/X)^3-1.062446E-02*(X/
2)^3+5.87872E-03*(2/X)^4
4010 K0=X^(-.5)*EXP(-X)*K0
4                     0                    2                    0
```

```
K1=1.25331414#+.23498619#*(2/X)-.0365562*(2/X) 2+1.504268E-02*(2/
X)^3-7.80353E-03*(2/X)^4
4030 K1=X^(-.5)*EXP(-X)*K1
4040 K2=2*K1/X+K0
4050 K1P=-.5*(K0+K2)
4070 RETURN
10   '*********************************************************
20   '
30   '
40   '
50   ' FILENAME: UCALC
60   '
70   ' THIS PROGRAM WAS USED TO CALCULATE THE NORMALIZED
80   ' TRANSVERSE PHASE CONSTANT IN THE CORE (U) IN THE
90   ' OPTICAL FIBER USED IN THIS RESEARCH PROJECT.
100  ' THE PROGRAM USES NUMERICAL SERIES APPROXIMATIONS
110  ' FOR THE BESSEL FUNCTIONS AND MODIFIED
120  ' BESSEL FUNCTIONS.  THESE NUMERICAL APPROXIMATIONS ARE ONLY
130  ' VALID WHEN THEIR ARGUMENT IS LESS THAN OR EQUAL TO 3.
140  ' TO SOLVE FOR U REQUIRES SOLVING A TRANSCENDENTAL EQUATION.
150  ' THE EQUATION WAS SOLVED BY SOLVING EACH SIDE FOR VARIOUS
160  ' VALUES OF U UNTIL THE DIFFERENCE WAS MINIMIZED.
170  '
180  '*********************************************************
190  '
200  '
1000 A = 0                            'START OF U VALUE RANGE
1010 B = 1.8                          'END OF U VALUE RANGE
1020 S = .1                           'STEP SIZE IN U VALUE RANGE
1022 LPRINT " "
1023 LPRINT " "
1025 OLDDIFF = 1E+30                  'INITIAL DIFFERENCE
1027 V = 1.87                         'NORMALIZED FREQUENCY
1028 LPRINT TAB(10);
1029 LPRINT "  U     DIFFERENCE"
1030 FOR U = A TO B STEP S            'LOOP USED TO CALCULATE
1035                                  'EACH SIDE FOR A DIFFERENCE
1040 X = U + .0000001                 'OFFSET FOR SINGULARITY
1050 GOSUB 3000                       'CALCULATE J0,J1,K0,K1
1060 LEFT = J0/(X*J1)                 'LEFT SIDE OF EQUATION
1070 X = (V^2-U^2)^.5                 'SCALED VARIABLE
1080 GOSUB 3000                       'CALCULATE J0,J1,K0,K1
1090 RIGHT = K0/(X*K1)                'RIGHT SIDE OF EQUATION
1100 NEWDIFF = ABS(LEFT-RIGHT)        'LEFT - RIGHT
1102 LPRINT TAB(10);
1105 LPRINT USING "#.###  ";U;
1107 LPRINT USING "##.##^^^^";NEWDIFF
1110 IF NEWDIFF>OLDDIFF THEN 1200     'CONTINUE LOOP UNTIL
1112                                  'LEFT - RIGHT MINIMIZED
1115 OLDDIFF=NEWDIFF                  'RESET DIFFERENCE
1120 NEXT U
1200 IF S <= .001 THEN 1300           'CHECK STEP SIZE
```

```
1210 A = U-2*S                        'NEW INITIAL U RANGE
1220 B = U                            'NEW FINAL U RANGE
1230 S = S/10                         'NEW STEP SIZE
1235 OLDDIFF = OLDDIFF + 1
1240 GOTO 1030
1300 END
2990 '
2992 '**********************************************************
2993 '
2994 '
2995 '
2996 '  SUBROUTINES USED TO CALCULATE J0,J1,K0,K1
2998 '
3                     0                     0                    0
J0=1-2.2499997#*(X/3)^2+1.2656208#*(X/3)^4-.3163866*(X/3)^6+.0444
479*(X/3)^8-.0039444*(X/3)^10+.00021*(X/3)^12
3                     0                     1                    0
J1=X*(.5-.56249985#*(X/3)^2+.21093573#*(X/3)^4-3.954289E-02*(X/3)
^6+4.43319E-03*(X/3)^8-3.1761E-04*(X/3)^10+1.109E-05*(X/3)^12)
3020 J2=2*J1/X-J0
3030 J1P=.5*(J0-J2)
3032 'RETURN
3036 IF X>2 THEN 4000
3                     0                     3                    7
I0=1+3.5156229#*(X/3.75)^2+3.0899424#*(X/3.75)^4+1.2067492#*(X/3.
75)^6+.2659732*(X/3.75)^8+.0360768*(X/3.75)^10+.0045813*(X/3.75)^
12
3                     0                     3                    8
I1=.5+.87890594#*(X/3.75)^2+.51498869#*(X/3.75)^4+.15084934#*(X/3
.75)^6+2.658733E-02*(X/3.75)^8+3.01532E-03*(X/3.75)^10+3.24111E-0
4*(X/3.75)^12
3039 I1=I1*X
3                     0                     4                    0
K0=-LOG(X/2)*I0-.57721566#+.4227842*(X/2)^2+.23069756#*(X/2)^4+.0
348859*(X/2)^6+2.62698E-03*(X/2)^8+.0001075*(X/2)^10+.0000074*(X/
2)^12
3                     0                     4                    5
K1=X*LOG(X/2)*I1+1+.15443144#*(X/2)^2-.67278579#*(X/2)^4-.1815689
7#*(X/2)^6-1.919402E-02*(X/2)^8-1.10404E-03*(X/2)^10
3050 K1=X^(-1)*K1
3060 K2=2*K1/X+K0
3070 K1P=-.5*(K0+K2)
3080 IF X<=2 THEN 4070
4                     0                     0                    0
K0=1.25331414#-.07832*(2/X)+2.189568E-02*(2/X)^3-1.062446E-02*(X/
2)^3+5.87872E-03*(2/X)^4
4010 K0=X^(-.5)*EXP(-X)*K0
4                     0                     2                    0
K1=1.25331414#+.23498619#*(2/X)-.0365562*(2/X)^2+1.504268E-02*(2/
X)^3-7.80353E-03*(2/X)^4
4030 K1=X^(-.5)*EXP(-X)*K1
4040 K2=2*K1/X+K0
```

```
4050 K1P=-.5*(K0+K2)
4070 RETURN
```

```
*********************     CORE     ***************************
    R        EX       EY       EZ       HX       HY       HZ
+0.0000  +0.0000 -17.1938  +0.0000  +0.0666  +0.0000  -0.0000
+0.1000  +0.0000 -17.0996  +0.0000  +0.0662  +0.0000  -0.0003
+0.2000  +0.0000 -16.8185  +0.0000  +0.0651  +0.0000  -0.0006
+0.3000  +0.0000 -16.3551  +0.0000  +0.0633  +0.0000  -0.0008
+0.4000  +0.0000 -15.7170  +0.0000  +0.0609  +0.0000  -0.0011
+0.5000  +0.0000 -14.9147  +0.0000  +0.0578  +0.0000  -0.0013
+0.6000  +0.0000 -13.9613  +0.0000  +0.0541  +0.0000  -0.0016
+0.7000  +0.0000 -12.8721  +0.0000  +0.0499  +0.0000  -0.0018
+0.8000  +0.0000 -11.6649  +0.0000  +0.0452  +0.0000  -0.0019
+0.9000  +0.0000 -10.3592  +0.0000  +0.0402  +0.0000  -0.0021
+1.0000  +0.0000  -8.9757  +0.0000  +0.0348  +0.0000  -0.0022
*********************     CLADDING     ************************
    R        EX       EY       EZ       HX       HY       HZ
+1.0000  +0.0000  -8.9758  +0.0000  +0.0346  +0.0000  -0.0022
+1.1000  +0.0000  -6.8640  +0.0000  +0.0264  +0.0000  -0.0018
+1.2000  +0.0000  -5.3338  +0.0000  +0.0205  +0.0000  -0.0015
+1.3000  +0.0000  -4.2002  +0.0000  +0.0162  +0.0000  -0.0013
+1.4000  +0.0000  -3.3450  +0.0000  +0.0129  +0.0000  -0.0011
+1.5000  +0.0000  -2.6895  +0.0000  +0.0104  +0.0000  -0.0009
+1.6000  +0.0000  -2.1804  +0.0000  +0.0084  +0.0000  -0.0008
+1.7000  +0.0000  -1.7803  +0.0000  +0.0069  +0.0000  -0.0007
+1.8000  +0.0000  -1.4605  +0.0000  +0.0056  +0.0000  -0.0006
+1.9000  +0.0000  -1.1972  +0.0000  +0.0046  +0.0000  -0.0005
+2.0000  +0.0000  -0.9861  +0.0000  +0.0038  +0.0000  -0.0004
+2.1000  +0.0000  -0.8156  +0.0000  +0.0031  +0.0000  -0.0004
+2.2000  +0.0000  -0.6769  +0.0000  +0.0026  +0.0000  -0.0003
+2.3000  +0.0000  -0.5635  +0.0000  +0.0022  +0.0000  -0.0003
+2.4000  +0.0000  -0.4702  +0.0000  +0.0018  +0.0000  -0.0002
+2.5000  +0.0000  -0.3932  +0.0000  +0.0015  +0.0000  -0.0002
+2.6000  +0.0000  -0.3293  +0.0000  +0.0013  +0.0000  -0.0002
+2.7000  +0.0000  -0.2762  +0.0000  +0.0011  +0.0000  -0.0002
+2.8000  +0.0000  -0.2318  +0.0000  +0.0009  +0.0000  -0.0001
+2.9000  +0.0000  -0.1947  +0.0000  +0.0007  +0.0000  -0.0001
+3.0000  +0.0000  -0.1635  +0.0000  +0.0006  +0.0000  -0.0001
```

```
  U      DIFFERENCE
0.000    2.00E+14
0.100    1.99E+02
0.200    4.93E+01
0.300    2.15E+01
0.400    1.18E+01
0.500    7.30E+00
0.600    4.85E+00
0.700    3.37E+00
0.800    2.40E+00
0.900    1.73E+00
1.000    1.25E+00
1.100    8.79E-01
1.200    5.90E-01
1.300    3.54E-01
1.400    1.51E-01
1.500    3.32E-02
1.600    2.17E-01
1.400    1.51E-01
1.410    1.32E-01
1.420    1.13E-01
1.430    9.48E-02
1.440    7.62E-02
1.450    5.78E-02
1.460    3.94E-02
1.470    2.12E-02
1.480    3.03E-03
1.490    1.51E-02
1.470    2.12E-02
1.471    1.94E-02
1.472    1.76E-02
1.473    1.57E-02
1.474    1.39E-02
1.475    1.21E-02
1.476    1.03E-02
1.477    8.48E-03
1.478    6.66E-03
1.479    4.85E-03
1.480    3.03E-03
1.481    1.22E-03
1.482    5.96E-04
1.483    2.41E-03
```

Appendix D

BASIC Computer Programs Used to Record Data

```
10   '**********************************************************
20   '
30   '
40   '
50   ' FILENAME: BKDISP
60   '
70   ' THIS PROGRAM WAS USED TO TAKE DATA FROM THE BREUL & KJAER
80   ' TYPE 2032 SIGNAL ANALYZER VIA A METROBYTE IEEE 488
90   ' CARD AND A ZENITH 248 COMPUTER.  THE PROGRAM USES
100  ' SUBROUTINES TO SEND COMMANDS TO AND RECEIVE DATA FROM THE
110  ' B&K 2032.  THE PROGRAM INITIALIZES BOTH THE IEEE CARD AND
120  ' THE B&K 2032.  AFTER INITIALIZATION, THE PROGRAM PRESENTS
130  ' A MENU WITH CHOICES OF EXAMINING OR RECORDING THE TIME OR
140  ' SPECTRAL INFORMATION IN THE EXCITATION OR RESPONSE.
150  '
160  '**********************************************************
170  '
180  '                INITIALIZATION
190  '
1000 OPTION BASE 1                'ARRAYS BEGIN WITH ELEMENT 1
1010 GOSUB 9000                   'INITIALIZE THE INTERFACE
1020 GOSUB 9100                   'REMOTE
1100 O$ = "ED DS,0"               'INPUT DATA SOURCE
1110 GOSUB 9300
1120 O$ = "EM MM,1"               'SPECTRUM AVERGING ZERO PAD
1130 GOSUB 9300
1170 O$ = "EM AF,0"               'CH A FILTER OFF
1180 GOSUB 9300
1190 O$ = "EM AU,0"               'VOLT UNITS FOR CH A
1210 GOSUB 9300
1240 O$ = "EM BF,0"               'CH B FILTER OFF
1250 GOSUB 9300
1260 O$ = "EM BU,0"               'VOLT UNITS FOR CH B
1270 GOSUB 9300
1280 O$ = "EM MC,2"               'DUAL MEASUREMENT CHANNEL
1290 GOSUB 9300
1490 '
1492 '**********************************************************
1493 '
1494 '                 THE MENU IS DISPLAYED
1496 '
1498 '
1500 CLS
1510 PRINT "ENTER CHOICE:    1) DISPLAY DUAL TIME"
1520 PRINT " "
1530 PRINT "                 2) DISPLAY RESPONSE TIME ONLY"
1540 PRINT " "
```

```
1550 PRINT "                 3) DISPLAY EXCITATION TIME ONLY"
1560 PRINT " "
1570 PRINT "                 4) DISPLAY DUAL SPECTRUM "
1580 PRINT " "
1590 PRINT "                 5) DISPLAY RESPONSE SPECTRUM ONLY"
1600 PRINT " "
1610 PRINT "                 6) DISPLAY EXCITATION SPECTRUM ONLY"
1620 PRINT " "
1630 PRINT "                 7) STORE TIME FILE"
1640 PRINT " "
1650 PRINT "                 8) STORE SPECTRUM FILE"
1660 PRINT " "
1710 INPUT "                 9) END";R
1720 GOSUB 9100                 'REMOTE
1722 '
1723 '**********************************************************
1724 '
1725 '     BASED ON MENU CHOICE, PROGRAM BRANCHES TO SUBROUTINES
1726 '
1730 ON R GOSUB 2000,2500,3000,3500,4000,4500,5000,5500,7000
1740 GOTO 1500
1990 '
1991 '**********************************************************
1992 '
1993 '             DUAL TIME DISPLAY COMMANDS
1994 '
2000 O$ = "DF UM"              'UPPER DISPLAY
2010 GOSUB 9300
2020 O$ = "ED FU,1"            'TIME CHANNEL B
2030 GOSUB 9300
2040 O$ = "ED FC,0"            'REAL FUNCTION COORD
2050 GOSUB 9300
2052 O$ = "ED,CT,0"            'MAIN CURSOR
2054 GOSUB 9300
2080 O$ = "ED CU,0"            'CURSOR POSITION = 0
2090 GOSUB 9300
2160 O$ = "EM TM,1"            'TRIGGER ON CHANNEL A
2170 GOSUB 9300
2180 O$ = "EM FS,1600"         'FREQUENCY SPAN = 1.6KHZ
2190 GOSUB 9300
2200 O$ = "DF LM"              'LOWER DISPLAY
2210 GOSUB 9300
2220 O$ = "ED FU,0"            'TIME CHANNEL A
2230 GOSUB 9300
2240 O$ = "ED,CT,0"            'MAIN CURSOR
2250 GOSUB 9300
2300 O$ = "ED CU,0"            'CURSOR POSITION = 0
2310 GOSUB 9300
2312 O$ = "DF UL"              'DISPLAY UPPER/LOWER GRAPHS
2314 GOSUB 9300
2480 GOSUB 9200                'LOCAL
2490 RETURN
```

```
2491 '
2492 '*******************************************************
2493 '
2494 '          RESPONSE TIME DISPLAY COMMANDS
2495 '
2500 O$ = "DF UM"                'UPPER DISPLAY
2510 GOSUB 9300
2520 O$ = "ED FU,1"              'TIME CHANNEL B
2530 GOSUB 9300
2532 O$ = "ED,CT,0"              'MAIN CURSOR
2534 GOSUB 9300
2540 O$ = "ED CU,0"              'CURSOR POSITION = 0
2550 GOSUB 9300
2560 O$ = "EM TM,1"              'TRIGGER ON CHANNEL A
2570 GOSUB 9300
2580 O$ = "EM FS,1600"           'FREQUENCY SPAN = 1.6KHZ
2590 GOSUB 9300
2592 O$ = "DF UF"                'UPPER FULL DISPLAY
2594 GOSUB 9300
2600 GOSUB 9200                  'LOCAL
2610 RETURN
2901 '
2902 '*******************************************************
2903 '
2904 '         EXCITATION TIME DISPLAY COMMANDS
2905 '
3000 O$ = "DF UM"                'UPPER DISPLAY
3010 GOSUB 9300
3020 O$ = "ED FU,0"              'TIME CHANNEL A
3030 GOSUB 9300
3032 O$ = "ED,CT,0"              'MAIN CURSOR
3034 GOSUB 9300
3040 O$ = "EM TM,1"              'TRIGGER ON CHANNEL A
3050 GOSUB 9300
3060 O$ = "EM FS,1600"           'FREQUENCY SPAN = 1.6KHZ
3070 GOSUB 9300
3072 O$ = "DF UF"                'UPPER FULL DISPLAY
3074 GOSUB 9300
3080 GOSUB 9200                  'LOCAL
3090 RETURN
3490 '
3491 '*******************************************************
3492 '
3493 '     DUAL SPECTRUM DISPLAY COMMANDS
3494 '
3500 O$ = "DF UM"                'UPPER DISPLAY
3510 GOSUB 9300
3520 O$ = "ED FU,11"             'SPECTRUM CHANNEL B
3521 GOSUB 9300
3522 O$ = "ED,CT,1"              'HARMONIC CURSOR
3530 GOSUB 9300
3540 O$ = "EM,TM,0"              'TRIGGER SET TO FREE RUN
```

```
3550 GOSUB 9300
3560 O$ = "EM FS,100"          'FREQUENCY SPAN = 100 HZ
3570 GOSUB 9300
3572 O$ = "ED CU,25"           'CURSOR SET TO 25 HZ
3574 GOSUB 9300
3580 O$ = "DF LM"              'LOWER DISPLAY
3590 GOSUB 9300
3600 O$ = "ED FU,10"           'SPECTRUM CHANNEL A
3602 GOSUB 9300
3604 O$ = "ED CT,1"            'HARMONIC CURSOR
3606 GOSUB 9300
3612 O$ = "ED CU,25"           'CURSOR SET TO 25 HZ
3614 GOSUB 9300
3620 O$ = "EM FS,100"          'FREQUENCY SPAN = 100 HZ
3630 GOSUB 9300
3640 O$ = "DF UL"              'UPPER/LOWER GRAPHS
3650 GOSUB 9300
3660 GOSUB 9200                'LOCAL
3670 RETURN
3990 '
3991 '***********************************************************
3992 '
3993 '         RESPONSE SPECTRUM DISPLAY COMMANDS
3994 '
4000 O$ = "DF UM"              'UPPER DISPLAY
4010 GOSUB 9300
4020 O$ = "ED FU,11"           'SPECTRUM CHANNEL B
4030 GOSUB 9300
4032 O$ = "ED CU,25"           'CURSOR SET TO 25 HZ
4034 GOSUB 9300
4040 O$ = "EM FS,100"          'FREQUENCY SPAN = 100 HZ
4050 GOSUB 9300
4052 O$ = "EM,TM,0"            'TRIGGER SET TO FREE RUN
4054 GOSUB 9300
4060 O$ = "DF UF"              'UPPER FULL GRAPH
4070 GOSUB 9300
4080 GOSUB 9200                'LOCAL
4090 RETURN
4490 '
4491 '***********************************************************
4492 '
4493 '      EXCITATION SPECTRUM DISPLAY COMMANDS
4494 '
4500 O$ = "DF UM"              'UPPER DISPLAY
4510 GOSUB 9300
4512 O$ = "ED CU,25"           'CURSOR SET TO 25 HZ
4514 GOSUB 9300
4520 O$ = "ED FU,10"           'SPECTRUM CHANNEL A
4530 GOSUB 9300
4532 O$ = "EM,TM,0"            'TRIGGER SET TO FREE RUN
4534 GOSUB 9300
4540 O$ = "EM FS,100"          'FREQUENCY SPAN = 100 HZ
```

```
4550 GOSUB 9300
4560 O$ = "DF UF"                  'UPPER FULL GRAPH
4570 GOSUB 9300
4580 GOSUB 9200                    'LOCAL
4590 RETURN
4990 '
4991 '***********************************************************
4992 '
4993 '      TIME DISPLAY STORAGE COMMANDS
4994 '
5000 INPUT "ENTER DATA FILE NAME";DF$
5010 OPEN "O",#1,DF$
5020 FOR I = 1 TO 500             ' 500 POINTS OF DATA
5030 O$ = "AF "+STR$(I)
5040 GOSUB 9300
5050 GOSUB 9400
5060  DAT  =  VAL(MID$(E$,2,4))*10^VAL(MID$(E$,8,3))      'DATA
CONVERSION
5080 WRITE #1,I,DAT
5090 NEXT I
5400 CLOSE #1
5410 GOSUB 9200
5440 RETURN
5490 '
5491 '***********************************************************
5492 '
5493 '    SPECTRUM DISPLAY STORAGE COMMANDS
5494 '
5500 INPUT "ENTER DATA FILE NAME";DF$
5510 OPEN "O",#1,DF$
5530 FOR I = 1 TO 800                 ' 800 POINTS OF DATA
5540 O$ = "AF "+STR$(I)
5550 GOSUB 9300
5560 GOSUB 9400
5570 DAT = VAL(MID$(E$,2,6))    'DATA CONVERSION
5580 WRITE #1,DAT
5590 NEXT I
5600 CLOSE #1
5605 GOSUB 9200
5610 RETURN
6990 '
6991 '***********************************************************
6992 '
6993 '       END OF PROGRAM
6994 '
7000 GOSUB 9200
7010 END
8988 '
8989 '***********************************************************
8990 '
8992 ' INITIALIZING THE IEEE INTERFACE
8994 '
```

```
9000 DEF SEG = &HD000
9010 CINIT$ = "SYSCON MAD=3, CIC=1, NOB=1, BA0=&H300"
9020 CREMOTE$ = "REMOTE 26"
9030 CLOCAL$ = "LOCAL 26"
9040 COUTPUT$ = "OUTPUT 26[$]"
9050 CENTER$ = "ENTER 26[$]"
9060 IE488 = 0: A% = 0: FLG% = 0: BRD% = 0
9070 CALL IE488 (CINIT$, A%, FLG%, BRD%)
9080 IF FLG%<>0 THEN PRINT "INSTALLATION ERROR: ";HEX$(FLG%):END
9090 RETURN
9095 '
9                    0                    9                    6
'**************************************************************
9097 '
9098 ' SET THE B&K TO REMOTE
9099 '
9100 CALL IE488 (CREMOTE$, A%, FLG%, BRD%)
9110 IF FLG%<>0 THEN PRINT "REMOTE ERROR: ":HEX$(FLG%):END
9120 RETURN
9195 '
9196 '**************************************************************
9197 '
9198 ' SET THE B&K TO LOCAL
9199 '
9200 CALL IE488 (CLOCAL$, A%, FLG%, BRD%)
9210 IF FLG%<>0 THEN PRINT "LOCAL ERROR: ";HEX$(FLG%):END
9220 RETURN
9295 '
9296 '**************************************************************
9297 '
9298 ' OUTPUT A COMMAND TO THE B&K
9299 '
9300 OUTPUT$ = O$+CHR$(10)
9310 CALL IE488 (COUTPUT$, OUTPUT$, FLG%, BRD%)
9320 IF FLG%<>0 THEN PRINT "OUTPUT ERROR: ";HEX$(FLG%):END
9330 RETURN
9395 '
9396 '**************************************************************
9397 '
9398 ' INPUT DATA FROM THE B&K
9399 '
9400 E$ = SPACE$(15)
9410 CALL IE488 (CENTER$, E$, FLG%, BRD%)
9420 IF FLG%<>0 THEN PRINT "ENTRY ERROR: ";HEX$(FLG%):END
9430 RETURN
*****************************************************************
```

```
10    '**********************************************************
20    '
30    '
40    ' FILENAME: BK
50    '
60    ' THIS PROGRAM WAS USED TO TAKE DATA FROM THE BREUL & KJAER
70      ' TYPE  2032  SIGNAL  ANALYZER  VIA  A  METROBYTE  IEEE  488
INTERFACE
80    ' CARD AND A ZENITH 248 COMPUTER.  THE PROGRAM INTITIALIZES
90    ' THE INTERFACE CARD, BUT DOES INITIALIZE THE B&K 2032.  THE
100   ' PROGRAM ASSUMES THAT THE DATA TO BE STORED IS ALREADY
110   ' ON THE SCREEN OF THE B&K 2032.
120   '
130   ' THE PROGRAM WILL STORED THE SPECTRUM FROM 23 TO 27 HZ IF
THE
140   ' B&K 2032 IS DISPLAYING THE 0 TO 50 HZ SPECTRUM.
150   '
160   ' THE PROGRAM USES THE SAME SUBROUTINES AS "BKDISP"
170   '
180   '***********************************************************
1000 OPTION BASE 1                'ARRAYS BEGIN WITH ELEMENT 1
1010 GOSUB 9000                   'INITIALIZE THE INTERFACE
1020 GOSUB 9200                   'LOCAL
1500 CLS
5500 INPUT "ENTER DATA FILE NAME";DF$
5505 GOSUB 9100                  'REMOTE
5510 OPEN "O",#1,DF$
5530 FOR I = 368 TO 432          'SAMPLES THE CENTER 64 POINTS
5540 O$ = "AF "+STR$(I)
5550 GOSUB 9300
5560 GOSUB 9400
5570 DAT = VAL(MID$(E$,2,6))     'DATA CONVERSION
5580 WRITE #1,DAT
5590 NEXT I
5600 CLOSE #1
5605 GOSUB 9200
5610 GOTO 1020
7000 GOSUB 9200
7010 END
9000 DEF SEG = &HD000
9010 CINIT$ = "SYSCON MAD=3, CIC=1, NOB=1, BA0=&H300"
9020 CREMOTE$ = "REMOTE 26"
9030 CLCCAL$ = "LOCAL 26"
9040 COUTPUT$ = "OUTPUT 26[$"
9050 CENTER$ = "ENTER 26[$
9060 IE488 = 0: A% = 0: FLG% = 0: BRD% = 0
9070 CALL IE488 (CINIT$, A%, FLG%, BRD%)
9080 IF FLG%<>0 THEN PRINT "INSTALLATION ERROR: ";HEX$(FLG%):END
9090 RETURN
9100 CALL IE488 (CREMOTE$, A%, FLG%, BRD%)
9110 IF FLG%<>0 THEN PRINT "REMOTE ERROR: ";HEX$(FLG%):END
9120 RETURN
```

```
9200 CALL IE488 (CLOCAL$, A%, FLG%, BRD%)
9210 IF FLG%<>0 THEN PRINT "LOCAL ERROR: ";HEX$(FLG%):END
9220 RETURN
9300 OUTPUT$ = O$+CHR$(10)
9310 CALL IE488 (COUTPUT$, OUTPUT$, FLG%, BRD%)
9320 IF FLG%<>0 THEN PRINT "OUTPUT ERROR: ";HEX$(FLG%):END
9330 RETURN
9400 E$ = SPACE$(15)
9410 CALL IE488 (CENTER$, E$, FLG%, BRD%)
9420 IF FLG%<>0 THEN PRINT "ENTRY ERROR: ";HEX$(FLG%):END
9430 RETURN
```

Bibliography

1. Churchill, R. Laser Fiber Optic Sensor For Human Biomagnetic Measurements, Topic 86-278, Radford, VA: American Research Corporation of Virginia, 1986.

2. Kraus, J. Electromagnetics. New York, NY: McGraw-Hill Book Company, 1984.

3. Yariv, A. and Winsor, H. "Proposal for the Detection of Magnetic Fields Through Magnetostrictive Perturbation of Optical Fibers," Optics Letters, 5: 87-99 (March 1980).

4. Giallorenzi, T. et al. "Optical-fiber Sensors Challenge the Competition," IEEE Spectrum: 44-49, (September 1986).

5. Churchill, R. Laser Fiber Optic Sensor for Human Biomagnetic Measurements: Phase I Report, Topic 86-278, 1986, Radford, VA: American Research Corporation of Virginia.

6. Dandridge, A. et al. "Optical Fiber Magnetic Field Sensors," Electronics Letters, 16: 408-409, (May 1980).

7. Lenz, J. et al. "Fiber Optic Magnetometer Design," SPIE Fiber Optic and Laser Sensors II, 478: 86-90 (1984).

8. White, B. et al. Optical Fiber Magnetic Field Sensor Studies, October 83 - October 85. Report NADC-85154-30. Naval Air Development Center, October 85 (AD-B098365L).

9. F.W. Bell, Inc. Model 620 Gaussmeter Instruction Manual, Columbus, OH.

10. Bucholtz, F. et al. "Fiber Optic Magnetic Sensor Development," SPIE Fiber Optic and Laser Sensors IV, 718: 56-65 (1986).

11. "New Magnetometer Promises Improved Diagnosis of Brain Disorders," OE Reports, 70: 5 (October 1989).

12. Philips. The Magnetoresistive Sensor. Technical Publication 268. Philips Components Division, Eindhoven, The Netherlands, 1988.

13. Seyrafi, K. Electro-Optical Systems Analysis. Los Angeles, CA: Electro-Optics Research Company, 1985.

14. Jackson, D. et al. "Measurement of Small Phase Shifts Using a Single-mode Optical-Fiber Interferometer," Optics Letters, 5: 139-141 (April 1980).

15. Jackson, D. et al. "Elimination of Drift in a Single-mode Optical Fiber Interferometer Using a Piezoelectrically Stretched Coiled Fiber," Applied Optics, 19: 2926-2929 (September 1980).

16. Koo, K. and Sigel, G. "Characteristics of Fiber-Optic Magnetic Field Sensors Employing Metallic Glasses," Optics Letters,7: 334-336 (July 1982).

17. Jaeger, R. and Aslami, M. "Sensing Magnetic Fields," Fiber Optic Product News, 2: 26-27. (November 1987).

18. Churchill, R. Laser Fiber Optic Sensor for Human Biomagnetic Measurements: Phase II Interim Report, 27 July 1988 - 27 Jan 1989. Contract F33615-87-C-0546. Radford, VA: American Research Corporation of Virginia, February 1989.

19. Reitz, J. and Milford, F. Foundations of Electromagnetic Theory. Reading, MA: Addison-Wesley Publishing Company, 1966.

20. Bozorth, R. Ferromagnetism. New York, NY: D. Van Nostrand Company, Inc., 1951.

21. Abrahams, E. and Keffer, F. "Ferromagnetism," McGraw-Hill Encyclopedia of Science and Technoloogy, 10: 63-68 (1987).

22. Masterton, W. et al. Chemical Principles. Philadelphia, PA: Saunders College Publishing, 1981.

23. Cullity, B. "Fundamentals of Magnetostriction," Journal of Metals, 23: 35-41 (January 1971).

24. Emsley, C., Application Engineer. Telephone interview. York Technology, Hampshire, United Kingdom, 27 June 1989.

25. Giancoli, D. Physics. Englewood-Cliffs, NJ: Prentice-Hall, Inc., 1980.

26. Yariv, A. Optical Electronics. New York, NY: CBS College Publishing, 1985.

27. Okoshi, T. Optical Fibers. New York, NY: Academic Press, 1982.

28. Abramowitz, M. and Stegun, I., Editors. Handbook of Mathematical Functions. Washington, DC: US Government Printing Office, 1964.

29. Hecht, E. and Zajac, A. Optics. Reading, MA: Addison-Wesley Publishing Company, 1979.

30. Hughes, R. and Priest, R. "Thermally Induced Optical Phase Effects in Fiber Optic Sensors," Applied Optics, 19: 1477-1483 (May 1980).

31. Heaton, H. "Thermal Straining in a Magnetostrictive Optical Fiber Interferometer," Applied Optics,19: 3719-3720 (November 1980).

32. Jarzynski, J. et al. "Magnetic Field Sensitivity of an Optical Fiber with Magnetostrictive Jacket," Applied Optics, 19: 3746-3748 (November 1980).

33. Bendow, B. and Mitra, S., Editors. Fiber Optics, New York, NY: Plenum Press, 1979.

34. York Technology. Data Sheet for Fused Coupler Model SC-633-50-0.5, Hampshire, United Kingdom.

35. Touloukian, Y. Thermal Expansion. New York, NY: IFI/Plenum Press, 1975.

36. Sarrafzaeh, D. Project Engineer. Telephone interview. American Research Corporation of Virginia, Radford, Virginia, 2 August 1989.

37. Sousa, B. Application Engineer. Telephone interview. York Technology, Hampshire, United Kingdom, 2 August 1989.

38. Vernitron. Modern Piezoelectric Ceramics, Bedford, OH.

Vita

Captain R. Dempsey Hackett [redacted] As an Air Force dependent, he attended public schools in many states and foreign countries including Okinawa and Singapore. After graduation from high school in 1981, he attended Virginia Polytechnic Institute and State University, from which he received a Bachelor's degree in Electrical Engineering in 1985. He also received a commission in the USAF through the ROTC program. Following graduation, he worked as an electrical engineer in the Army's Night Vision Laboratory until he was called to active duty and stationed at Wright-Patterson AFB, OH. As a lieutenant, he worked as an electrical engineer and contract monitor in the Electro-Optics Technology Branch of the Avionics Laboratory until entering the Air Force Institute of Technology in May 1988.

[redacted]

UNCLASSIFIED

SECURITY CLASSIFICATION OF THIS PAGE

REPORT DOCUMENTATION PAGE

Form Approved
OMB No. 0704-0188

1a. REPORT SECURITY CLASSIFICATION
UNCLASSIFIED

1b. RESTRICTIVE MARKINGS

2a. SECURITY CLASSIFICATION AUTHORITY

2b. DECLASSIFICATION / DOWNGRADING SCHEDULE

3. DISTRIBUTION / AVAILABILITY OF REPORT
Approved for public release;
distribution unlimited

4. PERFORMING ORGANIZATION REPORT NUMBER(S)
AFIT/GEO/ENG/89D-4

5. MONITORING ORGANIZATION REPORT NUMBER(S)

6a. NAME OF PERFORMING ORGANIZATION
School of Engineering

6b. OFFICE SYMBOL (If applicable)
AFIT/ENG

7a. NAME OF MONITORING ORGANIZATION

6c. ADDRESS (City, State, and ZIP Code)
Air Force Institute of Technology
Wright-Patterson AFB OH 45433-6583

7b. ADDRESS (City, State, and ZIP Code)

8a. NAME OF FUNDING / SPONSORING ORGANIZATION
AAMRL

8b. OFFICE SYMBOL (If applicable)
CC

9. PROCUREMENT INSTRUMENT IDENTIFICATION NUMBER

8c. ADDRESS (City, State, and ZIP Code)
Wright-Patterson AFB OH 45433-6583

10. SOURCE OF FUNDING NUMBERS

PROGRAM ELEMENT NO.	PROJECT NO.	TASK NO.	WORK UNIT ACCESSION NO.

11. TITLE (Include Security Classification)
See box 19

12. PERSONAL AUTHOR(S)
R. Dempsey Hackett, BSEE, Captain, USAF

13a. TYPE OF REPORT
MS Thesis

13b. TIME COVERED
FROM ________ TO ________

14. DATE OF REPORT (Year, Month, Day)
1989 December

15. PAGE COUNT
186

16. SUPPLEMENTARY NOTATION

17. COSATI CODES

FIELD	GROUP	SUB-GROUP
20	06	01
20	03	

18. SUBJECT TERMS (Continue on reverse if necessary and identify by block number)
Magnetostriction, Fiber Optics, Interferometers

19. ABSTRACT (Continue on reverse if necessary and identify by block number)

Title: Investigation of a Magnetostrictive Fiber Optic Interferometric Sensor (Unclassified)

Thesis Chairman: Edward S. Kolesar, Major, USAF
Associate Professor
Department of Electrical and Computer Engineering

20. DISTRIBUTION / AVAILABILITY OF ABSTRACT
☐ UNCLASSIFIED/UNLIMITED ☒ SAME AS RPT ☐ DTIC USERS

21. ABSTRACT SECURITY CLASSIFICATION
UNCLASSIFIED

22a. NAME OF RESPONSIBLE INDIVIDUAL
Edward S. Kolesar, Major, USAF

22b. TELEPHONE (Include Area Code)
(513) 255-3576

22c. OFFICE SYMBOL
AFIT/ENG

DD Form 1473, JUN 86

Previous editions are obsolete

SECURITY CLASSIFICATION OF THIS PAGE

UNCLASSIFIED

UNCLASSIFIED

Block 19:

This document reports the results associated with a magnetostrictive fiber optic interferometric sensor which was fabricated and evaluated. To evaluate the sensor's performance, a Helmholtz coil was designed and constructed to generate a uniform magnetic field. The sensor's response was determined by examining the amplitude of the interferometer's output light. No DC magnetic fields could be detected due to excessive noise contributed by the fused coupler component in the interferometer. AC measurements were successfully accomplished for a 25 Hz magnetic field by inspecting the modulation of the interferometer's output light at 25 Hz. Sensors composed of RF sputtered metal coated fibers did not detect the AC magnetic field because the thin metal films did not generate enough force to change the length of the optical fiber a detectable amount. The sensor did detect the AC magnetic field when the sensor arm was composed of a bulk nickel rod. Thermal annealing the nickel rod in the presence of an external magnetic field improved the sensor's response. Thinning the optical fiber in the sensor arm did not significantly affect the sensor's performance, but increasing the length of the optical fiber did enhance the sensor's response. The sensor's performance also improved when the AC magnetic field was superimposed on a DC bias magnetic field. In the sensor's optimum configuration, an AC magnetic field flux density of 10 mG was detected.

UNCLASSIFIED